UNIVERSITY OF CALIFORNIA
SANTA BARBARA

Nonlinear Exciton Dynamics in InGaAs Quantum Wells

A dissertation submitted in partial satisfaction
of the requirements for the degree of

Doctor of Philosophy

in

Physics

by

Benjamin Rene Zaks

Committee in Charge:

Professor Mark Sherwin, Chair

Professor S. James Allen
Professor Leon Balents

August 2012

The dissertation of
Benjamin Rene Zaks is approved:

Professor S. James Allen

Professor Leon Balents

Professor Mark Sherwin, Chair

August 2012

Nonlinear Exciton Dynamics in InGaAs Quantum Wells

by

Benjamin Rene Zaks

Acknowledgements

First and foremost I would like to thank Professor Mark Sherwin for giving me the opportunity to participate in such a fun and exciting research environment. I would also like to thank him for his patience in dealing with me and for being supportive and understanding throughout all of my endeavors, successful and not. Without his leadership, I would certainly not be the scientist that I am today.

I would next like to thank Dave Enyeart for always being ready to run the FEL for me. Without his patience and guidance, none of the work I have done would have been possible, as no one else knows the ins and outs of making the FEL do what you want it to like Dave does. Jerry Ramian was always helpful when we had software problems with the FEL and we appreciate the work he has done in keeping the FEL control system updated and easy to use. I would also like to thank all of the postdocs that have directly influenced my research and who were there to show me the way in the lab when I wasn't sure what the next step was: Dominik Stehr, Ethan Pratt, Sascha Preu, Susumu Takahashi, Vinh Nguyen, and Louis-Cluade Brunel. Additionally I would like to thank the graduate students along the way that have leant their ears for discussion and their support in the lab whenever possible: Dan Allen, Sangwoo Kim, Cristo Yee, Chris Morris, Devin Edwards, and Hunter Banks. In particular, I would like to thank Chris Morris for his help and support through our four years in the Sherwin group together. He was always there for a discussion about our research or to chat about anything else I found interesting, particularly during the many lunches we ate together off campus to avoid the repetitiveness of the UCEN and Nanocafe. I would also like to thank all of the people that have participated in collaborations with my research, including but not limited to Ren-Bao Liu, Stephen Hughes, Pierre Petroff, Tuan-Ahn Truong, Gernot Fasching, and Shawn Mack.

To all my friends in Santa Barbara and elsewhere, thank you for making these six years some of the most enjoyable and memorable years of my life despite the many long days and nights I spent in the lab. You allowed me to have the balance I need to be a successful graduate student.

I would like to thank my parents, Walt and Rhea, and my brother, Aaron, for always being there to support me. I appreciate everything that you have done to allow me to become the man that I am today. Lastly, but definitely not least, I would to thank my fiancée Annie for being there through thick and thin for the last six years and more, always ready to lift me back up when I was ready to fall, I truly could not have achieved this without you.

Curriculum Vitae

Benjamin Rene Zaks

Education

2012	Ph.D. in Physics, University of California, Santa Barbara
2009	M.A. in Physics, University of California, Santa Barbara
2005	B.S. in Physics, University of California, Berkeley

Publications

“ High-order sideband generation in bulk GaAs" B. Zaks, H. Banks and M. S. Sherwin, *In preperation, 2012*

“Experimental observation of electron-hole recollisions" B. Zaks, R. B. Liu and M. S. Sherwin, Nature **483**, 580-583 (2012).

“THz-driven quantum wells: Coulomb interactions and Stark shifts in the ultrastrong coupling regime" B.Zaks, D. Stehr, T. Truong, P. M. Petroff, S. Hughes and M. S. Sherwin, New Journal of Physics **13**, 083009 (2011).

“Efficient Current Injection into 3-D Confined Nanostructures for Room-Temperature THz Lasers" C. Morris, G. Fasching, E. Pratt, H. Kim, B. Zaks, T. Truong, V. Nguyen, P. M. Petroff and M. S. Sherwin, *DARPA seedling project final report, July 2010.*

Conference Proceedings

“ High-Order Sideband Generation in Quantum Wells Driven by Intense THz Radiation: Electron-Hole Recollisions" B. Zaks, R. B. Liu and M. S. Sherwin, *Conference on Lasers and Electro-Optics (2012)*

“ Asymmetric Autler-Townes Effect in THz-driven Quantum Wells: Beyond the Three State and Rotating Wave Approximations" B. Zaks, D. Stehr, S. Hughes, A. Maslov, D. S. Citrin and M. S. Sherwin, *Conference on Lasers and Electro-Optics (2010)*

“Single-Shot, High-Resolution THz Upconversion Spectrometer" B. Zaks, J. Heyman, D. Stehr, D. Allen, N. Coates and M. S. Sherwin, *33rd International Conference on Infrared and Millimeter Waves (2008).*

Awards

Winner of the 2012 International Conference on the Physics of Semiconductors Young Scientist Best Paper Award for the publication *Experimental Observation of Electron-Hole Recollisions.*

Abstract

Nonlinear Exciton Dynamics in InGaAs Quantum Wells

Benjamin Rene Zaks

Near infrared and optical light applied near the band edge of a semiconductor can lead to the formation of bound electron-hole pairs known as excitons. Using growth methods such as molecular beam epitaxy, semiconductor heterostructures can be engineered to have properties beneficial to particular experiments. The formation of very thin layers of semiconductor can lead electrons and holes to be confined along a particular direction, and one structure that can be grown is called a quantum well. The confinement of charges in a quantum well will lead to a stronger Coulomb interaction between the electrons and holes and increase the formation of excitons in the heterostructure. When excitons are driven with an intense THz field, changes to the optical properties of the semiconductor can be observed. These changes to the optical properties can not only provide interesting information about the exciton system, but also may provide insight on modulating optical beams at THz frequencies, information that may be necessary to further improve the speed and quality of our cable and internet connections. By growing InGaAs quantum wells with AlGaAs barriers on a GaAs substrate, we have observed strong changes to the optical spectrum due to intense THz fields. We find that when the strong THz field is applied to an intersubband transition in the quantum well, the applied field can significantly shift the energy of that intersubband transition. This shift is unexpected within the approximations often used to describe this system, and we find that full numerical simulations of the system are necessary to interpret our results. When the strong THz field is polarized in the plane of the quantum well, we are able to observe optical light at up to 11 frequencies that were not present before application of the THz. The new frequencies are separated from the optical frequency by multiples of the THz frequency and are often referred to as sidebands. To understand the origin of the high-order sidebands observed, which are present up to 18^{th} order, a recollision model between electrons and holes is adopted. Strong agreement with theoretical predictions indicates that recollisions are responsible for high-order sideband generation providing an intriguing connection between atomic and condensed matter phenomena.

Contents

Chapter 1

Background Information

The experiments described in this manuscript are mainly performed on excitons in quantum wells. An exciton is an excitation in a semiconductor which has atom like properties. A quantum well is a potential trap for electrons and "holes" in semiconductors. In order to be able to understand the effects described, we need to develop an understanding of the tools used to investigate the interesting phenomena observed. Here we provide a brief description of quantum wells in semiconductors followed by a short section describing excitons. Additionally, there is a brief description of the UC Santa Barbara Free Electron Laser (FEL), the main tool used to make this research possible. After an overview of quantum wells, excitons and the free electron laser, we will be ready to start investigating and understanding the more interesting and unique effects we have observed like optical sideband generation and the Autler-Townes splitting of a near infrared absorption peak. Much of the work in this chapter can be found in much more detail in the books *Introduction to Solid State Physics* by Charles Kittel[1] and *The Physics of Low − Dimensional Semiconductors* by John H. Davies[2].

1.1 Quantum Wells

1.1.1 Semiconductor Quantum Wells

When an electron travels through a vacuum, it's wave function can often be described by a plane wave with a parabolic energy-momentum dispersion curve. In contrast, when an electron is in a crystalline material defined by a periodic potential, its wavefunction is modified by the potential and often gaps are formed in its energy-momentum dispersion relation. The regions separated by these energy gaps are often referred to as energy bands. The electronic wavefunction can be described by the Bloch function, and this formalism allows us to better understand the nature of bands in solids:

$$\psi_k\left(\mathbf{r}\right) = e^{i\mathbf{k}\cdot\mathbf{r}} u_k\left(\mathbf{r}\right) \tag{1.1}$$

Though any material may have a number of band gaps, in general the most interesting energy gap is the gap between the highest filled band (valence band) and the lowest unfilled band (conduction band), $E_{gap} = E_C - E_V$. Band gaps in semiconductors are dependent on the material and are on the order of $\sim 1\,eV$. If a semiconductor is "undoped", then it has an empty conduction band and a full valence band, and it will be a poor conductor at low bias. A doped semiconductor will have carriers in either the valence or conduction band and will be a decent conductor at low bias. In an undoped semiconductor, electrons can often be excited from a valence band to a conduction band by an optical photon, temporarily making the semiconductor a decent conductor. By accurately growing monolayers of semiconductors and semiconductor alloys on top of each other, the properties of the energy bands can be specifically engineered in materials. In particular, when a material with a lower band gap is grown between two layers of a material with a higher band gap, an electron in this heterostructure will see a lower potential in the center material, creating what is referred to as a quantum well (Figure 1.1). This quantum well is a potential trap for any electrons present, and due to the length scales and energies relevant to this problem, it must be treated quantum mechanically.

The easiest quantum well to study is the infinite square well, often the first quantum mechanics problem given to undergraduate physicists. The band gap of the surrounding material is assumed to be infinite, which is physically impossible, but provides a very good approximation nonetheless. If we are interested in understanding how an electron trapped in the conduction band will behave in a well with width L, we can write down the energy levels and wavefunctions for this system. Assuming the width of the well is in the z-direction, the well extends from $z = 0$ to $z = L$, and that the effective mass of the electron is m_e^*, the wave

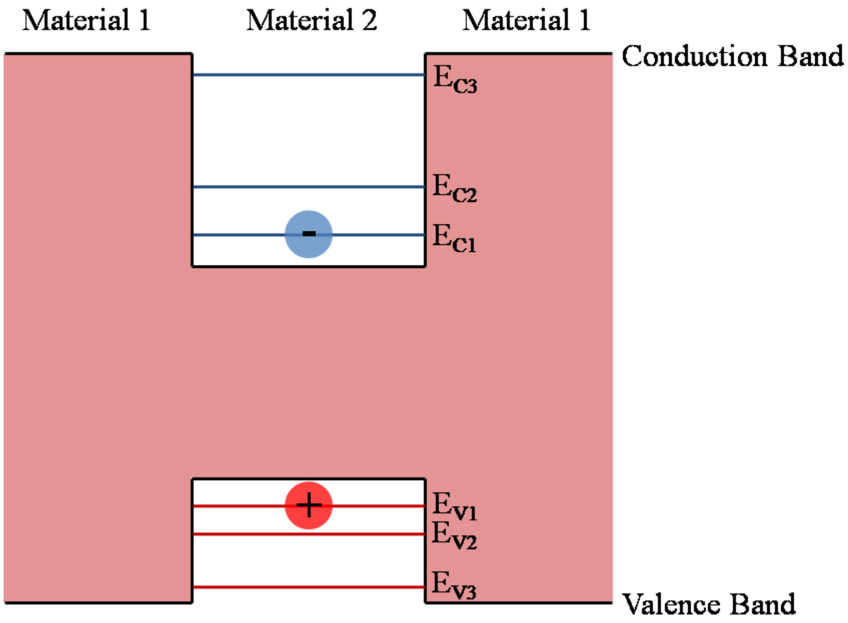

Figure 1.1: A diagram showing the potential energy as a function of position in the material. There is a quantum well formed in both the conduction and valence bands. An electron present in the material will see a lower potential energy in material 2 and can become trapped there. One example of this system is a layer of GaAs (material 2) between two layers of AlGaAs (material 1). A simple picture of a quantum well potential energy with valence and conduction bands, formed by placing a low band gap material between two layers of higher band gap material. An example would be a layer of GaAs between two layers of AlGaAs.

functions and energies take the form:

$$E_n = \frac{n^2\hbar^2\pi^2}{2m_e^* L^2} \tag{1.2}$$

$$\psi_n = \sqrt{\frac{2}{L}}\sin\left(\frac{n\pi z}{L}\right) \tag{1.3}$$

Because the confinement in a quantum well is only along the z-direction, the electrons are free to move in the x-y plane. This freedom creates a continuum of energies above the quantized energy levels. Because each quantum well energy level has a continuum of energy states in the x-y plane, they are reffered to as subbands. The wavefunction in 3-d is the product of the wavefunctions in the z-direction and the x-y plane. In the z-direction, the wavefunction $\phi_n(z)$ is still given by a linear combination of the quantum well eigenstates. In the x-y plane, the wavefunction can be represented by a plane wave $e^{i\mathbf{k}\cdot\mathbf{r}}$. The energy of an electron in the n^{th} conduction subband with a momentum $\mathbf{k} = (k_x, k_y)$ is given by

$$E_{Cn,\mathbf{k}} = E_{Cn} + \hbar(k_x^2 + k_y^2)/2m_e^* \tag{1.4}$$

and the wavefunction is

$$f_{Cn} = C\phi_{Cn}(z)\, e^{i\mathbf{k}\cdot\mathbf{r}} \tag{1.5}$$

where C is a constant of normalization and the energies $E_{Cn,\mathbf{k}}$ are obtained by inserting the wavefunctions into the Schrödinger equation. We note that the wavefunction of the states near the bottom of the conduction band have the symmetry of s orbitals. This will be important to consider when we discuss optical absorption.

Though we have discussed electron quantum wells in the conduction band, we can see from Fig. 1.1 that there is also a potential well in the valence band. This quantum well is a potential energy trap for "holes". A "hole" is the absence of an electron in an otherwise full valence band. In the single particle model, holes behave like positively charged particles with magnitude e, however have an effective mass that is dependent on the material given as m_h^*. Solving for the energies and wavefunctions in the valence band, we find that the wavefunctions are still given by eq. 1.3 and the energies are given by eq. 1.2 with m_e^* replaced by m_h^*. Confinement of holes and electrons leads to quantization of energy levels in both the conduction and valence band, however, differing effective masses between the electrons and holes leads to different energy spacing in these bands, as is demonstrated in Figure 1.2. In the InGaAs quantum wells investigated, strain broke the heavy hole light hole degeneracy and moved the light hole band significantly further away from the conduction band. Due to this shift, many complexities due to degeneracy in the valance band can be ignored and will not be discussed further.

In the valence band, the zero energy point is at the top of the band. The energy of the hole is opposite the energy of the electron and the work done to remove an electron from a low orbital is greater than to remove it from a higher one. Because the valence band states at the top of the band correspond to higher orbitals, they have a p type symmetry. The valence subband energies and wavefunctions for

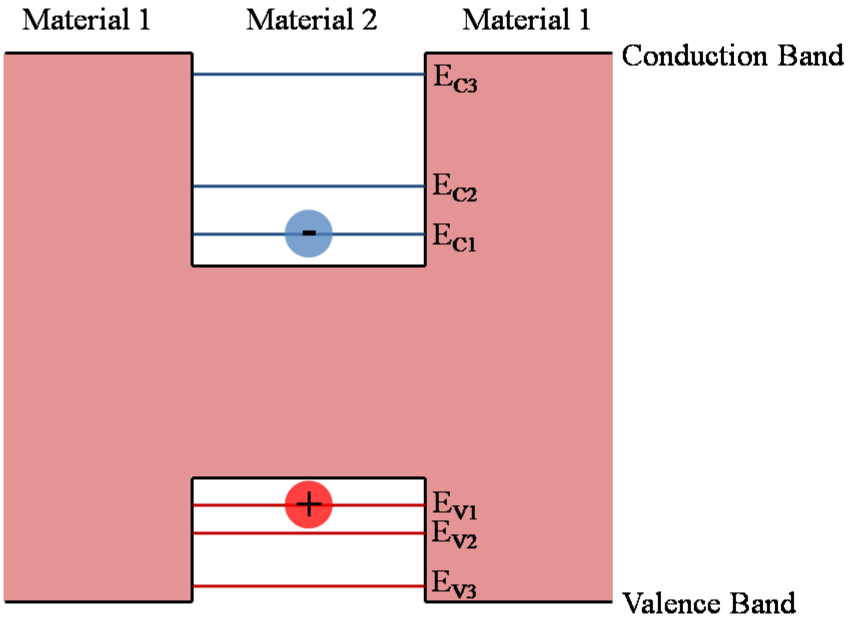

Figure 1.2: Diagram of a quantum well showing the distinct energy levels in the conduction and valence bands. For most GaAs alloys, the effective mass of the holes is larger than the effective mass for electrons, leading to a smaller spacing between energy levels in the valence band than in the conduction band.

holes are given by:

$$E_{Vn,\mathbf{k}} = E_{Vn} - \hbar(k_x^2 + k_y^2)/2m_h^* \tag{1.6}$$

$$f_{Vn} = C\phi_{Vn}\left(z\right) e^{i\mathbf{k}\cdot\mathbf{r}} \tag{1.7}$$

achieved in similar manner to the conduction subbands. Here we can see that in the infinite potential well model, the wavefunctions in the valence band are essentially identical to the corresponding wavefunctions in the conduction band. Additionally, we note that holes moving in the valence band interact with electric fields like a particle with positive charge e.

In an undoped semiconductor at equilibrium at T = 0K, there are no electrons in the conduction band and no holes in the valence band. When an electron in an undoped semiconductor is excited into the conduction band it will leave a hole in the valence band. This is often achieved by absorption of a photon with energy greater than the band gap.

1.1.2 Optical Absorption

In the single electron model, electrons and holes will interact individually with electromagnetic fields present in the materials. In general, the wavelengths which are relevant to this system span many unit cells and have a low photon momentum. In this case, the photon momentum is neglected and the electric field is considered constant across a unit cell. This is called the $electric - dipole\, approximation$. In this approximation, we can write down the transition rate from an initial state i

to a final state j using Fermi's golden rule:

$$W_{ij} = \frac{2\pi}{\hbar}\frac{e^2 E_0^2}{4{m^*}^2\omega^2}\left|\langle i|\mathbf{e}\cdot\mathbf{p}|j\rangle\right|^2 \delta\left(E_f - E_i - \hbar\omega\right) \tag{1.8}$$

where $\mathbf{e}$ is the polarization vector of the electric field, E_j and E_i are the final and initial state energies, and $\mathbf{p}$ is the quantum mechanical momentum operator. When the photon is resonant with transition, $\hbar\omega = E_j - E_i$, we see that $\left|\langle i|\mathbf{e}\cdot\mathbf{p}|j\rangle\right|^2$ is the term responsible for the strength of the absorption. If the initial and final wavefunctions are known, then the matrix element can be evaluated to achieve the transition rate.

1.1.2.1 Quantum Well Interband Absorption

In an undoped semiconductor, there are no available states in the gap and only light with energy greater than E_{gap} will be absorbed by the material. When Coulomb effects are included, electrons and holes can become bound to each other allowing energy to be absorbed slightly below E_{gap}. This will be discussed in Section 1.2. In a quantum well, the highest energy state in the valence band is E_{V1} and the lowest energy in the valence band is E_{C1} so that the lowest energy photon that can be absorbed is $E_{C1} - E_{V1}$. Due to confinement in a quantum well, $E_{C1} - E_{V1} > E_{gap}$ and the absorption begins at higher energy than in the bulk. If we consider a interband transition from an initial state in the valence band to a final state in the conduction band, we can write out the transition rate if we obtain the matrix element $\langle i|\mathbf{e}\cdot\mathbf{p}|j\rangle$. Because the wavefunctions in both the valence and conduction bands contain a Bloch wavefunction $|u\rangle$ and an envelope wavefunction $|f\rangle$, this matrix element can be expanded into two terms

$$\langle i|\mathbf{e}\cdot\mathbf{p}|f\rangle = \mathbf{e}\cdot\langle u_{V\nu}|\,\mathbf{p}\,|u_{C\nu'}\rangle\,\langle f_{Vn}|f_{Cn'}\rangle + \mathbf{e}\cdot\langle u_{V\nu}|\,u_{C\nu'}\rangle\,\langle f_{Vn}|\mathbf{p}|f_{Cn'}\rangle \tag{1.9}$$

The first term is responsible for interband transitions (valence to conduction) while the second is responsible for intersubband transitions (within the valence or conduction bands). Here υ denotes the band and n denotes the subband.

For an interband transition, the matrix element $\langle u_{V\nu}|\,u_{C\nu'}\rangle$ vanishes and we will examine the first term in eq. 1.9 within the Luttinger Kohn model. The first part of this term $\mathbf{e}\cdot\langle u_{V\nu}|\,\mathbf{p}\,|u_{C\nu'}\rangle$ is only dependent on the polarization of the light $\mathbf{e}$ and the Bloch wavefunctions. As stated before, the conduction band states are s like and the valence band states are p like, which will help us determine the selection rules for interband absorption. The valence band wavefunctions can be modeled as a spin $3/2$ system. If we assume that the initial state is a heavy hole state, which is proportional to a spin state with a total momentum $\mathbf{j} = 3/2$ and z-momentum $j_z = 3/2$, then $|u_{V\nu'}\rangle \propto \left|\frac{3}{2},\frac{3}{2}\right\rangle \propto |X + iY\rangle$ and the matrix element $\mathbf{e}\cdot\langle u_{V\nu}|\,\mathbf{p}\,|u_{C\nu'}\rangle$ is only non-zero for light polarized in the x-y plane (no dipole moment in the z-direction) and we would expect to see no absorption when the light is polarized in the growth direction. Here, $|X\rangle, |Y\rangle$ and $|Z\rangle$ denote the direction of orientation of the p-like orbitals, with z being the growth direction of the quantum wells. If the initial state is a light hole state, which is proportional to a spin state with a total momentum $\mathbf{j} = 3/2$ and z-momentum $j_z = 1/2$, then

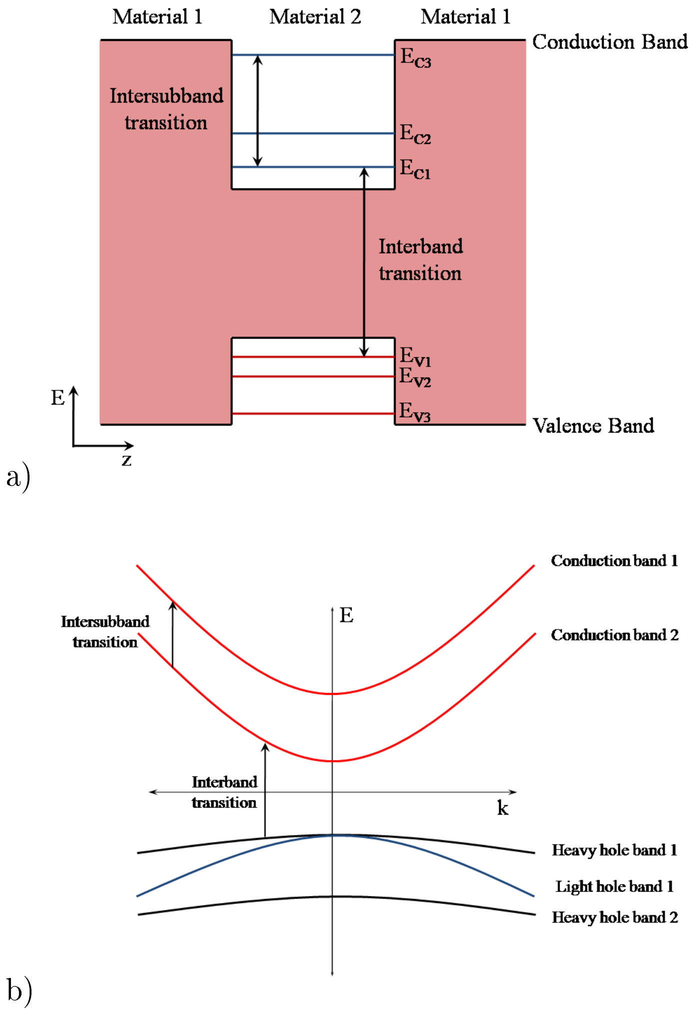

Figure 1.3: Diagram of interband and intersubband transitions in a semiconductor quantum well. Energy as a function of position along the growth direction is shown in a). Energy as a function of the in plane momentum k (along the x- and y-axis) is shown in b).

$|u_{V\nu'}\rangle \propto \left|\frac{3}{2},\frac{1}{2}\right\rangle \propto |X+iY\rangle + |Z\rangle$ and we would expect to see absorption for all polarizations of light. These are the polarization selection rules for interband absorption in a square quantum well.

The second set of selection rules is imposed by the second half of the first term of eq. 1.9. We see that the integral of the envelope wavefunctions with no operator between them,$\langle f_{Vn}|f_{Cn'}\rangle$, must be non-zero. Inserting our conduction and valence band wavefunctions, we obtain (ignoring normalization):

$$\langle f_{Vn} \mid f_{Cn'}\rangle = \int d^3r\, e^{i\mathbf{k}\cdot\mathbf{r}}\phi^*_{Vn}(z)\, e^{-i\mathbf{k}'\cdot\mathbf{r}}\phi_{Cn'}(z) = \delta_{\mathbf{k}\mathbf{k}'}\cdot\int dz\,\phi^*_{Vn}(z)\,\phi_{Cn'}(z) \tag{1.10}$$

We immediately see that the integral will vanish unless $\mathbf{k} = \mathbf{k}'$which imposes only vertical transitions. This leaves us with the integral $\int dz\,\phi^*_{Vn}(z)\,\phi_{Cn'}(z)$. In the infinite square well approximation, the wavefunctions in the conduction and valence bands are exactly the same and this integral can be simplified:

$$\int dz\,\phi^*_{Vn}(z)\,\phi_{Cn'}(z) = \int dz\,\phi^*_{n}(z)\,\phi_{n'}(z) = \delta_{nn'} \tag{1.11}$$

In an infinite square well, this imposes the selection rule $\Delta n = 0$. In finite wells, this selection rule is relaxed, but the strongest transitions still correspond to $\Delta n = 0$. In a symmetric quantum well like the one discussed here, the states will all be either symmetric or antisymmetric and the matrix element will vanish unless the states have the same parity. Therefore interband transitions are only allowed between states where Δn is *even*.

1.1.2.2 Quantum Well Intersubband Absorption

If we examine the matrix element $\langle i|\mathbf{e}\cdot\mathbf{p}|j\rangle$ for an intersubband transition, we obtain the following equation:

$$\langle i|\mathbf{e}\cdot\mathbf{p}|f\rangle = \mathbf{e}\cdot \langle u_\nu|\,\mathbf{p}\,|u_\nu\rangle \langle f_n|f_{n'}\rangle + \mathbf{e}\cdot \langle u_\nu|\, u_\nu\rangle \langle f_n|\mathbf{p}|f_{n'}\rangle \tag{1.12}$$

Because intraband transitions are between different levels of the same band, the matrix element $\langle u_\nu|\,\mathbf{p}\,|u_\nu\rangle$ will vanish leaving only the second term in the equation. It is easy to see that the matrix element $\langle u_\nu|\, u_\nu\rangle$ will become unity leaving only the term $\langle f_n|\mathbf{e}\cdot\mathbf{p}|f_{n'}\rangle$ responsible for intersubband transitions.

Explicitly writing out the integral for this term,we obtain the following:

$$\langle f_n|\mathbf{e}\cdot\mathbf{p}|f_{n'}\rangle = \int d^3r\, e^{i\mathbf{k}\cdot\mathbf{r}}\phi_n^*(z)\,\mathbf{e}\cdot\mathbf{p}\,e^{-i\mathbf{k}'\cdot\mathbf{r}}\phi_{n'}(z) \tag{1.13}$$

We know that the operator $\mathbf{e}\cdot\mathbf{p} = -i\hbar\left(\frac{\partial}{\partial x}e_x + \frac{\partial}{\partial y}e_y + \frac{\partial}{\partial z}e_z\right)$ and that the wavefunctions along the z-axis and in the x-y plane are separable, which simplifies the previous matrix element for particular polarizations of light. When light is polarized in the x-y plane, we obtain the following:

$$\langle f_n|\mathbf{e}\cdot\mathbf{p}|f_{n'}\rangle \propto \delta_{\mathbf{k}\mathbf{k}'}\langle \phi_n(z)\mid \phi_{n'}(z)\rangle \tag{1.14}$$

The wavefunctions $\phi_n(z)$ are orthogonal and the matrix element $\langle \phi_n(z)\mid \phi_{n'}(z)\rangle$ is zero unless $n = n'$. Therefore, no transitions in the quantum well occur with light polarized in the quantum well plane. For light polarized in the growth direction, along the z-axis, eq. 1.13 is proportional to the following:

$$\langle f_n|\mathbf{e}\cdot\mathbf{p}|f_{n'}\rangle \propto \delta_{\mathbf{k}\mathbf{k}'}\langle \phi_n(z)\mid p_z \mid \phi_{n'}(z)\rangle \tag{1.15}$$

First, we see that the matrix element will vanish unless $\mathbf{k} = \mathbf{k}'$, which again imposes vertical transitions within the band. Additionally, we see a strong dependence on the matrix element between the initial and final quantum well states $\left\langle \phi_n\left(z\right) \mid \frac{\partial}{\partial z} \mid \phi_{n'}\left(z\right)\right\rangle$. This matrix element may be easily evaluated in the infinite square well model, but we note that the momentum operator only connects states of opposite parity and we see that transitions are only allowed when Δn is *odd*. This is in stark contrast to the interband absorption, which has distinctly different selection rules.

1.2 Excitons

Until now, we have discussed quantum wells and the interband absorption assuming the single electron model to describe the bands. Though this model is quite successful at describing the physics of semiconductors and heterostructures quite well in general, real experiments deviate from these predictions when absorption near the band edge is investigated. The reason for the discrepancy near the band edge is due to *excitons*, bound electron-hole pairs which dominate the absorption spectrum, particularly at low temperature. We have neglected the Coulomb force in our previous calculations, and have thus neglected any interaction between the electrons and holes we are creating. In the following section, we will introduce the Coulomb potential into our Hamiltonian and see how excitons effect the quantum well system.

1.2.1 Coulomb Potential

In an undoped semiconductor, the ground state of our system is a completely filled valence band and an empty conduction band. When we excite an electron across the band gap, we can describe this situation as superposing an electron in the conduction band and a hole in the valence band on top of the ground state of a full valence band and empty conduction band. In other words, we are creating an electron-hole pair. Because the electron and the hole carry opposite charge, they will be attracted to each other via the Coulomb potential similar to the attraction between an electron and a proton in a hydrogen atom. This Coulomb attraction can lead to bound states, or *excitons*, which have lower energy than free electron-hole pairs and can therefore be observed as absorption slightly below the band edge.

We can write down the Hamiltonian for the electron hole system in a semiconductor heterostructure as the following:

$$[(E_C - \frac{\hbar^2}{2m_e^*}\nabla_e^2) - (E_V + \frac{\hbar^2}{2m_h^*}\nabla_h^2) - \frac{e^2}{4\pi\epsilon_r \left|\mathbf{R}_e - \mathbf{R}_h\right|}$$

$$+V_e(\mathbf{R}_e) + V_C(\mathbf{R}_h)]\psi(\mathbf{R}_e, \mathbf{R}_h) = E\psi(\mathbf{R}_e, \mathbf{R}_h) \tag{1.16}$$

where the wavefunction is dependent on the coordinates of both the electron and the hole, $\mathbf{R}_e$ and $\mathbf{R}_h$. Before investigating the more complicated quantum well system, let us first examine the nature of excitons in a three dimensional material with no confining potentials V_e or V_h.

1.2.1.1 Excitons in Three Dimensions

With no confining potentials, the electron and hole are free to move throughout the crystal freely except for the interaction between them. This interaction is only dependent on the difference of their coordinates, and we can translate the Schrödinger equation into the center of mass coordinate system with the new coordinates $\mathbf{R}_{CM}$ and $\mathbf{R}$ by the following relations:

$$\mathbf{R}_{CM} = \frac{m_e^*\mathbf{R}_e + m_h^*\mathbf{R}_h}{M} \tag{1.17}$$

$$\mathbf{R} = \mathbf{R}_e - \mathbf{R}_h \tag{1.18}$$

$$M = m_e^* + m_h^* \tag{1.19}$$

$$\frac{1}{m_{eh}^*} = \frac{1}{m_e^*} + \frac{1}{m_h^*} \tag{1.20}$$

leading to the Schrödinger equation in the new coordinate system:

$$[-\frac{\hbar^2}{2M}\nabla_{CM}^2 + (E_g - \frac{\hbar^2}{2m_{eh}^*}\nabla^2 - \frac{e^2}{4\pi\epsilon_r R})]\psi = E\psi \tag{1.21}$$

The operators which are dependent on $\mathbf{R}$ and $\mathbf{R}_{CM}$ appear additively and therefore the wavefunction can be factored into a product of functions of $\mathbf{R}$ and $\mathbf{R}_{CM}$. The center of mass operator is simply the free particle Schrödinger equation for a particle with mass M. The solutions to the center of mass part of the Schrödinger equation are plane waves $e^{i\mathbf{K}_{CM}\cdot\mathbf{R}_{CM}}$ with energy $\frac{\hbar^2K^2}{2M}$. However, when excitons are generated optically, the small wavevector of the incident photon limits the the center of mass wavevector to $K_{CM} \approx 0$ and the center of mass motion is ignored.

Focusing on the relative motion between the electron and the hole, we are left with the following equation

$$[-\frac{\hbar^2}{2m_{eh}^*}\nabla^2 - \frac{e^2}{4\pi\epsilon_r R}]\Phi(\mathbf{R}) = (E - E_g)\Phi(\mathbf{R}) \tag{1.22}$$

We clearly see that this equation is the Schrödinger equation for a hydrogen atom with the following substitutions: the electron mass is replaced by the electron hole reduced mass $m_0 \rightarrow m_{eh}^*$, the dielectric constant is scaled by the relative dielectric constant $\epsilon_0 \rightarrow \epsilon_r$, and the energy is shifted down by the band gap $E \rightarrow E - E_g$. Therefore, as in the hydrogen atom, we find that the energy levels of the exciton are quantized and proportional to $1/n^2$ and the energies can be found by scaling the adjusted parameters. This leads to energies given by

$$\varepsilon_n = E_g - \frac{E_{Ryd,e-h}}{n^2}, \;\; E_{Ryd,e-h} = \frac{m_{eh}^*}{2}(\frac{e^2}{4\pi\epsilon_r\hbar})^2 \tag{1.23}$$

where $E_{Ryd,e-h}$ is the Rydberg energy scaled by the dielectric constant and the effective mass of the electron-hole system. In GaAs, the Rydberg energy is on the order of a few meV. From this description, it is easy to see that an exciton is an atom-like system that has discrete energy levels which are slightly below the band gap of the material. Just as we can define the Bohr radius for a hydrogen atom, we can also write down the Bohr radius for an exciton:

$$a_{exciton} = \frac{4\pi\epsilon_r\hbar^2}{e^2 m_{eh}} \tag{1.24}$$

In GaAs, we find that the Bohr radius of the exciton to be $a_{exciton} \approx 10\,nm$. Because of the small wavevector of optical photons, the center of mass motion is taken to be zero and absorption due to excitons can be observed as discrete lines at slightly lower energy than the continuous absorption that occurs above the band gap.

1.2.1.2 Excitons in Two Dimensions

In a purely two dimensional system where the wavefunctions have zero thickness along the growth direction z, the theory of excitons is not greatly changed. By again separating the relative and center of mass coordinates the two dimensional hydrogen atom, the energy levels can be solved for

$$\varepsilon_n^{(2D)} = E_g - \frac{E_{Ryd,e-h}}{(n-\frac{1}{2})^2} \tag{1.25}$$

and we see that the lowest energy state has four times the binding energy of the three dimensional exciton. Additionally, we find that the exciton Bohr radius is decreased by 2. Due to the increased binding energies in the two dimensional system, one expects that excitons should be more significant in low dimensional systems.

1.2.1.3 Excitons in a Quantum Well

To a lowest approximation, excitons in a quantum well can be treated as excitons in a two dimensional system. As we would expect from the increased Coulomb energy compared to the bulk, the quantum well absorption spectrum is dominated by excitons near the band edge. However, because the Bohr radius of

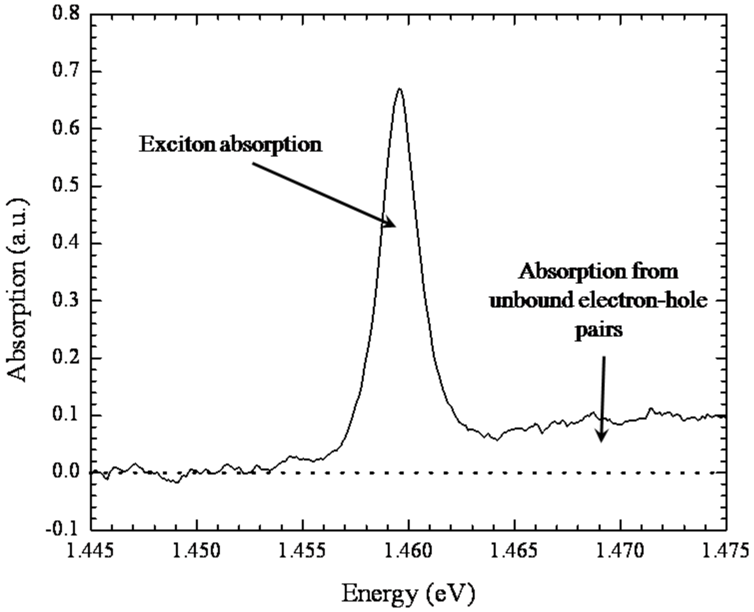

Figure 1.4: Absorption from an InGaAs quantum well. The large feature is due to exciton absorption in the sample. At energies below the exciton line, we see negligible absorption while we can see a small amount of absorption above the exciton line from unbound electron-hole pairs. The absorption near the band edge is dominated by exciton absorption.

the exciton is of the same order as the width of the well, proper analysis means that the Coulomb interaction and the confinement must be treated equally. The two and three dimensional solutions to the exciton problem can be treated as limits of an infinitely thin or wide quantum well, respectively. Though the exact wavefunctions and energies are difficult to calculate exactly from first principles, these limits help us understand the expected behavior of excitons in a quantum well.

One major difference between the simple two dimensional system and a real quantum well is that the confinement in the z-direction leads to the formation of subbands. A transition from a valence subband ν to a conduction subband ν' has an energy $E_{V\nu-C\nu'} = E_{V\nu} - E_{C\nu'}$. Due to the energy gap between the subbands, each transition can support a separate exciton. The energy levels of a particular transition in a quantum well is given by:

$$\varepsilon_n^{(QW)} = E_{V\nu-C\nu'} - \frac{E_{Ryd,e-h}}{(n-\frac{1}{2})^2} \tag{1.26}$$

In the following experiments, transitions between different excitons will be investigated intensively and the distinction between intra-excitonic (n to n') and interexcitonic ($V\nu$ to $C\nu'$) transitions will be important to understand.

1.3 Free Electron Laser

The Free Electron Laser (FEL) is tool unique to UC Santa Barbara which is capable of producing THz radiation from 100 GHz to 5 THz. The FEL uses an electrostatic accelerator to produce a beam of electrons with an energy of up to 6 MeV which is sent through an oscillating magnetic field to wiggle the electrons. As the electrons wiggle they emit radiation and by carefully designing the frequency of oscillation and by building a cavity, it is possible to produce coherent, collimated radiation. Tuning of the THz radiation is achieved by adjusting the energy of the electron beam. Though the population inversion which provides gain in a normal laser is not present in an FEL, the radiation produced behaves as a laser would.

In general, the FEL can provide between 500W and 2kW of power at most frequencies running in its normal operation mode. However, if more intense THz fields are necessary, the FEL cavity dump system can be used. Inserting a thin undoped silicon wafer into the THz cavity at Brewsters angle should not strongly effect the THz generation as the absorption from the silicon is minimal at THz frequencies and the reflection should be zero at Brewsters angle. However, when the silicon wafer is illuminated with light above the band gap, it very quickly becomes metallic and very reflective. In practice, the silicon wafer is illuminated by a Nd:YAG laser to dump all of the power in the laser cavity at once. This produces a pulse that is $\sim$ 40 ns, the round trip travel time for light in the cavity[3].

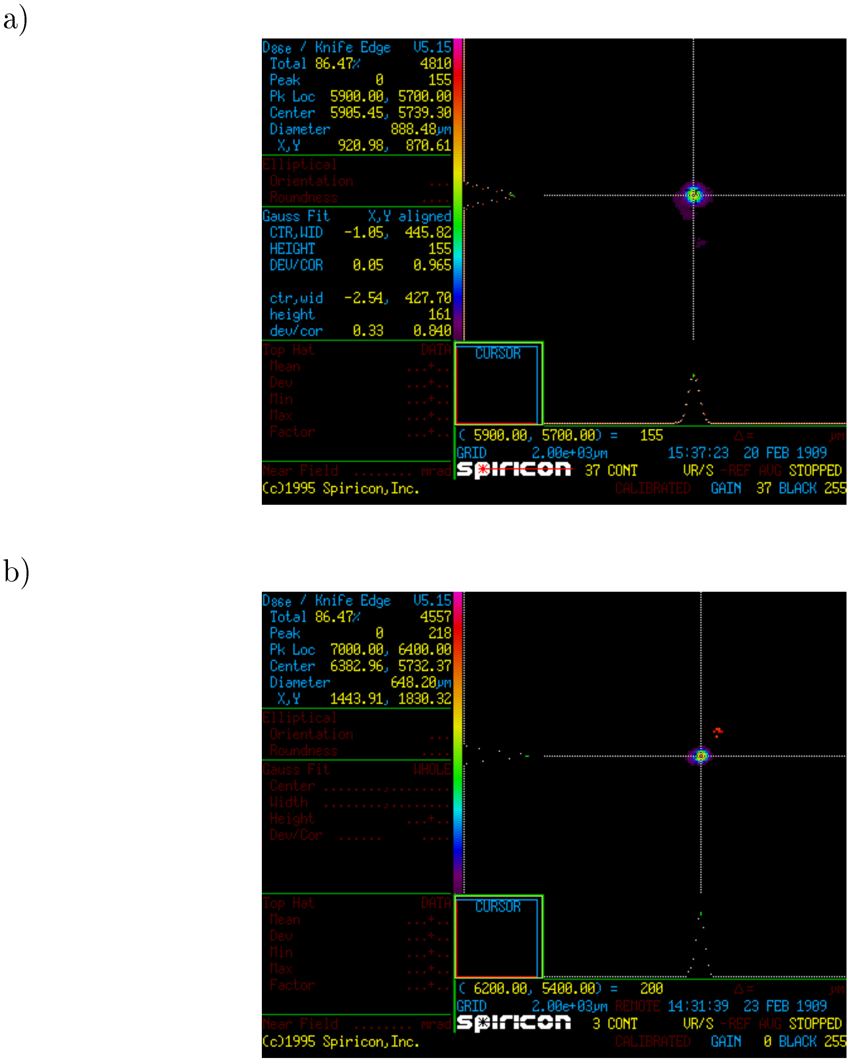

a)

```
D86e / Knife Edge   V5.15
 Total 86.47%        4810
 Peak           0     155
 Pk Loc  5900.00, 5700.00
 Center  5905.45, 5739.30
 Diameter       888.48μm
  X,Y     920.98,  870.61
Elliptical
 Orientation          ...
 Roundness           ....
Gauss Fit     X,Y aligned
 CTR,WID   -1.05,  445.82
 HEIGHT               155
 DEV/COR    0.05    0.965

 ctr,wid   -2.54,  427.70
 height               161
 dev/cor    0.33    0.840
Top Hat              DATA
 Mean              ...+..
 Dev               ...+..
 Min               ...+..
 Max               ...+..
 Factor            ...+..

Near Field ........ mrad
(c)1995 Spiricon,Inc.

CURSOR
( 5900.00, 5700.00) =   155          Δ=          μm
GRID     2.00e+03μm       15:37:23  20 FEB 1909
Spiricon  37 CONT       VR/S -REF AVG STOPPED
                CALIBRATED   GAIN  37 BLACK 255
```

b)

```
D86e / Knife Edge   V5.15
 Total 86.47%        4557
 Peak           0     218
 Pk Loc  7000.00, 6400.00
 Center  6382.96, 5732.37
 Diameter       648.20μm
  X,Y    1443.91, 1830.32
Elliptical
 Orientation          ...
 Roundness           ....
Gauss Fit           WHOLE
 Center ........,........
 Width  ........,........
 Height            ...+..
 Dev/Cor  ......     ....

Top Hat              DATA
 Mean              ...+..
 Dev               ...+..
 Min               ...+..
 Max               ...+..
 Factor            ...+..

Near Field ........ mrad
(c)1995 Spiricon,Inc.

CURSOR
( 6200.00, 5400.00) =   200          Δ=          μm
GRID     2.00e+03μm REMOTE 14:31:39  23 FEB 1909
Spiricon   3 CONT       VR/S -REF AVG STOPPED
                CALIBRATED   GAIN   0 BLACK 255
```

Figure 1.5: Images of focused THz light generated by the FEL. The frequency is 1.53 THz in a) and 2.52 THz in b). As expected near the diffraction limit, the THz spot size decreases as the THz frequency increases.

The FEL is a quasi-continuous wave source, meaning it is a pulsed laser but the pulses are long enough that they contain millions of THz cycles per pulse and are not subject to a large amount of Fourier broadening. The pulse duration ranges from $\sim 1 - 10\,\mu$s with a repetition rate of 0.5-1.5 Hz. A spatial profile of the focused beam as measured by a Spiricon is shown in Figure 1.5. Though the FEL is continuously tunable, there are a number of frequencies in the tuning range which are heavily absorbed by water. The THz radiation from the FEL is transported to the user laboratories from the accelerator vault via an evacuated metal tube. There are multiple output ports in each lab to allow multiple THz experiments be setup at the same time, though only one experiment may use the FEL at any given time. To avoid purging or evacuating the THz beam path outside of the transport system, the work done was performed in “water windows” where the absorption due to water is minimal.

Chapter 2

FEL Sideband Spectrometer

UCSB currently has two high power, narrow band, free electron laser beams, the millimeter (MM) and far infrared (FIR) FELs. For a variety of reasons, it is necessary to be able to precisely measure the frequency of these lasers, but currently there is a lack of detectors with this capability. It is very difficult to do THz spectroscopy due to a lack of detectors and gratings that function efficiently at THz frequencies. The frequency of the THz radiation can be measured by an interferometer but there are problems with moving parts, a lack of high resolution and an inability to measure individual FEL pulses. We have proposed and developed a single shot, high resolution FEL upconversion spectrometer that requires no moving parts with a design that utilizes sum and difference frequency generation (SFG and DFG, respectively) in a nonlinear optical crystal to measure FEL frequencies.

2.1 Nonlinear Optics

In this section, we will discuss non linear optical phenomena. Non linear optical phenomena occur as a consequence of the modification of the optical properties of a system due to the presence of the light. The term “nonlinear” refers to the fact that the phenomena investigated are not linear in the electric field of the light, but rather has quadratic, cubic or higher order dependences. To better understand non linear effects, we can consider how the dipole moment per unit volume $\tilde{P}(t)$ of a material depends on the applied optical field strength $\tilde{E}(t)$. In linear materials, we have the well known relation that

$$\tilde{P}(t) = \chi^{(1)}\tilde{E}(t) \tag{2.1}$$

In non linear materials, the response can often be described by expressing the polarization $\tilde{P}(t)$ as a power series of the electric field $\tilde{E}(t)$ as

$$\begin{aligned}\tilde{P}(t) &= \chi^{(1)}\tilde{E}(t) + \chi^{(2)}\tilde{E}^2(t) + \chi^{(3)}\tilde{E}^3(t) + ... \\ &\equiv \tilde{P}^{(1)}(t) + \tilde{P}^{(2)}(t) + \tilde{P}^{(3)}(t) + ... \end{aligned} \tag{2.2}$$

where $\chi^{(2)}$ and $\chi^{(3)}$ are the second and third order non-linear optical susceptibilities, respectively. For simplicity, we have assumed $\tilde{P}(t)$ and $\tilde{E}(t)$ to be scalar quantities. The quantitites $\tilde{P}^{(2)}(t) = \chi^{(2)}\tilde{E}^2(t)$ and $\tilde{P}^{(3)}(t) = \chi^{(3)}\tilde{E}^3(t)$ are called the second and third order non-linear polarization, respectively. It is found that physical processes and effects due to the second order polarization are distinct from those caused by the third order non-linear polarization. Effects due to the second order non-linear polarization include second harmonic generation, sum and difference frequency generation, and optical parametric oscillation. Some effects due to the third order non linear polarization include third harmonic generation and self foucing due intensity dependence of the refractive index. We will briefly discuss the details of sum and difference frequency generation in the following section. These and other non-linear optical phenomena are well described in the book “Nonlinear Optics” by Robert W. Boyd[4].

2.1.1 Sum and Difference Frequency Generation

Sum and difference frequency generation is an effect which results from a non-zero second order non-linear polarization. When two monochromatic light fields are present in a material with a non-zero second order susceptibility, this susceptibility can mix the two frequencies to create light at a third frequency. Due to conservation of energy, the frequency of the generated light must be equal to the sum or difference of the two applied frequencies. If we assume that two disctinct frequencies of light given by

$$\tilde{E}_1(t) = E_1 e^{-i\omega_1 t} + c.c. \tag{2.3}$$

$$\tilde{E}_2(t) = E_2 e^{-i\omega_2 t} + c.c. \tag{2.4}$$

$$\tilde{E}(t) = \tilde{E}_1(\omega_1, t) + \tilde{E}_2(\omega_2, t) \tag{2.5}$$

are present in a second order non linear material such that

$$\tilde{P}^{(2)}(t) = \chi^{(2)}\tilde{E}^2(t) \tag{2.6}$$

we obtain an expression proportional to the following terms

$$\tilde{P}^{(2)}(t) = \chi^{(2)}[\tilde{E}_1^2(\omega_1, t) + \tilde{E}_2^2(\omega_2, t) + 2\tilde{E}_1(\omega_1, t)\tilde{E}_2(\omega_2, t)] \tag{2.7}$$

The first two terms only contain the individual frequencies of light applied. Due to the electric field being squared, these terms oscillated at twice the frequency of the respective fields, and these terms are resoponsible for second harmonic generation. The last term now contains cross terms of the two monochromatic fields and we find that

$$\tilde{P}^{(2)}(\omega_3, t) = 2\chi^{(2)}\tilde{E}_1(\omega_1, t)\tilde{E}_2(\omega_2, t) \tag{2.8}$$

has terms proportional to the sum of the applied frequencies $(\omega_1 + \omega_2)$ and the difference of the applied frequencies $(\omega_1 - \omega_2)$. For a fixed geometry, we can express the nonlinear polarization by the scalar relationship

$$P(\omega_3) = 4d_{eff}E(\omega_1)E(\omega_2) \tag{2.9}$$

where d_{eff} is the scalar effective value of the tensor for the second order nonlinear susceptibility $\chi^{(2)}$. It is easy to see that if $E(\omega_1)$ and $E(\omega_2)$ have both forward and backward propagating terms, $P(\omega_3)$ will have terms proportional to $\omega_3 = \omega_1 + \omega_2$ and $\omega_3 = \omega_1 - \omega_2$. A simple schematic is shown in Fig. 2.1. We can describe this process as the material absorbing two photons of different frequencies to create a third photon at the sum or difference of the two frequencies.

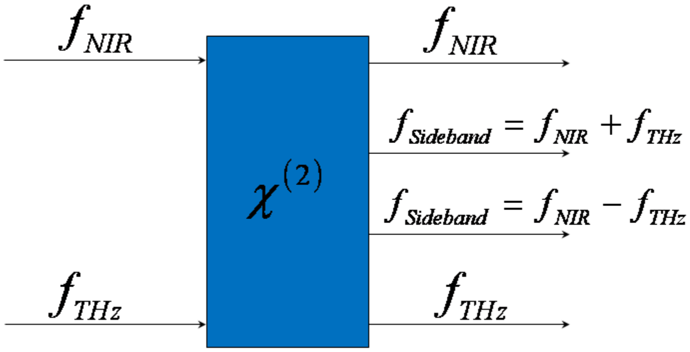

Figure 2.1: A simple schematic of sum and difference frequency generation in a second order non linear material.

We can wirte down an expression for the intensity of the light generated at the sum or difference frequencies. It is given by

$$I_3 = \frac{512\pi^5 d^2 I_1 I_2}{n_1 n_2 n_3 \lambda_3^2 c} L^2 \mathrm{sinc}^2(\Delta k L/2) \tag{2.10}$$

where I_1 and I_2 are the intensities of the two applied frequencies, respectively, d is the effective value of the second order susceptibility, L is the length of the crystal, n_1, n_2, and n_3 are the indeces of refraction at the three frequencies, respectively, and λ_3 is the wavelength of the newly generated light. In this equation, Δk represents the phase matching term. We can see that if Δk is close to zero, implying good phase matching, that the intensity of the generated light will increase with increasing crystal length L, as long as $\Delta k L/2$ is small. From this equation, it is possible to estimate the maximimum intensity of the generated light assuming the indeces of refraction are known at the applied frequencies. In our experiments, we will mix the THz from the FEL with a NIR light and will measure the frequency of the THz radiation from the difference between the fundemental NIR frequency and the sideband frequency.

2.1.1.1 Note on Phase Matching

We have mentioned that light is generated at the sum and difference of the frequencies of the applied fields due to conservation of energy. Similarly, we must also obey the conservation of momentum, leading to the follwoing expressions

$$\omega_3 = \omega_1 \pm \omega_2 \tag{2.11}$$

$$k_3 = k_1 \pm k_2 \tag{2.12}$$

$$\Delta k = k_3 - (k_1 \pm k_2) \tag{2.13}$$

However, we can relate the wavevector k to the frequency ω to obtain the following

$$\Delta k = \frac{\omega_3}{n_3} - (\frac{\omega_1}{n_1} \pm \frac{\omega_2}{n_2}) \tag{2.14}$$

We can see that unless $n_1 = n_2 = n_3$ the phase mismatch will be non zero and the new light can only be coherently generated in a limited length of sample. There is a simple physical description that helps understand why we can only generates sideband sin a certain length of crystal. Because of the mismatch of speeds between different frequencies of light in the sample, light generated at the front of the sample can be at a different phase than light created further into the sample. Becuase of the law of superposition, the fields can add constructively or destructively. The coherence length $L_c = {}^2/_{\Delta k}$ is the length where the fields begin to add destructively, and the length of crystal which can produce the strongest intensity of new light.

2.1.2 Higher Order Processes and Sideband Generation

From equation 2.2, we can see the the polarization in a sample is the sum of the linear polarization plus the polarization due to the higher order susceptibilities. We have seen in the previous section that the second order susceptibility is responsible for mixing two phtons to create a third photon. Similarly, the third

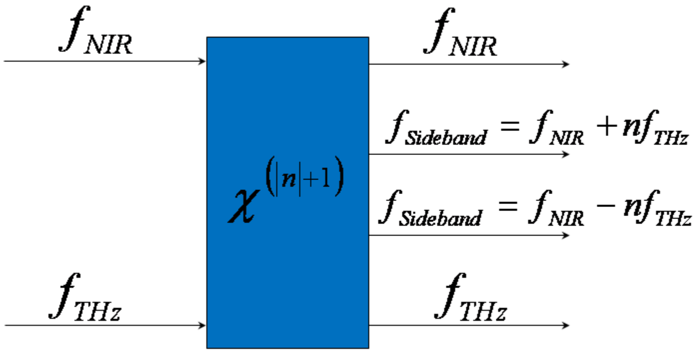

Figure 2.2: A simple schematic of sideband generation in a n^{th} order non linear material.

order susceptibility is responsible for mixing three photons to create a fourth photon. In general, an n^{th} order process will mix n photons to create a new photon. Because the n^{th} order process requires n photons, higher order processes will need more intense fields to observe. One example of a higher order process is sideband generation, which is diagrammed in Fig. 2.2.

Sideband generation is very similar to sum and difference frequency generation, and when an intense THz field is mixed with a NIR field in sum and difference frequency generation, sidebbands of the NIR light are observed. Sidebands are new light separated from the fundemental laser (which is often linear) by multiples of the drivinig frequency (non linear). Experiments at the UCSB free electron laser are often performed with a NIR fundemental laser and an intense THz laser. Sidebands are new light generated at frequencies $f_{Sideband} = f_{NIR} + nf_{THz}$ for an $n+1$ order process. This is an $n+1$ order process because it mixes n THz photons with one NIR photon. Because this process takes n THz photons, we find that the intensity of the light emmited at $f_{Sideband}$ is proportional to

$$I_{Sideband} \propto I_{THz}^{n} \tag{2.15}$$

We therefore expect higher order non linear phenomena and sidebands to be much more difficult to observe as they require much more intense fields. Though this perturbative model describes many systems well, we want to be clear these expressions are not valid in all circumstances.

2.2 Measurements of the FEL Frequency

The frequency of the UCSB FELs is tuned by varying the terminal voltage of a National Electrostatics Corporation electrostatic accelerator between 2 and 6 MV. Precise knowledge of the FEL frequency is important to any experiment that uses a FEL, and as in any laser system, it is desirable to accurately calibrate the laser source. We have recently been able to measure the FEL frequency at a number of different terminal voltages, giving us the ability to calibrate the FELs with high precision.

Sum and difference frequency generation is a second order non-linear optical process, which makes it necessary to use a crystal with a large second order dielectric susceptibility in order to achieve high conversion efficiencies. We can estimate the maximum power that will be generated during sum and difference frequency generation by using the planewave fixed-field approximation[5], assuming that the power generated does not deplete the pump laser:

$$P_{SFG} = \frac{2^5 \pi^5 d_{eff}^2 P_{NIR} P_{THz}}{\epsilon_0 c n_{THz} n_{NIR}^2 \lambda_{SFG}^2 A \left|\Delta k\right|^2} \tag{2.16}$$

Here, d_{eff} is the magnitude of the second order dielectric succeptibility and A is the area of the THz spot. We can see that the power is strongly dependent on Δk, which is the phase matching condition discussed in section 2.1.1.1.

The tunable Titanium:Sapphire laser gave us the ability to change wavelengths between 800nm and 935nm to minimize the phase mismatch and maximize our signal. The power generated during an individual FEL pulse by sum or difference frequency generation in a GaP $\langle 110 \rangle$ crystal ranges from hundreds of nW to tens of µW depending on the FEL frequency and pump beam powers. Table 2.1 shows the approximate predicted values and measured values of SFG power assuming the following values: $P_{NIR} = 10$ mW, $P_{FEL} = 100$ W, $d_{eff} = 100$ ${}^{pm}/{}_{V}$[6], $A = 1\,mm^2$and $\lambda_{SFG} \approx \lambda_{NIR} = 925$ nm. Though the predicted values for the power of a sum or difference frequency sideband are higher than the actual values, they are still within about one order of magnitude of the measured power and we believe the previous equation provides a reasonable approximation of our system.

FEL Frequency (THz)	FEL Frequency (cm^{-1})	Predicted SFG Power (μW)	Approximate Measured Power (μW)
0.3	10	350	30
0.6	20	200	10
1.5	50	30	2
3	100	6	.75 (at 84 cm^{-1})

Table 2.1: Predicted and measured values of SFG power for a number of FEL frequencies

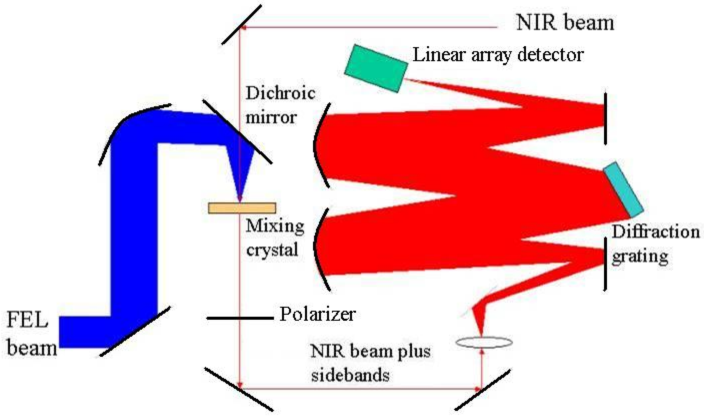

Figure 2.3: Schematic of the experimental setup of the mixing crystal and spectrometer.

2.2.1 Experimental setup and results

The FEL radiation is collected by a 4" focal length, 2" clear aperture parabolic mirror, reflected by a dichroic mirror (ITO coated glass), and then focused onto a GaP mixing crystal. A 0.5 mm GaP $\langle 110 \rangle$ crystal is mounted in a rotation stage to optimize the polarization of the generated radiation. The THz and NIR beams are orthoganally polarized with the THz aligned along the $[-110]$ axis for the maximum signal.

The NIR radiation is provided by a Coherent 890 Titanum:Sapphire laser which is fiber coupled to the experiment by a 62 μm core cable. The NIR radiation then passes through a Glan Taylor polarizer set to transmit vertically polarized light. The NIR and FEL radiation are mixed at the dichroic mirror and fall onto the mixing crystal. The sum and difference frequency radiation propagates collinear to the NIR beam but has a polarization dependent on the orientation of the mixing crystal. A Glan Taylor polarizer set to transmit horizontally polarized light attenuates the vertically polarized NIR beam, and the mixing crystal is adjusted so that the sidebands are transmitted.

The NIR beam is focused into the Czerny-Turner spectrometer using a 20 mm focal length lens, is then collimated by a 0.75 m focal length mirror, strikes a 50 mm wide diffraction grating and then the first order beam is sent to a 1 m focal length mirror and focused onto a linear CCD array (see Figure 2.3). This diffraction grating has 1800 $^{grooves}/_{mm}$, which gives us a resolving power of 90000, and leads to a maximum resolution of 0.1 cm^{-1} at NIR frequencies.

An Ocean Optics USB4000 card utilizes a 3648 pixel linear CCD array with each pixel having a width of 8 μm. The detector is run in hardware-triggered mode with a shutter time of 10 μs and is externally triggered by the FEL advanced trigger. The FEL pulse is usually between 3-8 μs and is timed such that the detector collects the full pulse during the 10 μs when the shutter is open. We use

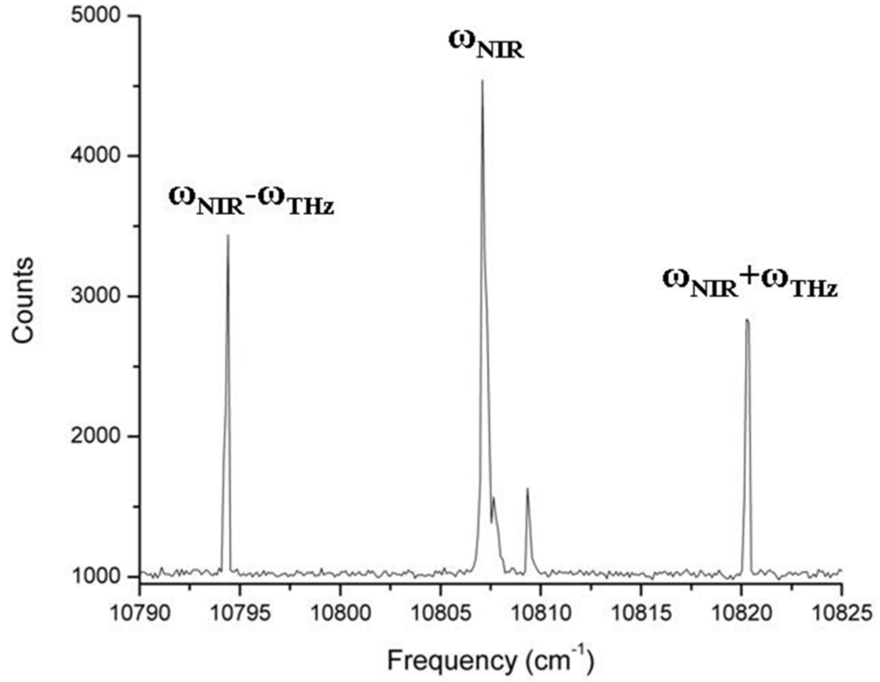

Figure 2.4: The spectrum of the NIR laser showing sum and difference frequency generation during a single $13\,cm^{-1}$ FEL pulse. The small peak at $10810\ cm^{-1}$ is a second Titanium:Sapphire laser mode.

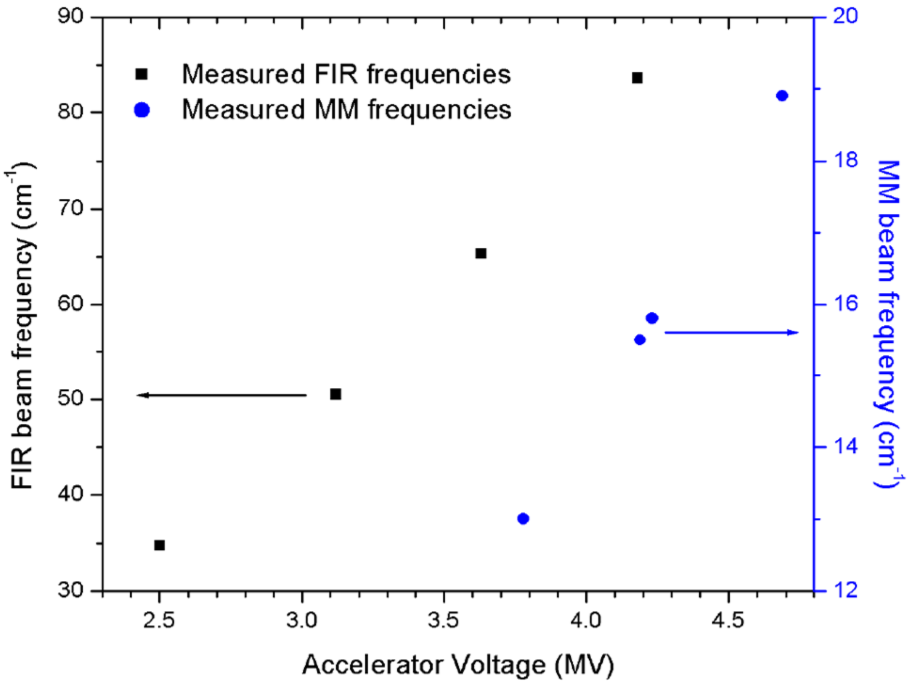

Figure 2.5: Plot of FEL frequency vs. accelerator voltage for the FIR and MM free electron lasers.

peak detect programs in Labview to find the difference in frequency between the NIR and sideband peaks, which yields us the FEL frequency.

We care been able to make single shot measurements of individual FEL pulses with resolution as good as 0.1 cm^{-1} at frequencies between 13 and 20 cm^{-1} on the MM FEL and between 35 and 85 cm^{-1} on the FIR FEL. For a sideband generated during an individual FEL pulse, we are able to obtain signal to noise ratios of better than 10:1 at 50 cm^{-1} and 100:1 at 13 cm^{-1} (see Fig. 2.4). Using these measured frequencies, we are able to perform highly precise calibrations of the Millimeter and Far Infrared FELs.

2.2.2 Conclusions

By using sum and difference frequency generation in a GaP crystal, we have demonstrated the ability to measure the frequency of individual THz pulses from a Free Electron Laser with 0.1 cm^{-1} resolution using a single shot THz upconversion spectrometer. Measurements have been used to calibrate the frequency of the FEL with respect to the voltage, and the setup can be used at anytime to measure the frequency of the FEL if it is active.

Chapter 3

Autler-Townes Splitting in InGaAs Quantum Wells

Strong interactions between light and matter are historically and currently of great interest in condensed matter, atomic and molecular physics, as well as in quantum information science. In the strong coupling regime, effects of the light–matter interaction can be manifested as coherent Rabi oscillations between a pair of quantum states[7,8], vacuum Rabi splitting of two-state quantum systems in a cavity[9,10,11], and the Autler–Townes effect in three-state quantum systems[12,13,14,15,16,17,18,19,20]. As many of these systems have proposed uses in the coherent control of states and in quantum information processing[21], further studies of light–matter coupling pave the way for future technology. Recently, cavity-coupled semiconductor[22,23] and superconductor[24] systems have achieved the ultrastrong coupling regime, where the photon exchange between the quantum system and optical field occurs at a rate (given by the Rabi frequency, Ω_{Rabi}) comparable to the frequency of the quantum transition ω_{21}. Though ultrastrong coupling has been difficult to achieve in the past, recent experiments open the door to investigate effects such as the Bloch–Siegert shift[25,26,27,28] which are expected to become observable in this regime. With an intense terahertz (THz) field incident upon a semiconductor quantum well, we are able to vary the light–matter coupling strength and investigate the ultrastrong coupling limit without a cavity.

Here, we investigate the near infrared interband absorption of semiconductor quantum wells driven by intense THz radiation in the regime of ultrastrong coupling, where the Rabi frequency Ω_{Rabi} is a significant fraction of the frequency of the strongly driven transition ω_{21}. With the driving frequency tuned just below the lowest frequency transition between valence subbands, a particularly interesting phenomenon is observed. As the THz power increases, a new peak emerges above the frequency of the undriven exciton peak, which grows and eventually becomes the larger of the two. This reversal of relative peak intensity is inconsistent with the Autler–Townes effect in a three-state system while within the rotating wave approximation (RWA). In the samples investigated, the Bloch–Siegert shift (associated with the reintroduction of terms dropped in the RWA), exciton binding energy, the Rabi energy, and non-resonant ac Stark effects are all of comparable magnitude. Solution of a semiconductor Bloch model with one conduction and multiple valence subbands indicates that the ac Stark effect is predominantly responsible for the observed phenomenon, but other effects are not negligible in this regime.

3.1 Experimental Methods

We will be investigating the strong coupling of a quantum well system to an intense electromagnetic field. Using weak NIR light, we optically create excitons in an InGaAs quantum well and drive an interexcitonic transition with an intense THz field. The NIR absorption is a probe of the quantum well states, and changes to the absorption spectra are caused by the strong interaction of the quantum wells with the THz radiation. Careful investigation of the changes induced by intense THz fields will show that the observed phenomena extends beyond the approximations often used to describe these systems, the two level and rotating wave approximations. A description of the experimental design is detailed in the follwoing section.

3.1.1 Samples

The samples grown for these the experiments were number # 081224C (18 nm) and # 090405 (22 nm), grown by Tuan Truong in the Petroff group. The samples consist of 10 repetitions of 18 or 22 nm analog $In_{0.06}Ga_{0.94}As$ quantum wells surrounded by 30 nm $Al_{0.3}Ga_{0.7}As$ barriers.

3.1.1.1 Sample Design

In order to investigate strong coupling in InGaAs quantum wells, we need to be able to resonantly probe the system with THz from the UCSB Free Electron Laser and the transition we are probing must have a strong oscillator strength. For the samples investigated in the following section, minimal processing is necessary. As will be explained later, the sole process is a metallization of the top of the sample with aluminum and no special care was taken to simplify this minimal process.

We have investigated the coupling of an intersubband transition in a quantum well to a strong THz field. In order to simplify our results, a system must be designed where the transitions we are interested in studying differ greatly in energy from the next nearest transition. For the following experiments that means that we must have a distinct interband and a distinct intersubband transition. Due to the drastically differeng effective masses for the electron, light hole and heavy hole in the InGaAs quantum well system, the intersubband transitions have largely different energy levels. Becuase the heavy hole has the largest effective mass, it has the subbands with the smallest spacing and therefore the lowest energy transition in a quantum well. By applying a frequency that is resonant with the lowest heavy hole transition, we know we will be far from resonance of other transitions and we will be interacting mainly with the two level system we are interested in understanding.

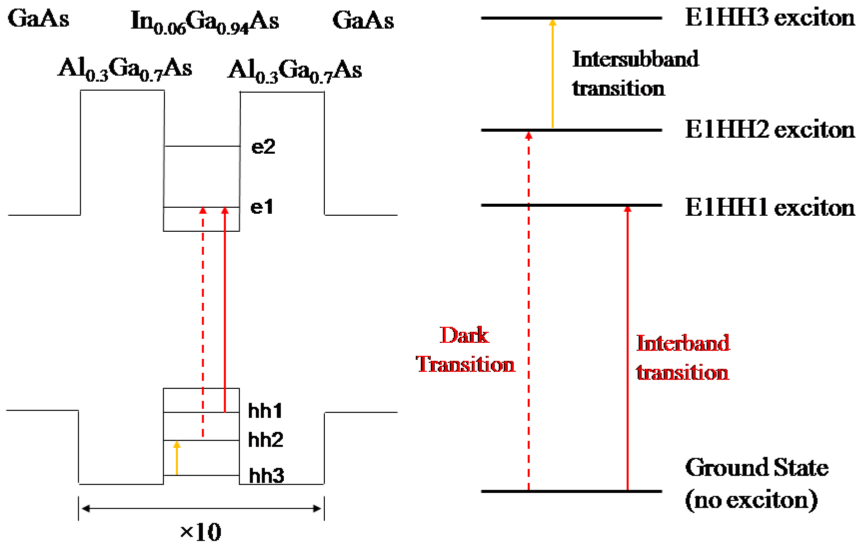

Figure 3.1: Energy level diagrams of the quantum well systems investigated. The left graphic shows the transitions in the single electron model while the diagram on the right is in the exciton reference frame where the zero energy ground state is when there is no exciton present. Without optical excitation, the valence band is full and the conduction band is empty and transitions will not occur unless an electron is excited across the band, implying that the lowest transition is the creation of an exciton between the highest heavy hole band and the lowest conduction band.

Unfortunately, the lowest heavy hole and light hole bands are essentially degenerate in the GaAs system, making it difficult to decouple the effects observed. In order to avoid this effect, the active region of our quantum well was grown as an $\mathrm{In_{0.06}Ga_{0.94}As}$ alloy. Due to the lattice mismatch between GaAs and InAs, the addition of a small amount of indium adds a significant amount of strain in the sample and breaks the degeneracy of the heavy and light holes. Strain shifts the light hole subband below the heavy hole subband by $> 20\,meV$. Additionally, because InAs has a significantly lower band gap than GaAs, the inclusion of this small amount of indium shifts the lowest interband transition in the InGaAs quantum well to be much lower than the band gap of the GaAs substrate. This allows us to investigate the absorption due to excitons in the quantum well while not worrying about strong absorption from the substrate (Fig. 3.2).

All samples investigated were grown by molecular beam epitaxy (MBE) on campus at UC Santa Barbara. The 15 nm quantum well was grown by Chad Wang in the group of L. C. Coldren while the 18 and 22 nm wells were grown by Tuan Truong in the P. M. Petroff group. All of the samples were grown with $\mathrm{In_{0.06}Ga_{0.94}As}$ quantum wells and $\mathrm{Al_{0.3}Ga_{0.7}As}$ barriers. Samples investigated were grown with 10 repetitions of quantum wells, increasing the absorption and exciton generation necessary for good results in the follwoing experiments. However, the large number of wells introduces some distribution in the well width and leads

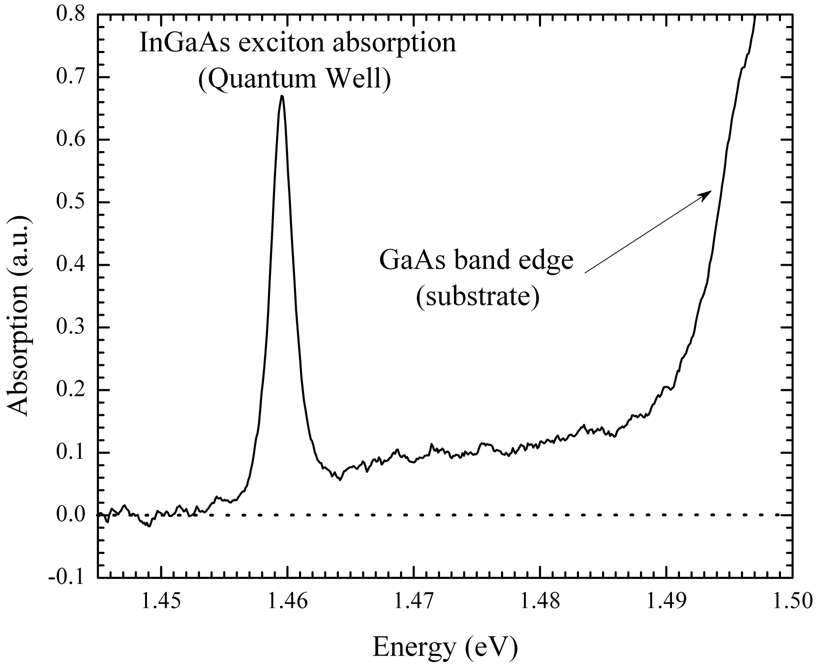

Figure 3.2: Due to the small band gap of InAs and the addition of indium into the quantum well, we see that the quantum well exciton is at a significantly lower energy than the GaAs band edge. This allows us to decouple quantum well effects from any effects due to the GaAs substrate.

to broadening of the observed absorption line. Homogeneous and inhomogeneous broadening will be discussed in more detail in section 3.3.2.2.

3.1.1.2 18 and 22 nm InGaAs Quantum Wells

Using the infinite square well model, we can calculate the intersubband transition energies in the quantum well. Using this model we estimate the lowest heavy hole transition in the 22 nm quantum well to be 5.3 meV and the lowest transition in the 18 nm quantum well to be 9.5 meV.

We can also calculate the dipole moments from the infinite square well model. For an intersubband transition the dipole moment μ is given by $e\langle z\rangle$, where e is the electric charge and $\langle z\rangle$ is the matrix element of the position operator in the growth direction. For the 22 nm QW, the dipole moments of the two lowest transitions are z_{21} = 3.97 nm and z_{32} =4.28 nm. The 18 nm QW has z_{21} =3.24 nm and z_{32} =3.50 nm. These dipole moments are very useful in verifying that the electric fields being used in the SBE calculations are consistent with what we believe we are applying experimentally.

3.1.1.3 Optical Coupling into the Samples

The NIR light acts as the quantum well probe in this transmission experiment. We observe changes to the NIR absorption as we vary the intensity of the THz radiation. Near IR light is applied at frequencies near to the exciton absorption frequency and must be polarized in the plane of the quantum well, as discussed in

1.1.2. In order to maximize the absorption of the quantum well active region, a thin layer of aluminum is deposited on the top side of the sample. This allows the NIR probe to enter through the substrate, travel through the active region, reflect of the aluminum, pass through the active region a second time and be collected from the backside of the sample.

In order to couple to the intersubband transitions in the quantum well, the THz light must be polarized in the growth direction of the sample. The THz radiation is therefore coupled in via the facet of the sample. In order to maximize the THz intensity at the quantum well active region, the THz is focused in at an angle of $\sim 15°$. The aluminum layer on the front side of the sample again proves to be beneficial as it forces the THz electric field to be in the growth direction of the sample. The boundary condition at the metal interface eliminates in-plane fields and gives constructive interference for fields in the growth-direction.

3.1.2 Experimental Setup

A brief description of the experimental setup and detailed description of the sample geometry. A diagram of the experimental setup can be found in Figure 3.3.

3.1.2.1 Experiment

The THz radiation exiting the transport system is split with a mylar thin film beamsplitter where less than 10% of the power is sent to a pyroelectric detector and the rest is focused on the sample using an off-axis parabolic mirror (OAP). Often a lens made of TPX (polymethylpentene) is used at the exit port of the transport system to correct for dispersion and to slightly decrease the size of the beam at the OAP. The radiation focused on the pyroelectric detector is monitored using an oscilliscope for rough measurement of the THz power.

The NIR probe of the sample is performed using a LED with peak intensity at $\sim$ 835nm. The LED is capable of providing 1mW of power at the sample and can be focused down to a spot of $\sim 300-400\mu$m in diameter. The light is coupled via fiber to the experimental setup. The light is then focused onto the sample where it reflects of the deposited aluminum layer, travels back the direction it came from and is collected by a separate fiber coupler to be analyzed by a Acton 0.275 meter triple grating monochromator and Princeton Instruments Intensified CCD spectrometer (ICCD). The ICCD spectrometer is equipped with both 300 and 1200 lines/mm gratings and the resolution with the 1200 lines/mm grating is greater than 2nm ($\sim$ 0.5 eV). The ICCD detector is similar to a photomultiplier tube in that it amplifies electrons ejected from a photocathode, but allows for frequency resolution by detecting an entire spectrum at once using the CCD. The signal is intensified when a high-voltage pulse is applied to the detector. This

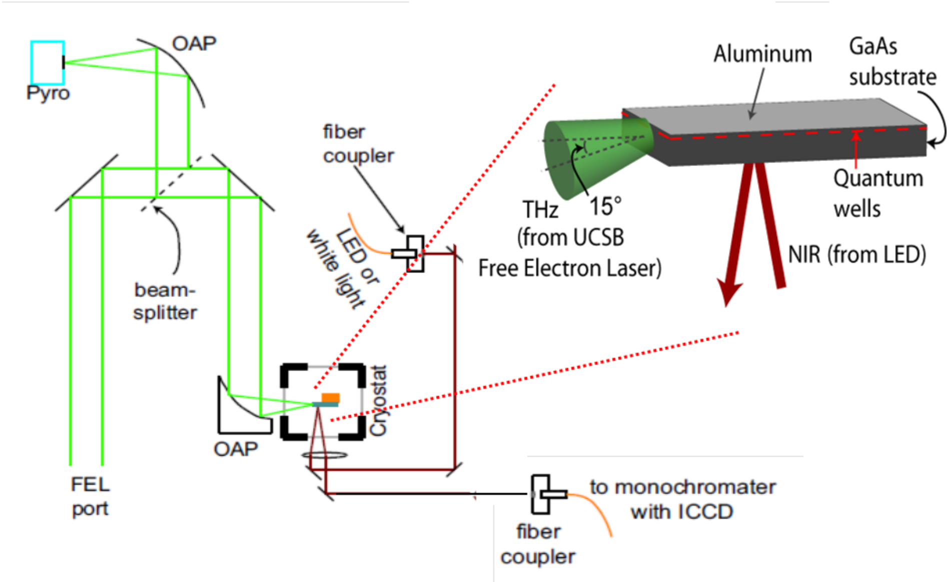

Figure 3.3: Illustration of the experimental setup. A blown up diagram of the sample geometry is shown in the upper right corner.

pulse may also be used to gate the detection on time scales as short as a few ns, particularly useful for investigations using the FEL cavity dump setup. The ICCD is cooled with a TE-cooler, reducing dark counts.

The sample is in general cooled to 10K. It is mounted in a CTI Cryogenics Model 22 closed-cycle Helium refrigerator which at best is capable of cooling the sample to 7-8K. The cryostat is connected to a CTI Cryogenics Model 8200 Helium compressor through two high pressure Helium lines. It is also connected to the controller built into the compressor and to a Lakeshore 330 temperature controller. The sample is mounted on copper plate using either rubber cement or Apiezon N vacuum grease. In general the rubber cement is easier to handle and remove, but the best thermal contact seems to be achieved using the vacuum grease. The sample mount is connected to the coldfinger through a separate semi-permanent copper stage. Applying a small amount of Apiezon N grease between the coldfinger and this mount also tends to increase the base temperature.

A Lakeshore temperature diode is screwed in to the top of the sample mount. At the base of the semi-permanent copper stage a Nichrome heating wire is wrapped and hooked in to the temperature controller. Once cold, the cryostat is capable of staying at low temperature for 2-3 days.

3.1.2.2 THz Beam Diagnostics

Measurement of the THz energy in the FEL pulses was performed with a Laser Precision Corp. RJ-7620 energy ratiometer. The FEL pulse duration is observed by a pyroelectric detector and an oscilliscope simultaneously to the measurements. By dividing the pulse energy by the pulse duration (measured from the scope), an estimate of the THz power can be made. Additionally, the spatial profile of the THz at the focus of an off-axis parabolic can be measured by a Spiricon pyroelectric imaging system. The FEL beam is $\sim 2-3$ inches in diameter as it exits the FEL port and is fairly low intensity, so focusing is often required for measurement. As expected near the diffraction limit, the spot size scales with the wavelength of the radiation and beam diamaters range from $\sim$ 0.5mm at 3.5 THz to $\sim$ 1mm at 500 GHz. The spatial profile of the beam can be combined with the THz power to obtain the approximate THz intensity. Estimates of the THz intensity are then used to estimate the electric field at the focus of the THz beam.

3.2 Theoretical Background

A brief description and overview of the physics neccessary to understand the phenomenon under investigation. The two level model interacting with an electromagnetic field and its limitations will be discussed.

3.2.1 Light Interacting with a Two Level System

Let us assume that we are looking only at a two level system containing the two lowest heavy hole excitons. We have discussed the exciton states in Chapter 1, however, in the presence of a strong electromagnetic field, the states are modified. Let us consider the solution to the Schrodinger equation for a two level system in an intense oscillating field. The exciton wavefunction will be given by ψ, where

$$i\hbar\frac{\partial\psi}{\partial t} = \hat{H}\psi \tag{3.1}$$

and the Hamiltonian operator $\hat{H}$ given by

$$\hat{H} = \hat{H}_0 + \hat{V}(t) \tag{3.2}$$

Here, H_0 represents the Hamiltonian of the exciton system in the absence of an oscillating field and $\hat{V}(t)$ represents the interaction with the applied field. As is discussed in Chapter 1, we make the dipole approximation to obtain

$$\hat{V}(t) = -\hat{\mu}\tilde{E}(t) \tag{3.3}$$

where the dipole moment operator is given by $\hat{\mu} = e\hat{r}$. Assuming we are coupling to quantum well transitions by applying the electric field in the growth direction, the dipole should only depend on the quantum well part of the wavefunction and we can estimate the dipole moment $\hat{\mu}$ between the initial state ψ_i and final state ψ_f:

$$\begin{aligned}\hat{\mu} = \langle \psi_i \mid ez \mid \psi_f \rangle \, \hat{z} &= \langle \psi_i(x,y) \mid \psi_f(x,y) \rangle \langle \phi_i(z) \mid ez \mid \phi_f(z) \rangle \, \hat{z} \\ &= \langle \phi_i(z) \mid ez \mid \phi_f(z) \rangle \, \hat{z} \end{aligned} \tag{3.4}$$

Because this is an intersubband transition, the wavefuntion in the x-y plane which is dependent on the Bloch wavefuntions are the same for the initial and final states and the dipole moment can be obtained simply from the quantum well matrix element of the position operator between states.

We assume that the field applied is $\tilde{E}(t) = Ee^{-i\omega t}$+c.c, where E is a constant, and the frequency ω is nearly resonant with the transition between the lowest heavy hole state a and the first heavy hole excited state b. A simple diagram of the exciton energy levels is given in Figure 3.4. Since the effect of the interaction is to mix states a and b, the wavefunction in the presence of the field can be represented as

$$\psi(\mathbf{r},t) = C_a(t)u_a(\mathbf{r})e^{-i\omega_a t} + C_b(t)u_b(\mathbf{r})e^{-i\omega_b t} \tag{3.5}$$

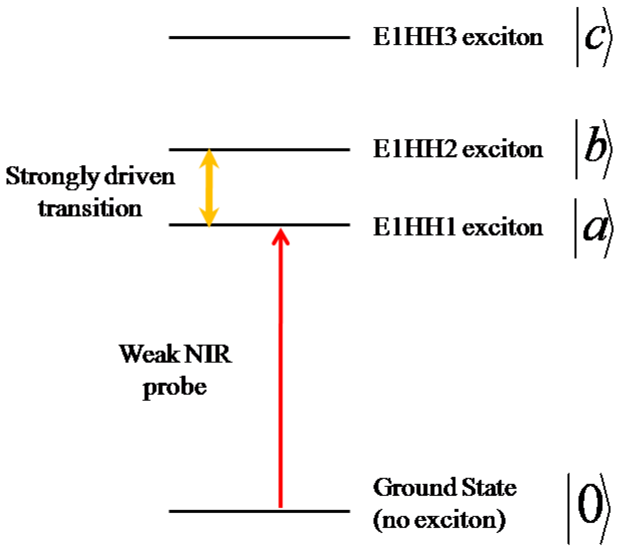

Figure 3.4: A simple diagram of the energy levels in the quantum well exciton system. The strongly driven transition is between the heavy hole states a and b. The weak NIR beam probes the energies near state a, the lowest energy exction. The NIR light emitting diode used is broad enough to probe both the E1HH1 and E1HH2 excitons, however the E1HH2 absorption is dissallowed by selection rules and only the E1HH1 exciton is observed.

Here $u_a(\mathbf{r})e^{-i\omega_a t}$ represents the excited wavefunction of the ground state a and $u_b(\mathbf{r})e^{-i\omega_b t}$ represents the excited wavefunction b, assumed to be orthonormal. The quantities $C_a(t)$ and $C_b(t)$ can be interpereted as the probability amplitudes that at time t that the exciton is in state a or b, respectively.

By inserting equation 3.5 into equation 3.1, it is possible to obtain the following relations:

$$\dot{C}_a = \frac{1}{i\hbar} C_b V_{ab} e^{-i\omega_{ba} t} \tag{3.6}$$

$$\dot{C}_b = \frac{1}{i\hbar} C_a V_{ba} e^{-i\omega_{ab} t} \tag{3.7}$$

$$V_{ab} = V_{ba}^* = \left\langle a \mid \hat{V} \mid b \right\rangle \tag{3.8}$$

We will know explicitly introduce the interaction Hamiltonian and represent the matrix elements as

$$V_{ab}^* = V_{ba} = -\mu_{ba}\tilde{E}(t) = -\mu_{ba}(Ee^{-i\omega t} + E^* e^{i\omega t}) \tag{3.9}$$

Equations 3.6 and 3.7 then become

$$\dot{C}_a = \frac{-\mu_{ab}}{i\hbar} C_b (E^* e^{-i(\omega_{ba}-\omega)t} + Ee^{-i(\omega_{ba}+\omega)t}) \tag{3.10}$$

$$\dot{C}_b = \frac{-\mu_{ba}}{i\hbar} C_a (Ee^{i(\omega_{ba}-\omega)t} + E^* e^{i(\omega_{ba}+\omega)t}) \tag{3.11}$$

Here we have the equations describing the time dependent population of teh levels in our two level system. To obatian an exact result, approximations must be made which will be discussed in the following section.

3.2.2 Rotating Wave Approximation

These equations can not be solved analytically as they are now, and we will perform what is reffered to as the rotating wave approximation (RWA). We can see that both equaitons 3.10 and 3.11 have two terms, one dependent on the sum of ω and ω_{ba}, one dependent on the difference. Because we have assumed that our driving field $\omega \approx \omega_{ba}$, we have one term that oscillates slowly and and one rapidly oscillating term. Over any significant timescale, we assume that the rapidly oscillating term will average to zero and can therefore be neglected. We perform the rotating wave approximation by dropping the rapidly oscillating terms from equaitons 3.10 and 3.11, leaving us with the following relation

$$\dot{C}_a = \frac{i\mu_{ab}E^*}{\hbar} C_b e^{-i\Delta t} \tag{3.12}$$

$$\dot{C}_b = \frac{i\mu_{ba}E}{\hbar} C_a e^{i\Delta t} \tag{3.13}$$

$$\Delta = \omega - \omega_{ba} \tag{3.14}$$

where Δ is the detuning of the applied field from the resonance of the transition. This set of coupled equations can now be solved explicitly. We introduce both the Rabi frequency Ω and the generalized Rabi frequency Ω'

$$\Omega = \frac{2\mu_{ba}E}{\hbar} \tag{3.15}$$

$$\Omega' = \sqrt{(\mid \Omega \mid^2 + \Delta^2} \tag{3.16}$$

We can write down the general solution for equations 3.12 and 3.13 as

$$C_a(t) = e^{(1/2)i\Delta t}(A_+ e^{-(1/2)i\Omega' t} + A_- e^{(1/2)i\Omega' t}) \tag{3.17}$$

$$C_b(t) = e^{(1/2)i\Delta t}(\frac{\Delta - \Omega'}{\Omega^*}A_+ e^{-(1/2)i\Omega' t} + \frac{\Delta + \Omega'}{\Omega^*}A_- e^{(1/2)i\Omega' t}) \tag{3.18}$$

where A_+ and A_- are constants of integration dependent on initial conditions. The next section will focus on a particular set of initial conditions that is relevant to the exciton system.

3.2.3 Dressed States

Dressed states are a solution to the schrodinger equation with the characteristic feature that their probability to be in state a (or b) is constant in time. Consequently, the probability amplitudes $C_a(t)$ and $C_b(t)$ can only have time dependent phase factors. From equations 3.12 and 3.13, we can see the two possible solutions are given by

$$\psi_+ \rightarrow A_+ = 1,\ A_- = 0 \tag{3.19}$$

$$\psi_- \rightarrow A_+ = 0,\ A_- = 1 \tag{3.20}$$

By combining equations 3.5, 3.17 and 3.18 with the previous equations, we can explicitly write out the dressed state wavefunctions

$$\begin{aligned}\psi_\pm = {} & \frac{\Omega^*}{\Omega'}[\frac{\Omega'}{2(\Omega' \mp \Delta)}]^{1/2} u_a(\mathbf{r})\exp[-i(\omega_a - \frac{1}{2}\Delta \pm \frac{1}{2}\Omega')t] \\ & \mp[\frac{\Omega' \mp \Delta}{2\Omega'}]^{1/2} u_b(\mathbf{r})\exp[-i(\omega_b + \frac{1}{2}\Delta \pm \frac{1}{2}\Omega')t]\end{aligned} \tag{3.21}$$

We can now examine some of the properties of dressed states. We can determine the probability of finding the the exciton in state a to be

$$|\langle a \mid \psi_\pm\rangle|^2 = \frac{|\Omega|^2}{2\Omega'(\Omega' \mp \Delta)} \tag{3.22}$$

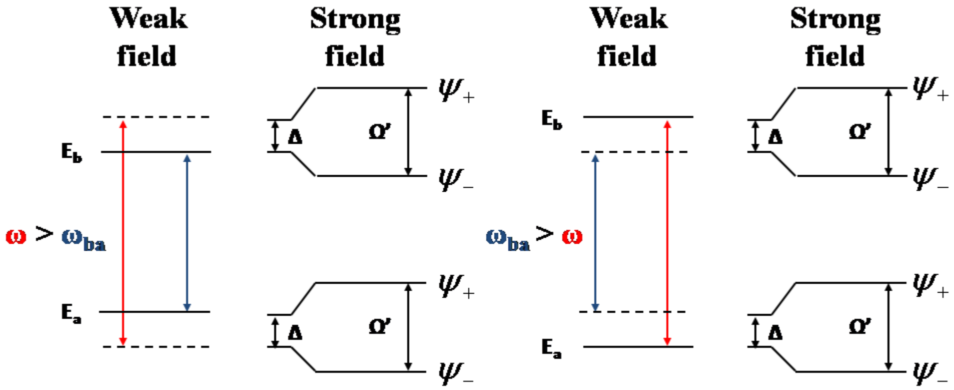

$$\Delta = \omega - \omega_{ba}$$

$$\Omega' = \sqrt{|\Omega|^2 + \Delta^2}$$

$$\Omega = \frac{2\mu_{ba}E}{\hbar} = Rabi\,Frequency$$

Figure 3.5: A diagram of the dressed states in a two level system interacting with an intense electromagnetic field. On the left, the applied field is higher frequency than the resonant frequency and the right shows the system with an applied field at lower frequency than the resonance. Under the weak field labels, the solid lines represent the initial exciton levels and the dashed lines represent the photon energy. Under the strong field label, the energy levels are identified by the dressed states $\psi_+$and ψ_-.

and the probability of finding the exciton in state b to be

$$|\langle b \mid \psi_{\pm}\rangle|^2 = \frac{\Omega' \pm \Delta}{2\Omega'} \tag{3.23}$$

We note that these probabilities are time-independent and that the dressed states are stationary states of the exciton-light system. The dipole transition moment between the two dresssed states is given as

$$\langle \psi_{\pm} \mid \hat{\mu} \mid \psi_{\mp}\rangle = \pm\mu_{ab}\frac{\Omega}{2\Omega'}(\frac{\Omega' \pm \Delta}{\Omega' \mp \Delta})^{1/2}e^{-i(\omega\mp\Omega')t}$$

$$\mp\mu_{ba}\frac{\Omega^*}{2\Omega'}(\frac{\Omega' \mp \Delta}{\Omega' \pm \Delta})^{1/2}e^{i(\omega\mp\Omega')t} \tag{3.24}$$

Properties of the dressed states are detailed by the energy level diagram in Fig. 3.5 for both a positive and negative detuning Δ. In the following section, we will address how dressed states are observed in the quantum well exciton system.

Another way to further understand dressed states is by plotting the two energies E_a, the energy of the ground state, and $E_b - \hbar\omega$, the energy of the excited state minus the photon energy of the driving field. In the absence of coupling between these to states, we expect E_a to remain constant and $E_b - \hbar\omega$ to decrease linearly with ω. The should cross when $E_b - \hbar\omega = E_a$ and eventually $E_b - \hbar\omega$ will be less than E_a. This is illustrated by the dashed lines in Fig. 3.6. However, the coupling between the two levels in our system is given by the Rabi energy $\hbar\Omega = 2\mu_{ba}E$ and we observe the anti-crossing behavior which is a characteristic of strongly coupled systems. The solid lines in Fig. 3.6 represent the same energy levels, however, we include the coupling between states in this calculation. We see

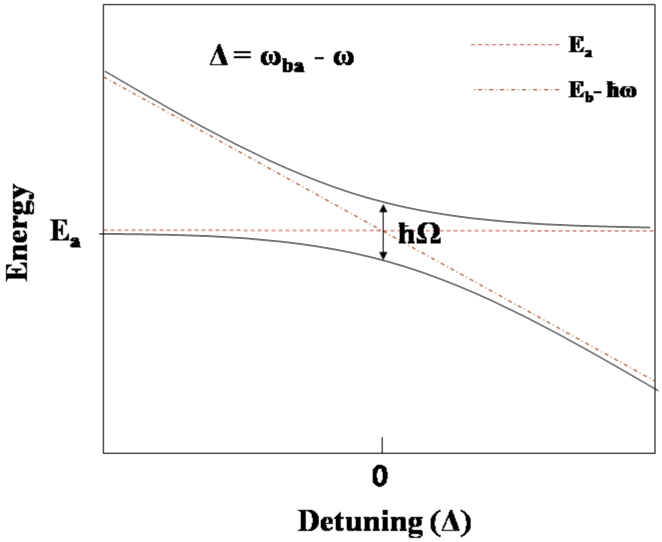

Figure 3.6: A diagram of the energy levels in a two level system interacting with an intense field. The dashed lines show the energies E_a and $E_b - \hbar\omega$ as a function of the detuning Δ with no coupling between the states. The solid lines are the same states where there is coupling between the two levels. In this case, we get the characteristic anti-crossing behavior, and the splitting at zero detuning is given by $\hbar\Omega = 2\mu_{ba}E$.

that at large values of detuning the solid and dashed lines nearly overlap and the energy levels are not shifted much, but as we approach $\Delta = 0$, the anti-crossing is clear and the two levels are separated by the Rabi energy $\hbar\Omega$. From this diagram, we can see that if we drive the system resonantly and probe the energies near state a, we will see two absorption peaks separated by $\hbar\Omega$, not the lone absorption peak due to state a. This is often refeered to as Autler-Townes splitting and will be further detailed in the following section.

3.2.4 Autler-Townes Splitting

We have described how a two level system interacts with an oscillating electric field in the previous sections. Here we will describe how to observe dressed states and the expected response to strong driving field. In 1955, Stanley Autler and Charles Townes[12] showed that the properties of a strongly driven two level system can be observed by a weak probe between one of the strongly driven levels in the two level system and a third state, assuming the pump and probe frequencies differ significantly. In our exciton system, the absorption from the $X1$ exciton (e1-hh1) will act as a probe of the strongly driven transition between the $X1$ and $X2$ (e1-hh2) excitons ω_{X2-X1}.

With no field applied, we observe the lone absoption peak due to the absorption from the $X1$ exciton. An energy level diagram showing the NIR probe and the expected absorption is shown in Fig. 3.7 a). As we apply a strong resonant

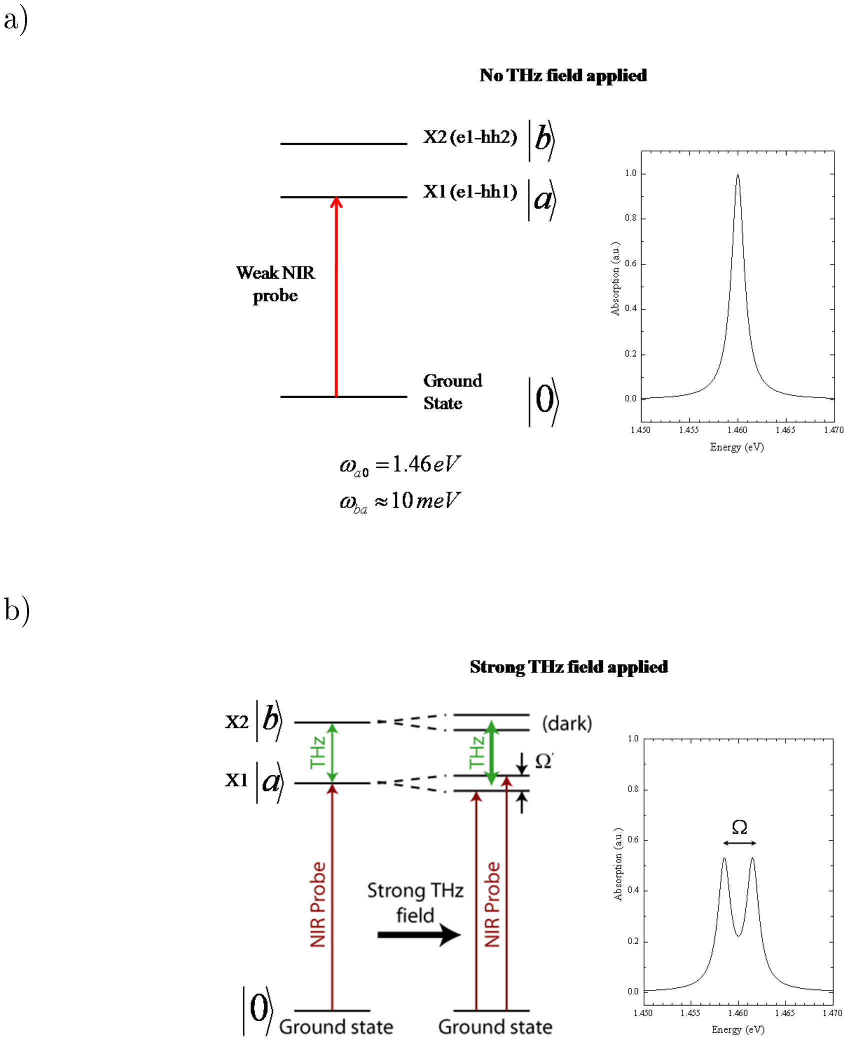

Figure 3.7: Energy level diagram showing the details of Autler-Townes splitting when resonantly driving the system. The absorption in a) is when there is no THz, and a single absorption line is observed. In b), a resonant strong THz field is applied leading to a splitting of the absorption peak. The peaks are of equal amplitdue and the magnitude of the splitting sigiven by the Rabi energy $\hbar\Omega$.

THz field to the system, the single absorption peak splits into two peaks of equal amplitude, shown in Fig. 3.7 b). These two peaks are often referred to as the Autler-Townes doublet and will often be called such in the rest of this manuscript.

If we assume that the THz intensity is the same as in Fig. 3.7b), but we detune the frequency of the strong driving field from the resonance ω_{X2-X1}, we will observe changes to the absorption spectra. There will still be the Autler-Townes doublet, however, the relative amplitudes of the tow peaks will change as the detuning is changed. If the system is driven slightly above resonance, the peak at *lower* energy will have the larger amplitdue of the two peaks, shown if Fig. 3.8a). When the system is driven slightly below resonance, the peak at *higher* energy will have the larger amplitude of the two peaks, shown in Fig. 3.8b).

We see that within the approximations that have been made in the previous sections, changes to the Autler-Townes spectrum can be described by changes of the THz intensity and changes to the detuning of the driving field from resonance. Understanding how changes to the Autler-Townes spectrum are related to the THz intensity and detuning from resonance is essential to understanding our experimental results, and these details will be discussed further in later chapters.

3.2.5 Stark Shifts

So far, we have only discussed the interaction of our system with resonant or nearly resonant light. However, there are other effects associated with strong non-

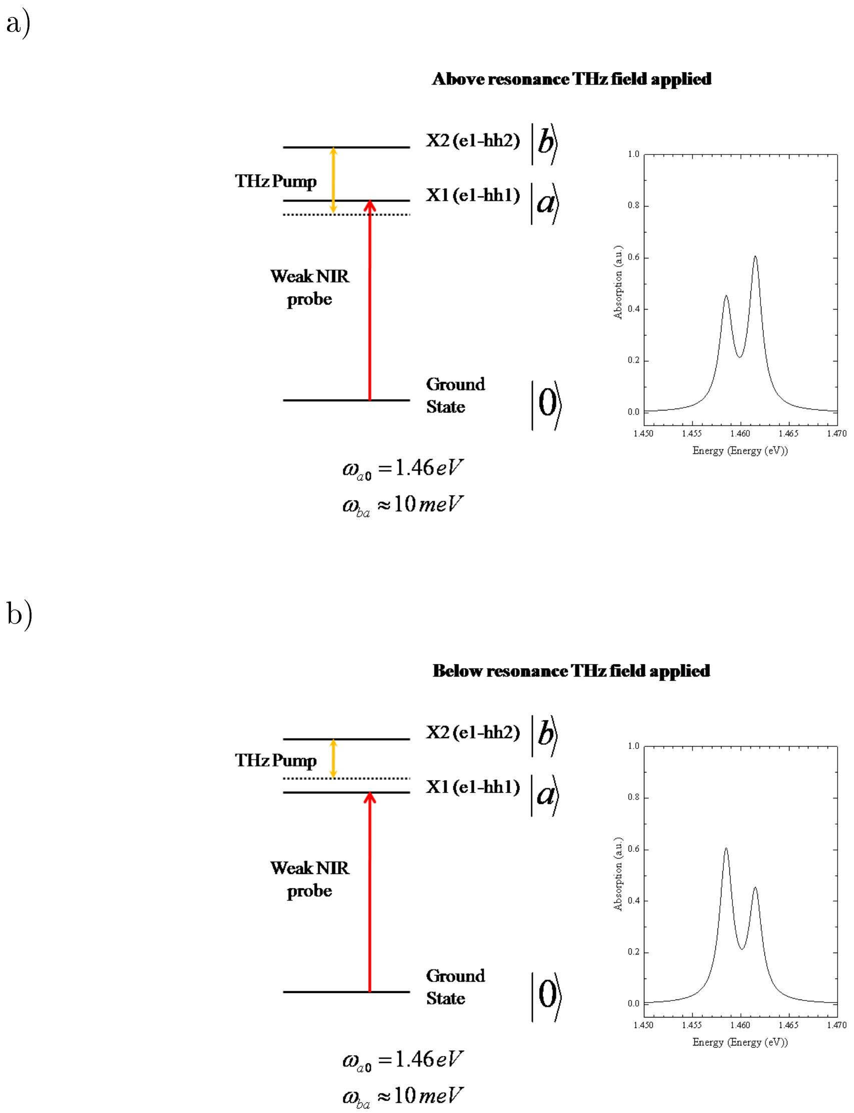

Figure 3.8: Energy level diagrams and examples of the Autler-Townes absorption expected when the THz field frequency is detuned from the exciton resonance ω_{X2-X1}. The driving frequency is above resonance in a) and below resonance in b).

resonant driving fields and DC applied fields. One important effect is the Stark shift of energy levels which occurs when strong non resonant fields are applied to a two level system. A two level system with a transition frequency ω_{ba} driven at a non resonant frequency ω will exhibit a Stark shift

$$\Delta E = \frac{\mu_{ba}^2 E^2}{2} \frac{\omega_0}{\omega_0^2 - \omega^2} \tag{3.25}$$

We see that the direction of the Stark shift is dependent on the detuning of the driving field from the resonant frequency. A driving field at higher frequency than the transition will lead to a decrease of the transition energy while a field a lower frequency will lead to an increase of the transition energy.

When studying DC electric fields applied to quantum wells, we encounter the quantum confined Stark effect (QCSE). Though similar to the Stark effect, strong exciton formation in a quantum well can lead to a significantly increased shift. This is due to the fact that under a strong field, the quantum well is tilted and electrons and holes are pushed to opposite sides of the well. Besides decreasing the overlap of the electron an hole wavefunctions, the electron (hole) is shifted to lower (higher) energies in the conduction (valence) band, creating a red shift of the exciton transition. This is illustrated in Fig. 3.9. The shift of the lowest quantum well level is easily obtained in the infinite quantum well model by treating the electric field as a perturbation to the quantum well energy states. Due to symmetry, the first order perturbation is zero. The Stark shift is

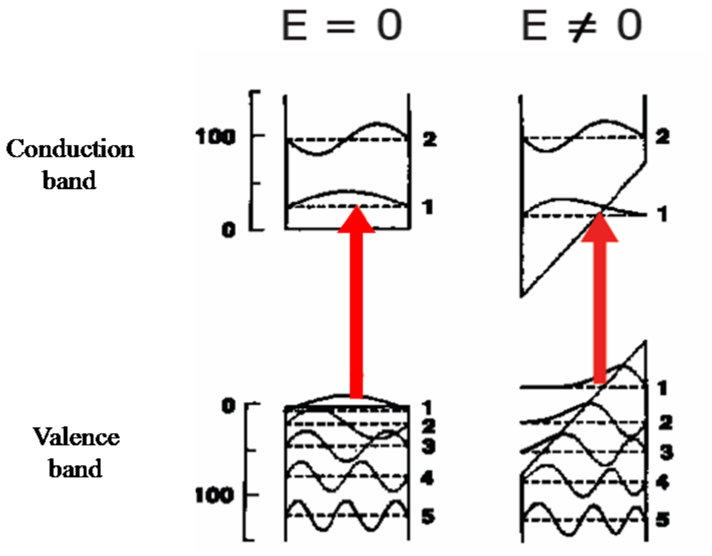

Figure 3.9: An illustration of the quantum confined Stark effect in a semiconductor quantum well. With an intense field applied, the electron and hole are pulled to opposite sides of the well and their energies are educed.

determined by second order perturbation theory and can be explicilty calculated in infinite square well model.

Though the quantum confined Stark shift is explicitly derived for DC electric fields, it is often useful for estimating the shift due to an oscillating field as well. In an AC field, the quantum well will tilt back and forth at the driving frequency, forcing the electrons and holes to spend much of their time near the edge of the well. By inserting the amplitude of the oscillating electric field as the electric field in the equation for the QCSE, we can obtain a rough estimate of the shift caused by the oscillating field.

3.2.6 Bloch-Siegert Shift and Breakdown of the Two Level Model

In the process of our calculations we have made a number of approximations to achieve our results, the two most important being the two level and rotating wave approximation. We have discussed the energy levels of a quantum well system, so we are quite aware that it is not a two level system. The assumption that the radiation only interacts with the two levels we are interested in is unrealistic and this problem can be addressed by introducing more levels into the calcualtions. This is difficult to do and solve analyticically, but nuerical models will account for higher lying levels in the system.

The other approximation made is the rotating wave approximation. In 1940, F. Bloch and A. Siegert[25] showed that by introducing the rapidly oscillating terms we had dropped back into the system as a perturbation, the lowest order effect was a shift of the transition energy. This increase in transition energy is called the Bloch-Siegert shift and we can define an effective transition frequency for our transition

$$\omega^*_{2-1} = \omega_{2-1}(1 + \frac{\Omega^2_{Rabi}}{4\omega^2_{2-1}}) \tag{3.26}$$

As we can see that the magnitude of this shifts quadratically dependent on the Rabi frequency Ω_{Rabi}, the stronger the coupling of the system, the more important this effect will become. If this Bloch-Seigert shift is large , then the rotating wave approximation is no longer valid approximation for the system and must not be used in numerical calculations. Both the Bloch-Siegert shift and effects due to the higher lying levels are present in the experiments performed.

3.3 Autler-Townes Splitting in InGaAs Quantum Wells

Experiments to observe the Autler-Townes effect in a semiconductor quantum well driven by an intense THz field were first performed by Sam Carter[16]. His work clearly showed strong coupling of the intersubband transition in the quantum well, and there were some subtlties of the data that lead us to believe we might observe some very interseting effects if we could achieve a larger ratio of the Rabi frequency Ω compared to the transition frequency ω_{21}. In an effort to achieve the ultrastrong couling limit, where the Rabi frequency is comparable to the transition frequency, we grew wider wells with lower energy transitions. Using lower energy transitions, Rabi frequencies which are a significant fraction of the transition energy are achieved, and extreme non-linear effects are observed. Details of our observations are described in the following sections.

3.3.1 Experimental Observations

In the absence of a THz driving field, the single strong NIR absorption line observed (Fig. 3.10) is identified as the lowest energy exciton $X1$ between an electron from the lowest conduction subband (e1) and a heavy hole from the highest valence subband (hh1). The second lowest energy exciton $X2$, containing a heavy hole from the second highest valence band and an electron from the lowest conduction band, was not observed because the initial and final wavefunctions have the same parity. The third lowest exciton $X3$, consisting of a heavy hole from the third highest valence band and an electron from the lowest conduction band, was not observed because of the small transition matrix element. The absorption at higher energy than the exciton peak arises from the continuum absorption. We see that the absorption due to the continuum is signficantly smaller than the exciton absorption.

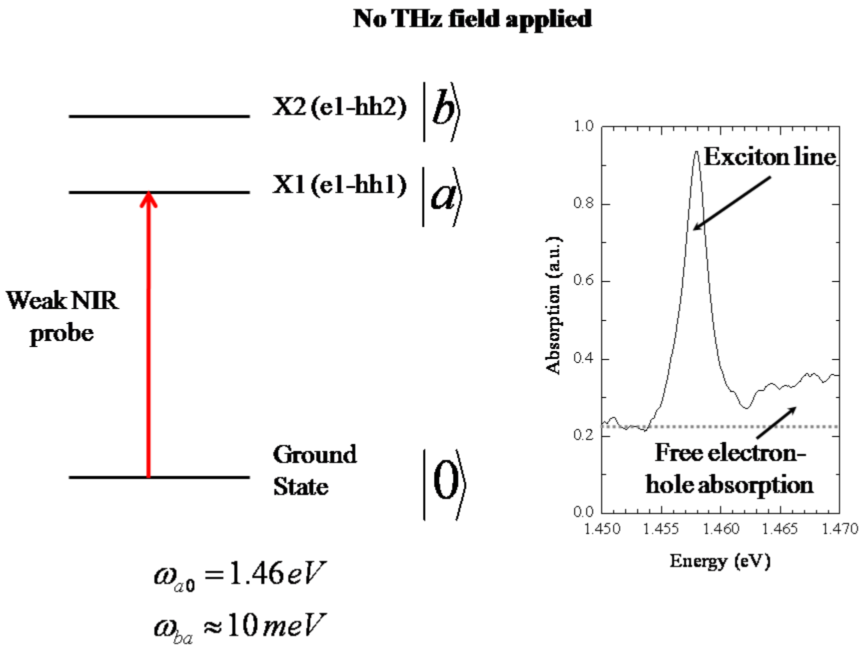

Figure 3.10: Near IR absorption from an 18 nm quantum well. The exciton energy diagram shows the active energy levels. The large peak is due to exciton absorption while the small plateau at higher energies is due to absorption from free electron-hole pairs.

Our experimantal observations showed that the most interesting behavior was observed when the driving frequency ω_{THz} was tuned slightly below the resonant frequency of the exciton transition ω_{X2-X1} (Fig. 3.11). Similar to previous results (ref), we observe the expected Autler-Townes splitting. The Autler-Townes effect is observed as a broadening of the absorption line at low THz intensities and a splitting of the exciton line into two peaks at higher THz intensities. As the THz intensity is further increased, the splitting increases and the peaks become more distinct. However, we can see that there are features of our absorption spectra which are not expected in the two level Autler-Townes picture. Though the splitting of the Autler-Townes doublet incereases as the THz intensity is increased as expected, we observe that the amplitude of these peaks changes with THz intensity as well. When a transition is driven resonantly in the two level model, changes to the driving intensity lead only to changes in the splitting, as it is given by the Rabi frequency $\Omega = \frac{2\mu_{ba}E}{\hbar}$ which has no frequency dependent terms. Changes to the amplitude of the Autler-Townes doublet are caused by shifts in the driving frequency in the two level model. These details are described more thouroghly in section 3.2.4.

For the exciton transition driven slightly below resonance ($\hbar\omega_{THz} = 5.5\, meV$, $\hbar\omega_{X2-X1} = 6.1\, meV$) in a 22 nm quantum well, we observe the spectra for different THz intensities (Fig. 3.11). At low THz intensities (230W), the Autler-Townes splitting can be observed and the peak at *lower* energy is the larger of the two

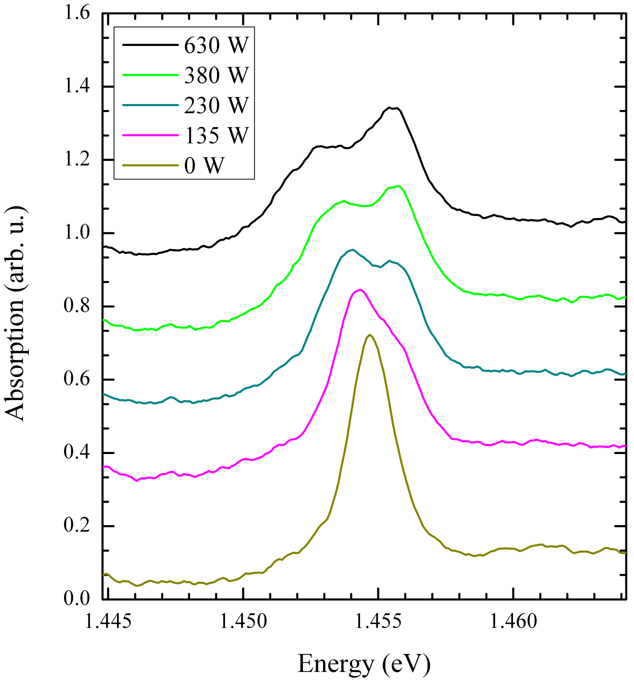

Figure 3.11: Absorption in a 22nm quantum well with a driving frequency $\hbar\omega_{THz} = 5.5\,meV$ at multiple THz powers. The exciton transition ω_{X2-X1} has an energy of 6.1 meV.

peaks. An Autler-Townes doublet where the peak at *lower* energy is larger is indicative of a system being driven *below* resonance. As we believe the field we are applying is slightly lower than the exciton transition, this is an expected result. As the THz intensity is increased, the peak at higher energy grows in amplitude while the amplitude of the peak at lower energy begins to decrease. At THz powers above 380 W, the amplitude of the peaks have changed such that the peak at *higher* energy is the larger of the two Autler-Townes peaks. An Autler-Townes doublet where the peak at *higher* energy is larger is indicative of a system being driven *above* resonance. Because the relative amplitudes of the Autler-Townes peaks indicates the system is being driven *below* resonance at low THz intensities and is being driven *above* resonance at higher THz intensities, without any adjustment of the THz frequency, we believe that the strong THz field induces a red-shift of the effective exciton transition energy $\hbar\omega^*_{X2-X1}$.

Shifts to the Autler-Townes peak intensities are observed at a number of other frequencies as well, shown in Fig. 3.12. The intensity-dependent change of the relative peak amplitudes is interpreted as a red shift of the effective exciton transition frequency ω^*_{X2-X1}. Becuase we appear to be driving the system below resonance at low THz intensities and above resonance at high THz intensities without changing the THz frequency, the exciton transition must be shifting to lower energies to observe this behavior. Experiments at a number of THz frequencies below resonance [Fig. 3.13a)] showed that the further below resonance the THz laser was tuned, a)

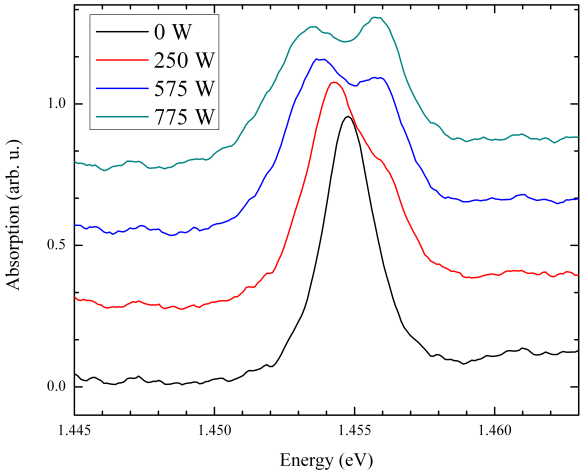

b)

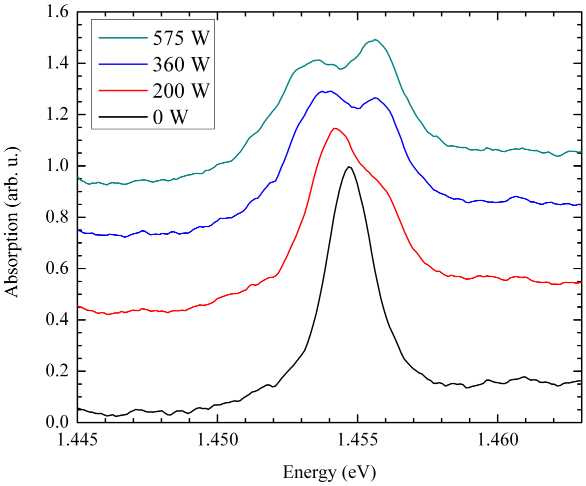

Figure 3.12: Absorption from a 22 nm quantum well at THz photon energies of a) $\hbar\omega_{THz} = 5.3\,meV$ and b) $\hbar\omega_{THz} = 5.4\,meV$. It can bee seen that as the driving frequency is lowered, the THz power necessary to achieve a symmetric splitting increases.

the more intense the THz fields needed to be to create the symmetric splitting associated with resonant tuning. The red shift was calculated as a function of the THz electric field applied by observing symmetric splittings at different detunings from resonance. When the splitting is symmetric, the detuning gives us the red-shift and the electric field can be calculated from the THz power or the magnitude of the splitting. A symmetric splitting of the Autler-Townes peaks was observed at a detuning as large as $\Delta = \omega_{THz} - \omega_{X2-X1} = 0.75\, meV$, corresponding to a shift, $\frac{\omega_{X2-X1} - \omega^{*}_{X2-X1}}{\omega_{X2-X1}}$, greater than 12% [Fig. 3.13b)]. This is further verification that strong THz fields produced a red shift of the exciton transition ω^{*}_{X2-X1}.

We note that the Rabi energies $\hbar\Omega = 2\mu_{ba}E$ achieved in the data shown above approach 3 meV. Considering that the exction transition energy $\hbar\omega_{X2-X1}$ is only around 6 meV, the ratio of these two energies $\frac{\Omega}{\omega_{X2-X1}} \sim 0.5$. This limit where the Rabi energy is a significant fraction of the transition energy is oftern referred to as the ultra-strong coupling regime. In this regime, many of the approximations previously made to describe the system break down and previously negligible interactions lead to interesting new phenomena.

3.3.2 Theoretical Description

Simulations of the quantum well system were performed by Stephen Hughes at Queens University in Canada. These calculations allow us to understand the origin of the red shift of the exciton transition ω^{*}_{X2-X1}. Some details of the theory

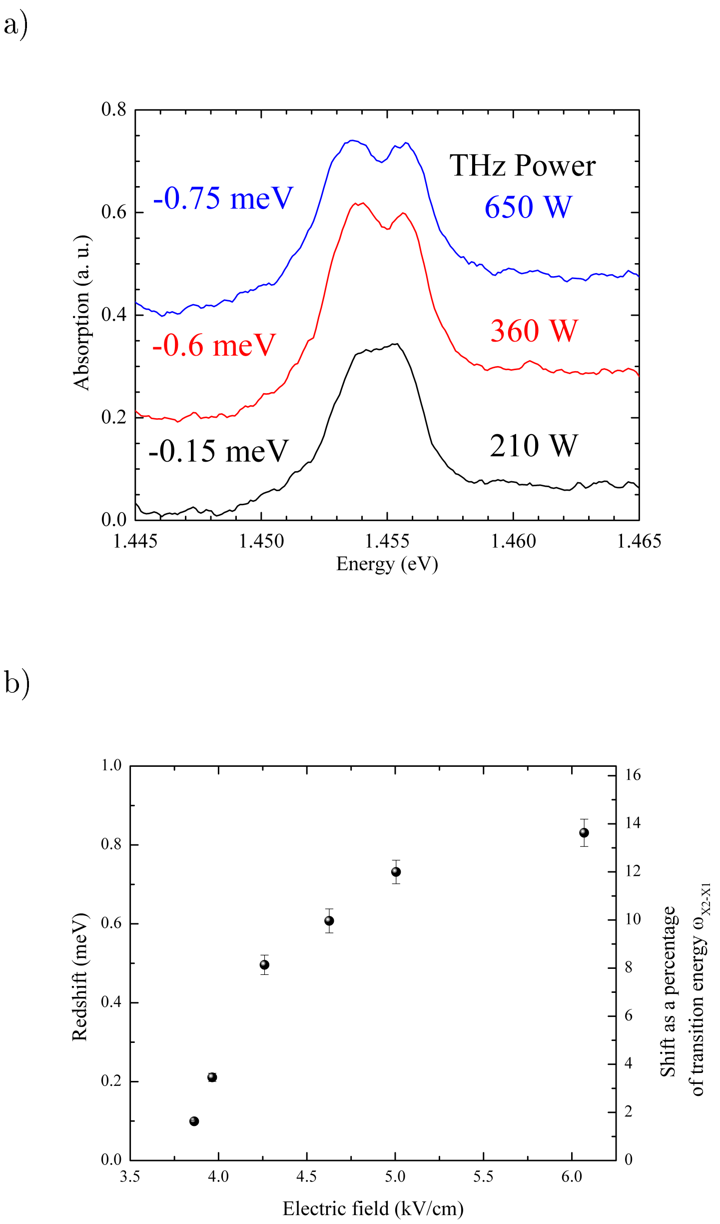

Figure 3.13: a) Absorption spectra from a 22 nm quantum well with the THz field applied at multiple frequencies. The Autler-Townes doublet is nearly symmetrical for all of the absorption curves shown, implying resonant behavior. The larger the negative detuning, the more THz power was necessary to observe a symmetric splitting. b) The red shift was calculated as a function of the THz electric field applied by observing symmetric splittings at different detunings from resonance. The shift relative to the undriven transition $\frac{\omega_{X2-X1}-\omega^*_{X2-X1}}{\omega_{X2-X1}}$ was also plotted.

are provided and the results of the calcualtions are discussed in the following sections.

3.3.2.1 Theory Details

To compute the THz-driven spectra, a numerical solution of the semiconductor Bloch equations was performed in the presence of both a weak optical probe field and a strong THz driving field. The semiconductor Bloch equations are a modificiation of the optical Bloch equations, which are used to understand the dynamics of a quantum system interacting with an electromagnetic field, to include Coulomb, photon and phonon effects. Separate calculations were performed to obtain results on a three band and a four band system. Calculations on both the three and four band systems were performed both with and without application of the RWA to the THz fields. Calculations included a single conduction subband, either two (3 band model) or three valence subbands (4 band model), and the continuum states of a symmetric QW. An efficient numerical solution of the semiconductor Bloch equations was carried out in real space [36]. Using an infinite quantum well model, energy levels were calculated and exciton effects were introduced by a self-consistent determination of the binding energies and Coulomb matrix elements. Calculations neglected band mixing and used the following parameters, which are typical of an InGaAs/AlGaAs system: dielectric constant $\varepsilon = 13$, an electron effective mass $m_e^* = 0.065 m_0$, and a hole effective mass $m_{hh}^* = 0.48 m_0$ for all heavy holes. All simulations used an exciton dephasing rate for the off-diagonal transitions that resulted in a homogeneous broadening rate (FWHM) $\gamma_{hom} = 1.4\,meV$. Simulations shown also include an inhomogeneous broadening $\gamma_{inh} = 0.8\,meV$.

3.3.2.2 Broadening

The true linewidth seen in experiments is caused by both homogeneous and inhomogeneous broadening, so the linewidth alone cannot be used to estimate the exciton dephasing rate, which is the source of only the homogeneous broadening. However, increasing the exciton dephasing rate in the simulations broadens the exciton line and reduces the maximum amplitude of the exciton absorption line while having little effect on the continuum absorption. As the homogenous broadening is increased, the peak is spread out and the relative maximum absorption is decreased relative to the continuum absortion, which is unaffected by changes to the exciton dephasing rate. Therefore, to obtain an estimate of the dephasing rate, the rate is adjusted in the simulations until the relative strengths of the continuum and exciton absorptions fit that of the experimental data with no THz field applied. This led to an exciton dephasing rate for the off-diagonal transitions that resulted in a homogeneous broadening (FWHM) $\gamma_{hom} = 1.4\,meV$. Terahertz induced broadening in the simulations arose directly from the SBE simulations as γ_{hom} was held constant for all values of the Rabi energy. It was found that small changes to the homogeneous broadening have little effect on our predictions.

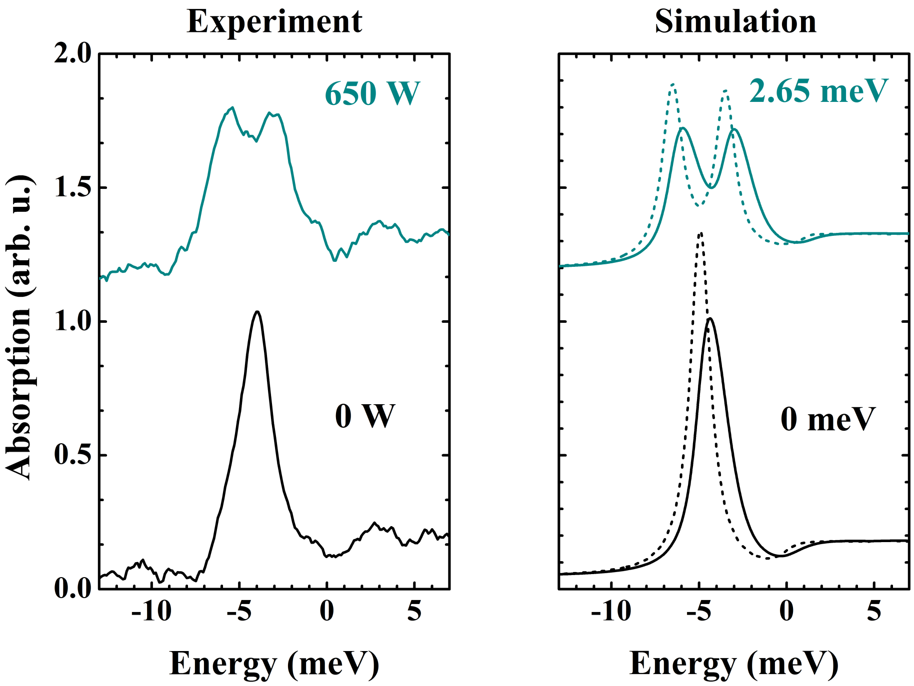

Figure 3.14: Experimental and simulated absorption spectra. The simulated spectra are shown with (solid lines) and without (dashed lines) inhomogeneous broadening $\gamma_{inh} = 0.8\,meV$. Inhomogeneously broadened spectra are more representative of the experimentally observed absorption.

Inhomogeneous broadening was qualitatively included by convolving the SBE solution with a Gaussian function, an effect that produced spectra more representative of the experimental results. Due to the continuum absorption at higher energy than the exciton peak, convolving the simulated spectra with a Gaussian function shifts the exciton peak towards higher energies. Simulations for both the 18 and 22 nm quantum wells are shown with (solid lines) and without (dashed lines) an inhomogeneous broadening $\gamma_{inh} = 0.8\,meV$ (Fig. 3.14).

3.3.2.3 Calculations

We first needed to estimate the energy of the excitonic transitions in the quantum well. Within the semiconductor Bloch equations, a self-consistent determination of the exciton binding energies revealed that $X1$ has a greater binding energy than $X2$. This resulted in the interexciton transition energy ω_{X2-X1} being larger than the bare intersubband transition energy ω_{2-1}. Thus the 22 nm QW, with a calculated hh2-hh1 intersubband transition energy of $\omega_{2-1} = 5.3\,meV$, has an exciton transition energy of $\omega_{X2-X1} = 6.1\,meV$. This significant difference in the energy spectra exemplifies the deviation of the excitonic system from the intersubband system and implies that Coulomb effects are important in observed and calculated spectra.

Simulations including either three or four bands of a 22 nm quantum well with ω_{THz} tuned below ω_{X2-X1} are shown in Fig. 3.15a). Three-subband simulations

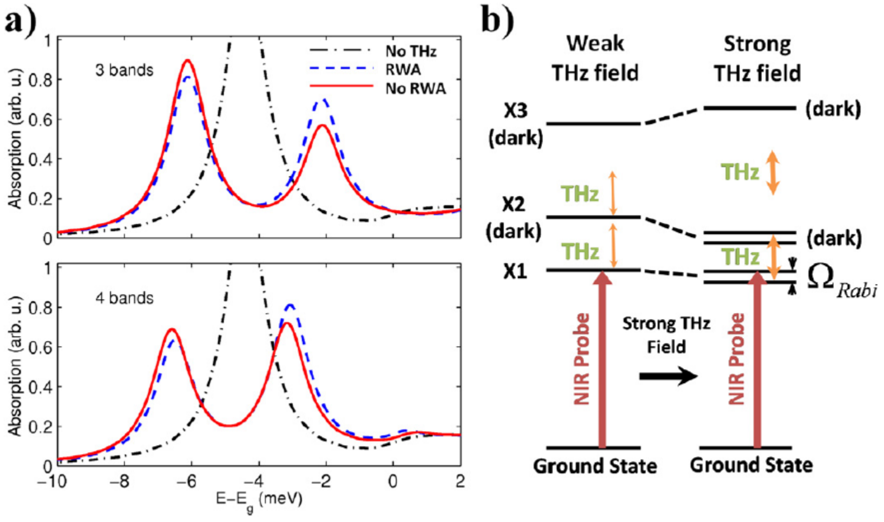

Figure 3.15: a) Simulations of the Autler–Townes splitting of an optically excited 22 nm quantum well with $\omega_{X2-X1} = 6.1\,meV$, $\omega_{THz} = 5.5\,meV$ and $\Omega = 4\,meV$. The black-chain line shows the absorption spectrum with no THz field. The top graph shows simulations calculated with only three subbands (2 valence subbands), while the bottom graph also includes the fourth subband (3 valence subbands). There is evidence of the Bloch–Siegert shift seen in the differences between simulations calculated with (blue dashed) and without (red solid) the RWA. Exciton dephasing rates are set to produce a homogeneous broadening $\gamma_{hom} = 1.4\,meV$. b) An exciton energy level schematic showing the effect of a strong, negatively detuned THz field on the states. In the four-subband model, a strong Stark-like shift to the $X3$–$X2$ transition overcomes the Bloch–Siegert effect and produces an overall red shift of the $X2$–$X1$ transition. Without the fourth subband, the Bloch-Siegert effect shifts the transition to higher frequency, behavior opposite of what is seen in the experiments.

of the Autler–Townes splitting with (blue dashed) and without (red solid) the RWA are shown (Fig. 3.15a), top graph); the chain curve shows the absorption in the zero THz limit. Though both simulations exhibit a negative detuning, the difference between the heights of the two peaks is larger in the non-RWA spectrum, indicating that it is further from resonance than the RWA spectrum. This difference between the effective detuning $\omega_{THz} - \omega^*_{X2-X1}$ of the two spectra is evidence of a Bloch–Siegert effect that blue shifts ω^*_{X2-X1} in the non-RWA model. By itself, this is an interesting result: the Bloch–Siegert effect, calculated for a simple three-state system, persists in the three-subband SBE model with Coulomb interactions. However, the persisting negative detuning of the system at this intense value of the Rabi energy, even without the RWA, shows the absence of a red shift and demonstrates that the three-subband model is not consistent with our experimental findings.

To address the inconsistencies between simulation and experiment, the third valence subband (hh3) was introduced which allowed coupling between excitons $X2$ and $X3$. As calculated in the infinite well approximation, the hh3 subband was separated from the hh2 subband in energy by 9.5 meV ($\frac{9}{5}\hbar\omega_{2-1}$), more than 4 meV off resonance from the driving frequency. As is seen in the three subband model, simulations (Fig. 3.15a), bottom graph) indicate a Bloch–Siegert shift of the non-RWA spectra. With an intense THz field applied at a frequency that is below that of the exciton transition ω_{X2-X1}, the relative amplitudes of the

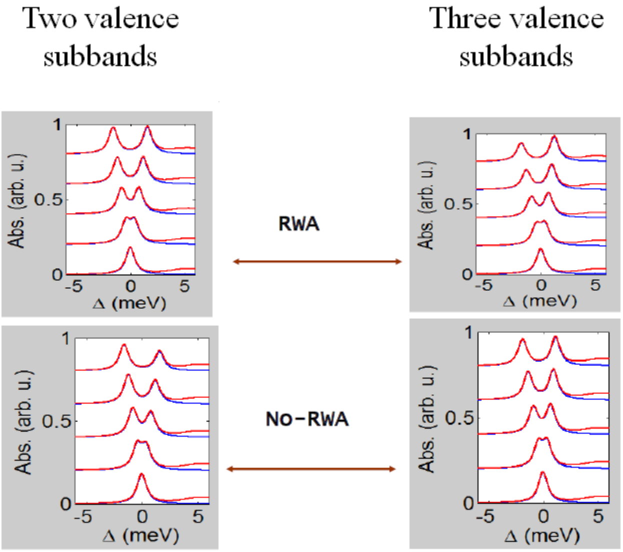

Figure 3.16: Simulations of the quantum well exciton system calculated with three and four subbands with and without the RWA for the THz fields. The red line includes the continuum states and absorption of free electron-hole pairs can be seen at higher energies.

two Autler–Townes peaks indicate that the system is being driven above resonance. The simulated behavior in the four subband model is consistent with our experimental observations by indicating that the strong THz field induces a red-shift of the effective transition energy ω^*_{X2-X1}. This red shift is interpreted as a Stark-like shift to the off-resonant $X3-X2$ transition that overcame the expected Bloch–Siegert effect, illustrated by an energy level schematic in Fig. 3.15b).

A detailed diagram showing the differences between the two models with and without the RWA is shown in Fig. 3.16. THese simulations clearly show that though the Bloch-Siegert shift is important at the THz intensities we are applying, it is not solely responsible for the shifts seen in the experiments. Only by including non-RWA effects and a fourth subband in the SBE model were we able to predict a red shift of ω^*_{X2-X1} which is in good qualitative agreement with the experimental data.

3.3.3 Comparison to Experiment

Now that we have established the model for simulating our system,we can begin to make quantitative comparisons to the experimental data. In order to simulate our system, we need to be able to estimate the electric field in the sample. This not trivial and is done in two separate ways.

3.3.3.1 Estimating the Electric Field in the Sample

It is very difficult to get an accurate estimate of the electric field at the sample using the power in the THz beam due to the complicated geometry where the beam strikes the sample facet. However, assuming the dipole moment is constant, as is done in the simulations, the Rabi energy is directly proportional to the electric field. Additionally, the magnitude of the splitting, when the driving beam is resonant, is given by the Rabi energy. Because we have the ability to measure the splitting quite accurately by fitting two Lorentzian peaks to the experimental data, we can obtain an accurate measure of the electric field from the splitting.

From the Lorentzian fits, we measure the maximum Rabi splitting in the 18 nm quantum well to be 2.7 meV. Using this Rabi energy and the dipole moment calculated from the infinite well model, we estimate the electric field at the quantum well to be $4.1\,{}^{kV}\!/_{cm}$. Calculations of the electric field based on the power and the diameter of the focused THz beam estimate the field strength to be between 4 and $5\,{}^{kV}\!/_{cm}$, a figure that is in good agreement with the value estimated from the Rabi splitting. For calculations of the electric field in the sample the values used are given as follows: the power in the sample $P_{in} \approx 0.6 * Power\,measured\;(\,3\,kW)$, beam diameter $d \approx 800\mu m$, index of refraction n = 3.3, spot area $A = \frac{\pi d^2}{4}$, and field strength $F = \sqrt{\frac{2P_{in}}{A\epsilon_0 cn}}$. This implies that it is reasonable to use the Rabi splitting to estimate the Rabi energy and to use these values in the simulations when calculating the corresponding spectra.

3.3.3.2 Results in an 18 nm Quantum Well

Experimental results from and simulations of an 18 nm wide quantum well driven slightly below resonance is shown in Fig. 3.17. When the 18 nm QW was driven with the THz frequency negatively detuned 0.4 meV below $\omega_{X2-X1} = 10\,meV$, a symmetric splitting was achieved at 650W. A Rabi energy $\hbar\Omega = 2.7 \pm 0.1\,meV$ was estimated by a fit of two Lorentzians to the absorption spectrum. The calculations of the 18 nm quantum well with a symmetric splitting of $\hbar\Omega = 2.65\,meV$, a value within the experimental error of the experimentally observed value, show strong agreement with the experiment. For simulations at lower powers, the Rabi energy used in the simulations was scaled to the square root of the experimentally measured power levels. The resulting absorption curves reproduce the behavior observed in experiment quite well.

Simulations of the 18 nm quantum well were performed at a number of separate THz frequencies and intensities as well. Experimental results and simulations for the 18 nm quantum well driven 1.8 meV below resonance and 0.4 meV above resonance are shown in Fig. 3.18. The very good agreement between the simulations and experimental data is a strong indication that the system is being appropriately modeled.

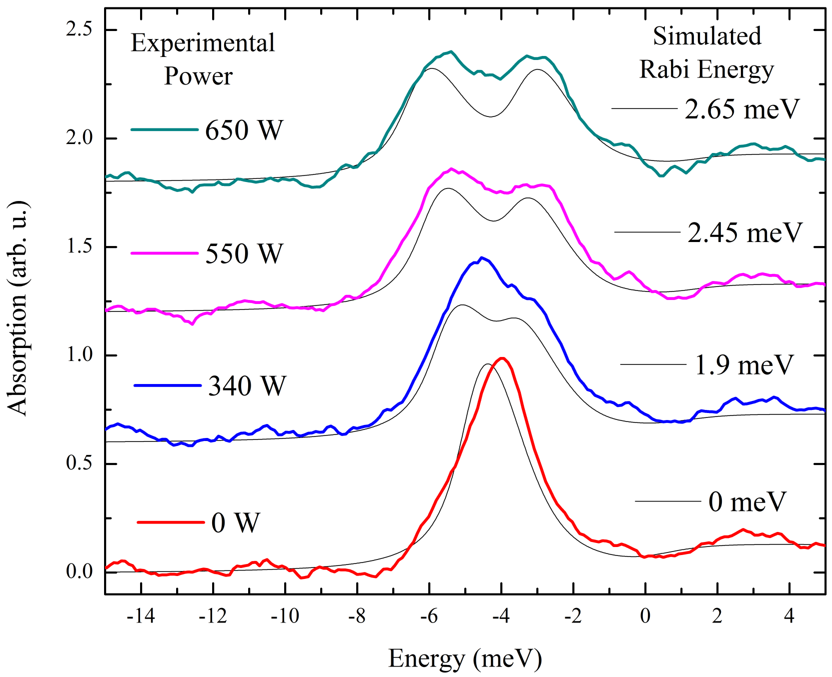

Figure 3.17: Experimental and calculated interband absorption spectra from an 18 nm quantum well at multiple THz powers. The system was driven 0.4 meV below the 10 meV excitonic transition ω_{X2-X1}. The experimental curves are labeled by the applied THz power and the simulations are labeled by the Rabi energy.

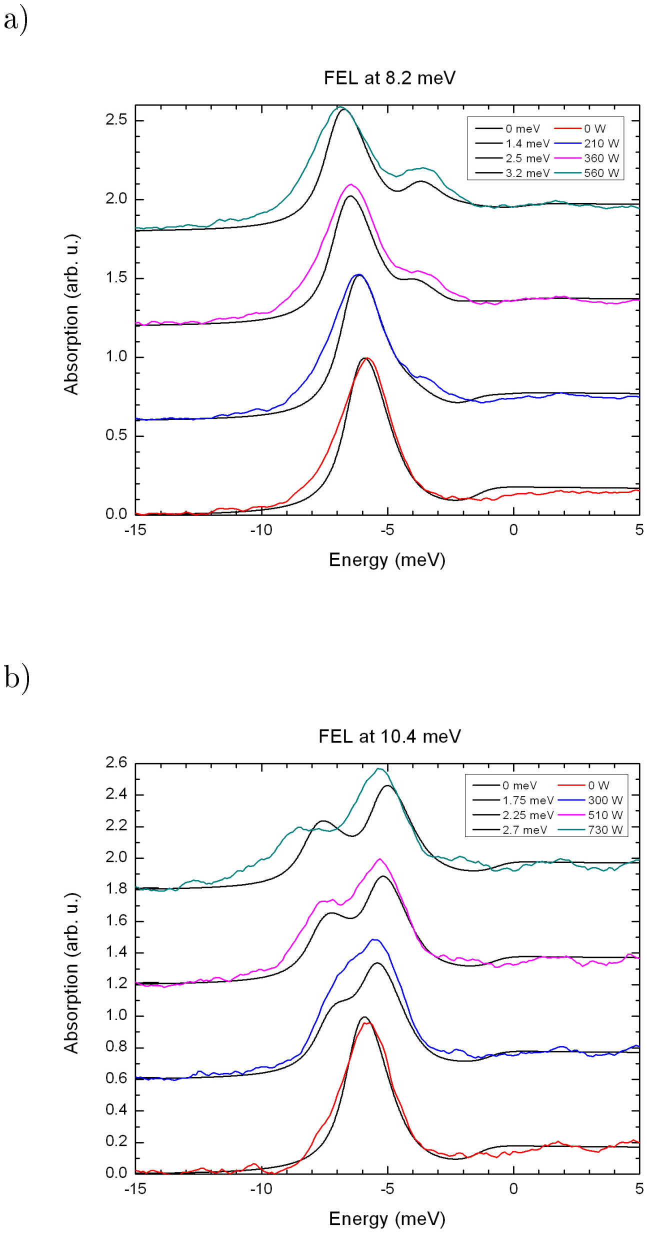

Figure 3.18: Experimental and calculated interband absorption spectra from an 18 nm quantum well at multiple THz frequencies and powers. The experimental curves are labeled by the applied THz power and the simulations are labeled by the Rabi energy. a) Results when the system was driven 1.8 meV below the 10 meV excitonic transition ω_{X2-X1}. b) Results when the system was driven 0.4 meV above the 10 meV excitonic transition ω_{X2-X1}.

3.3.3.3 Results in a 22 nm Quantum Well

Calculations of the 22 nm QWs driven 0.6 meV below the excitonic transition $\omega_{X2-X1} = 6.1\,meV$ clearly show the reversal of relative peak intensities with increasing Rabi energy that is observed in the experiments (Fig. 3.19, black solid lines). The splitting at 630 W was fit to two Lorentzians and found to be $3\,meV$, so the splitting in the simulation of 3.6 meV implies a more intense field than is present in the experiment, however, it still demonstrates the behavior observed in experiments (Fig. 3.19, colored lines). The amplitude of the higher energy peak is larger in the experimental data than in the simulations, so the calculated redshift of ω^{*}_{X2-X1} was not as large as was observed experimentally. However, the reversal of peak intensities, evidence of a redshift of the resonance, is still clearly replicated at high fields. Further simulations expanding our model to four valence subbands were performed, but these had qualitatively similar results to the three subband model. The overall success of our final model shows that the THz-driven quantum well system is modified by competing effects and a proper description must include a conduction subband and at least three valence subbands and must not invoke the RWA.

3.3.3.4 Note about heating

Heating has been thoroughly investigated in this and previous experiments and is not responsible for the behavior observed in this experiment. Our observations

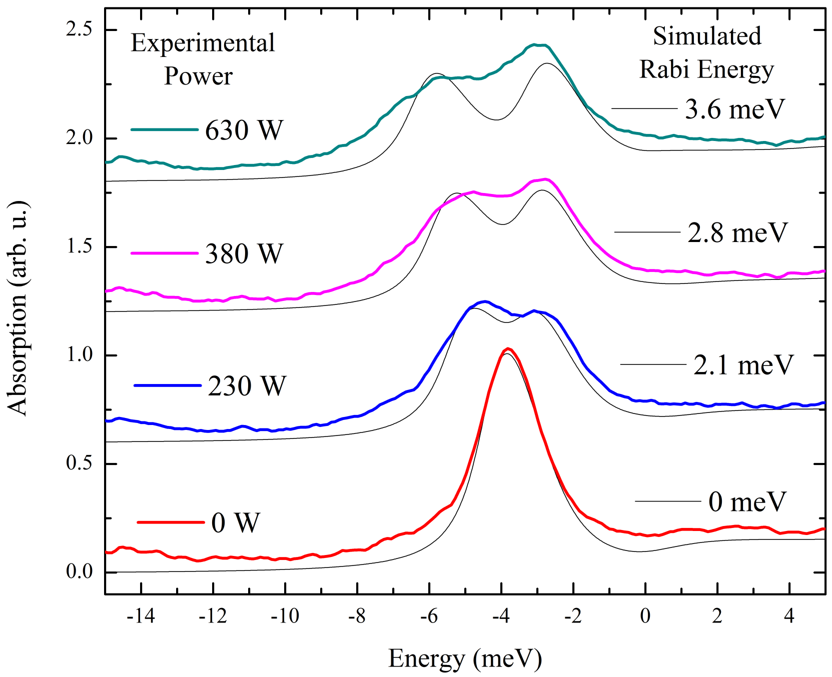

Figure 3.19: Experimental and calculated interband absorption spectra from an 22 nm quantum well at multiple THz powers. The system was driven 0.6 meV below the 6.1 meV excitonic transition ω_{X2-X1}. The experimental curves are labeled by the applied THz power and the simulations are labeled by the Rabi energy.

cannot be the result of either lattice or carrier heating. Though interband transitions are dependent on the energy of the band gap and therefore highly susceptible to temperature changes, intersubband levels in the quantum well are determined by the width of the well and the effective mass of the particle, neither of which are strongly temperature dependent[29]. Hence, any change in the temperature of the system should first be observed as a shift of the exciton absorption line. This is shown in temperature dependent measurements of the Autler–Townes effect performed by Sam Carter[30] (figure 3.19, p. 80), where the Autler–Townes peaks at 40K have the same relative amplitudes as the peaks at 10 K, but the main exciton line has been shifted by 2 meV. In the experiments presented we observe no discernable shift of the exciton, only a large red-shift of the excitonic intersubband energy. We measure absorption with a very weak light-emitting diode ($I_{NIR} < 0.5\,{}^{W}\!/_{cm^2}$) and are therefore insensitive to heating of the extremely small carrier population. The negligible effects of heating are also consistent with previous experiments performed by Černe et al[31] and Carter et al[16].

3.4 Conclusions

We have studied two QW samples in the limit of ultra-strong coupling. In the wide 22 nm quantum wells investigated, the Rabi energy approached half of the energy of the strongly driven transition ω_{X2-X1}. Though a blue-shift of the transition is expected due to non-RWA effects, what is observed is a red-shift that exceeds 12% of the transition energy. Theoretical investigations reveal the interplay between the Bloch–Siegert shift and the ac Stark effect and indicate that the Stark shift is the dominant effect in these samples. We imagine that this interplay could be further investigated with semiconductor quantum wells grown in different geometries. When the energy of the second lowest transition $E32 \gtrsim E21$, as is the case in square quantum wells like those investigated, the ac Stark shift is expected to be dominant. If the energy $E32 \gg E21$, as is the case for tunnel-coupled double quantum wells, we expect that the Stark shift would be negligible and only the Bloch–Siegert shift would be observed. Similarly, if $E32 < E21$, as in triangle quantum wells, the ac Stark shift is a blue shift and the Stark effect is in the same direction as the Bloch–Siegert effect. Our results, coupled with the adaptability of the THz-driven quantum well system, imply that this is an ideal system to investigate ultrastrong coupling on a quantitative level and to controllably explore the regime outside the three-level model and beyond the rotating wave approximation.

Chapter 4

Electron-Hole Recollisions

In the previous chapters, we have discussed a number of non-linear phenomena related to the mixing of intense THz radiation with NIR light in semiconductors. To describe these phenomena, we have relied on a solid understanding of condensed matter and semeconductor physics, as one would expect. In our descriptions of the semiconductor system, some analogies to atomic physics systems have been made, such as the exciton having many similarities to the hydrogen atom, but phenomena similar to that seen in atomic systems have not been discussed. There are many experiments currently working to utilize the similarities between atomic and condensed matter systems, such as atom-trapping experiments. Atom trapping experiments often hope to observe condensed matter phenomena in a much more dilute system, simplifying the analysis and allowing for the observation of very low numbers of particles.

We present here our observation of high-order sideband generation as a result of electron-hole recollisions in semiconductors. This is a remarkable extension of the recollision theory of high-order harmonic generation seen in atomic and molecular gases. Our observations not only show the power and utility of the quasiparticle model of excitons, but they may also allow for an enhanced understanding of the recollision phenomenon and basic material properties related to excitons. Additionally, our observation of recollisions in both a bulk semiconductor and a semiconductor heterostructure implies that this phenomenon is a universal effect of optical excitations in semiconductors and that high-order sideband generation might be a unique tool for probing these excitations.

4.1 Excitonic Sideband Generation

When intense THz radiation is applied to a semiconductor, the strong ac fields can drastically alter its optical properties near the band gap. Electro-optic effects such as the dynamical Franz-Keldysh[32,33,34] and Autler-Townes[16,18,35] effects have been studied in detail at the UCSB FEL, and details of the Autler-Townes effect have been described in the chapter 3. We have also discussed the basics of sideband generation in chapter 2. A number of experiments investigating sideband generation in excitons have been performed at the FEL and other high THz field facilities around the world[36,37,38]. For the observation of phenomena such as sideband generation and the Autler-Townes effect, the use of semiconductor quantum wells is often necessary due to their strong formation of excitons.

Sideband generation is useful for understanding the strong interaction between light and matter, particularly how this interaction results in non-linear optical phenomenon. It has been proven to be useful as a probe of the energy levels of excitons in semiconductor quantum wells. Additionaly, sideband generation has been of interest for modulating NIR or optical beams at high speeds.

Observation of excitonic sideband generation at the FEL has been achieved in a number of systems. John Černe, et. al[36], and Junichiro Kono, et. al[37], both performed sideband experiments on magnetoexcitons in quantum wells, where a magnetic field was applied to achieve Landau levels that are resonant with the excitonic transitions. When the Landau levels were resonantly tuned to intra-excitonic transitions, strong sideband generation was observed and sidebands of up to fourth order are observed.

More recent work performed at the Dresden FEL have shown that excitonic sideband generation can be observed withouth the application of a strong magnetic field. They were also able to show sideband generation at room temperature.

In both the experiments performed at Dresden and UCSB, the sideband generation appeared to be perturbative in nature and the sideband intensity decreased exponentially with increasing sideband order. None of the experiments performed were able to observe sidebands higher than fourth order. The observation of high-order sidebands presents an interesting question as to the nature of the phenomenon. We will describe our observations and theoretical description of the origin of the phenomenon in the following sections.

4.1.1 High-Order Sideband Generation

When an intense THz field was applied to optically excited excitons in a quantum well, up to nine sidebands were observed at higher frequency than the NIR frequency creating the excitons. The frequency of THz field applied was well below the lowest intersubband transition and the $1s-2p$ exciton transition. A large number of sidebands were seen at a few different FEL frequencies. We can see from the sideband spectra shown in Fig. 4.6 that the intensity of the sidebands does not decrease quickly with increasing order. This behavior is not described by the perturbative model of the exciton system in an intense electric field. In order to understand our observations, we turn to a phenomenon that has been studied in atomic systems for decades, high-order harmonic generation. We will show in the following sections that the recollision model that describes high-order harmonic generation can be modified to describe high-order sideband generation as well.

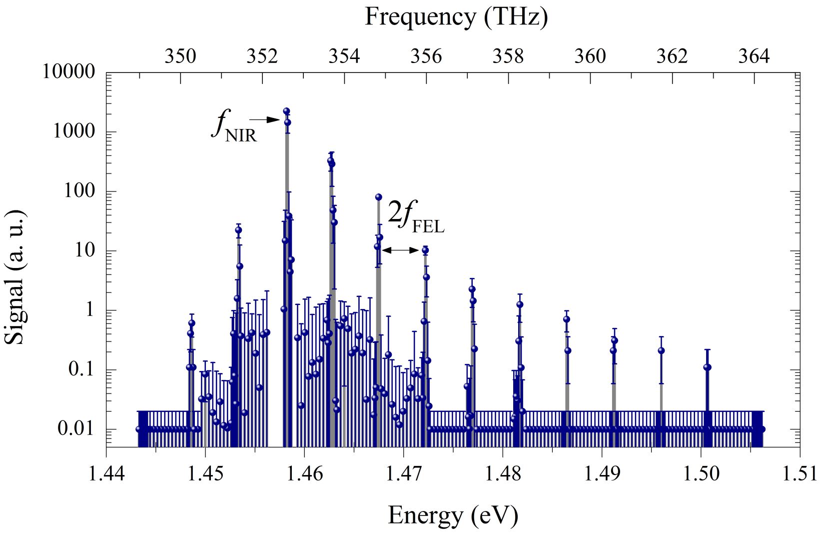

Figure 4.1: Sideband spectra from a 15 nm quantum well

4.2 High Harmonic Generation and the Recollision Model

4.2.1 High-Order Harmonic Generation

When an extremely intense optical or NIR laser is focused onto a gas of atoms of molecules an electron can be ripped from an atomic core, accelerated in the field and then forced to recollide with the core it originated from, releasing the energy gained as harmonics of the laser frequency. With the application of fields of intensity $\sim 10^{15}\, {}^{W}\!/_{cm^2}$, harmonics of over one hundredth order can be created, producing light deep into the x-ray spectrum. For this reason, high harmonic generation is now often used as a tabletop source of x-ray light in many laboratories. Additionally, it has been a powerful tool for studying the orbitals the electron originates from in molecules, and tomography of the highest occupied molecular orbital of a number of molecules has been performed. This has lead to a growth in the exploration of attosecond science resulting in powerful new technologies and growth in our understanding of molecular structure. The phenomenon of high harmonic generation has many similarities to high sideband generation and we hope that high sideband generation might present some interesting new science and technology.

4.2.2 The Three Step Recollision Model

The recollision process between an electron and an atomic core can be described by a three-step model[39]: first the electric field associated with an intense laser ($\sim 10^{13}\, {}^{W}\!/_{cm^2}$ at a wavelength $\lambda = 1\mu m$) ionizes an electron via tunneling[40], then the ionized electron is quickly accelerated like a free particle away from and back to the atomic core by the optical field, and finally, on returning to the core, the electron recollides with the atomic core and emits radiation in the form of high harmonics of the laser frequency. Because tunneling predominantly occurs when the electric field intensity is at its maximum[41], photons are emitted every half-period. The highest-order harmonic is determined by the maximum energy the electron can gain in the oscillating electric field, the ponderomotive energy $U_p = \frac{e^2E^2}{16\pi^2 m_e f^2}$, where e is the charge of the electron, m_e is the mass of the electron, E is the electric field amplitude and f is the frequency of the field.

The ponderomotive energy can be calculated by solving the equations of motion for a free electron in an oscillating electric field. The ponderomotive energy U_p is just the average kinetic energy of an electron in an oscillating field $\left\langle \frac{1}{2} m_e v^2 \right\rangle$. Assuming $E(t) = E\cos(2\pi ft + \varphi)$ then

$$F = m_e a(t) = eE\cos(2\pi ft + \varphi) \tag{4.1}$$

By solving for the acceleration $a(t)$ and integrating to get the electron velocity $v(t)$ we find

$$a(t) = \frac{eE}{m_e}\cos(2\pi ft + \varphi) \tag{4.2}$$

$$v(t) = \int_0^{t'} a dt = \int_0^{t'} \frac{eE}{m_e}\cos(2\pi ft + \varphi)dt \tag{4.3}$$

$$v = \frac{eE}{2\pi f m_e}\sin(2\pi ft' + \varphi) + C \tag{4.4}$$

For the following calculation, we will assume that the electron entered at the peak of the electric field with zero velocity v, meaning $C = 0$. We can then find the ponderomotive energy of the electron U_p

$$v^2 = \frac{e^2E^2}{4\pi^2 m_e^2 f^2}\sin^2(2\pi ft' + \varphi) \tag{4.5}$$

$$\begin{aligned} U_p &= \left\langle \frac{1}{2} m_e v^2 \right\rangle = \frac{1}{2}\left\langle \frac{e^2E^2}{4\pi^2 m_e f^2}\sin^2(2\pi ft' + \varphi) \right\rangle \\ &= \frac{e^2E^2}{8\pi^2 m_e f^2}\left\langle \sin^2(2\pi ft' + \varphi) \right\rangle = \frac{e^2E^2}{16\pi^2 m_e f^2} \end{aligned} \tag{4.6}$$

The maximum energy gained by the electron in the recollision process is $E_{max} = 3.17U_p + I_p$, where I_p is the ionization potential of the atom or molecule. When the electron is in the atomic or molecular core, it is lower than the free electron energy by a magnitude I_p. When the electron tunnels out and is free to move in the field, it has gained this amount of energy. Therefore the total energy the electron can gain is the maximum kinetic energy plus the potential energy of ionization. The value $3.17U_p$ is found to be the maximum kinetic energy gained by an electron in an oscillating electric field, producing the value $E_{max} = 3.17U_p + I_p$.

The three step model has been extremely successful at explaining phenomena related to recollisions for decades. In the sections to follow, we will apply the three step recollision model to excitons in semiconductors. We find that the recollision model provides good qualitative agreement with our observations, and we believe that recollisions between electrons and holes are responsible for the high-order sidebands observed.

4.2.2.1 Maximum Kinetic Energy in an Oscillating Field

If we assume that the velocity of an electron that entered an oscillating electric field at time $t' = 0$ and at a phase φ is zero, we find

$$v = 0 = \frac{eE}{2\pi f m_e}\sin(2\pi f 0 + \varphi) + C \tag{4.7}$$

$$C = \frac{-eE}{2\pi f m_e}\sin(\varphi) \tag{4.8}$$

$$v(t') = \frac{eE}{2\pi f m_e}[\sin(2\pi f t' + \varphi) - \sin(\varphi)] \tag{4.9}$$

By integrating the velocity $v(t)$, we calculate the position of the electron $x(t)$

$$x(t) = \int_0^t v dt' = \int_0^t \frac{eE}{2\pi f m_e}[\sin(2\pi f t' + \varphi) - \sin(\varphi)]$$

$$= \frac{-eE}{4\pi^2 m_e f^2}[\cos(2\pi f t + \varphi) + \sin(\varphi)t] + C \tag{4.10}$$

Assuming the position x at $t = 0$ is zero, we find the position

$$x(0) = 0 = \frac{-eE}{4\pi^2 m_e f^2}\cos(\varphi) + C \tag{4.11}$$

$$C = \frac{eE}{4\pi^2 m_e f^2}\cos(\varphi) \tag{4.12}$$

$$x(t) = \frac{-eE}{4\pi^2 m_e f^2}[\cos(2\pi f t + \varphi) + \sin(\varphi)t - \cos(\varphi)] \tag{4.13}$$

Given the position $x(t)$, we can find for the times t_f when the electron recrosses the origin by solving the equation $x(t_f) = 0$. This is not trivial as many values of φ exist where $x(t_f) \neq 0$. Once we have solved for the times t_f, we can find the kinetic energy $\frac{1}{2}m_e[v(t_f)]^2$ by using eq. 4.9. Solving for the maximum of the kinetic energy, we find it is equal to $3.17U_p$.

4.2.3 Extension to High-Order Sideband Generation

We believe that the recollision model can be extended to describe the interaction between electrons and holes when an intense THz field is applied to an exciton system. Theoretical calculations of the high-order sideband generation phenomena have been performed by Ren Bao Liu and his postdoc Jie-Yun Yan[42,43]. These calculations indicate that the electron can tunnel out of the exciton, be accelerated by the field, and recollide with the hole it was originally bound to. In this model, a weak NIR laser resonantly creates excitons in a semiconductor [Fig. 4.2a)] while an intense THz field is applied. The intense THz field causes the electron to "tunnel" out of the exciton, leaving to be freely accelerated by the field. Once it is free in the field, it is quickly accelerated away from and back to the hole it left behind originally [Fig. 4.2b)]. When it recollides with the hole it left behind, it can release the energy gained as well as the energy of recombination in the form of sidebands. Due to the inversion symmetry of the system, identical recollisions occur every half-period and sidebands of the NIR laser are observed only at even multiples of the FEL terahertz frequency: $f_{THz} = f_{NIR} + 2nf_{THz}$, where $2n$ is the order of the sideband. A large number of sidebands are expected to be observed and the intensity of the sideband is expected to decrease slowly with increasing order (Fig. 4.3). This phenomenon is similar to the plateau of harmonics seen in high-order harmonic generation and the maximum energy gained by the electron in the field is expected to be $E_{max} = 3.17U_p + E_b$. In this equation, E_b is the exciton binding energy and $U_p = \frac{e^2E^2}{16\pi^2 m_e^* f_{THz}^2}$, with the electron effective mass m_e^* replacing the electron mass m_e and where E is the amplitude of the THz field.

The "tunnelling" process in the recollision model is actually an approximation that can be made for multiphoton ionization[40]. In order for this approximation to be valid, the ionization potential I_p, or in the case of excitons, the binding energy E_b, must be significantly greater than the THz photon energy $\hbar\omega_{THz}$ to prevent single or two photon ionization. This limited us to frequencies with a photon energy of around 2-3 meV due to the 5-10 meV binding energy in GaAs and GaAs

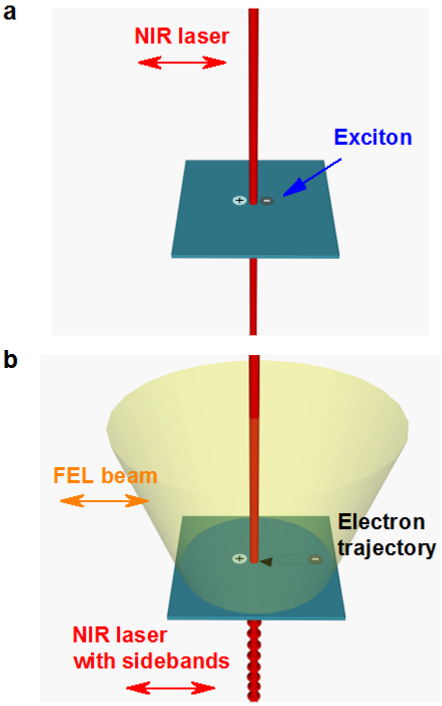

Figure 4.2: Illustration of the process of sideband generation. a) A NIR laser creates excitons in a semiconductor. b) An intense THz laser causes the electron to tunnel out, be accelerated in the field and recollide with the hole it left behind.

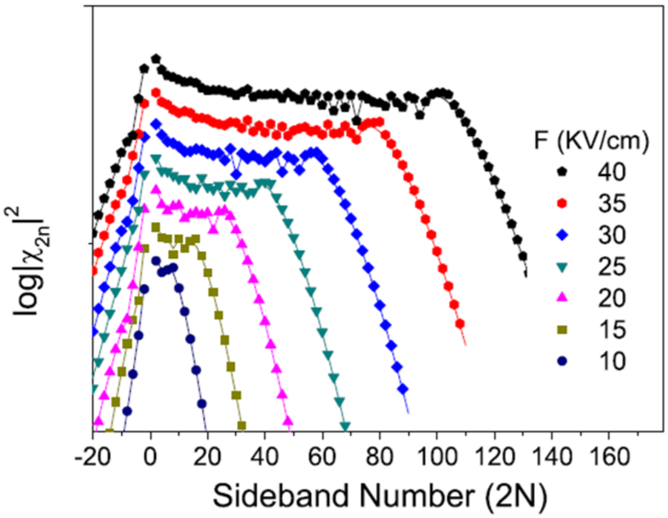

Figure 4.3: Calculations of the sideband intensity as a function of applied THz field strength. The offset is just for clarity. The exciton binding energy E_b used was 8 meV and the photon energy was 5 meV[43].

heterostructures. By causing recollisions between optically excited electron–hole pairs, which, in gallium arsenide, have small effective masses ($\sim {}^{m_e}/_{15}$) and binding energies of 5-10 meV, it is predicted that high-order sideband generation can be achieved at much lower intensities ($\sim 10^5\, {}^{W}/_{cm^2}$) than are required for high harmonic generation.

4.3 Observation of High-Order Sideband Generation in a Quantum Well

The high sideband experiment was first performed on the quantum well system due to the increased Coulomb interaction from confinement. The increased confinement increases the binding energy of the exciton and should increase the magnitude of the dipole moment, enhancing the sideband generation. Though calculations on quantum wells were not performed, it was hypothesized that the confinement and increased Coulomb force in the well will lead to an enhancement of the sideband signal.

4.3.1 Experimental Setup

Excitons in $\mathrm{In}_{0.06}\mathrm{Ga}_{0.94}\mathrm{As}/\mathrm{Al}_{0.3}\mathrm{Ga}_{0.7}\mathrm{As}$ quantum wells are created by NIR radiation (∼350 THz) from the continuous-wave titanium–sapphire laser. The quantum well sample used for most of the measurements taken was the 15 nm well grown for Sam Carter for his Autler-Townes experiment[16], however, some data was taken on the 15 and 18 nm quantum well samples described in section 3.1.1.2. The wells consist of 10 repetitions of 15/18/22 nm $\mathrm{In}_{0.06}\mathrm{Ga}_{0.94}\mathrm{As}$ quantum wells between 30 nm $\mathrm{Al}_{0.3}\mathrm{Ga}_{0.7}\mathrm{As}$ barriers. The excitons are subjected to high-intensity radiation from FELs at frequencies between 0.4 and 1.6 THz. The beam from the FEL is focused onto the top of the quantum well sample such that the

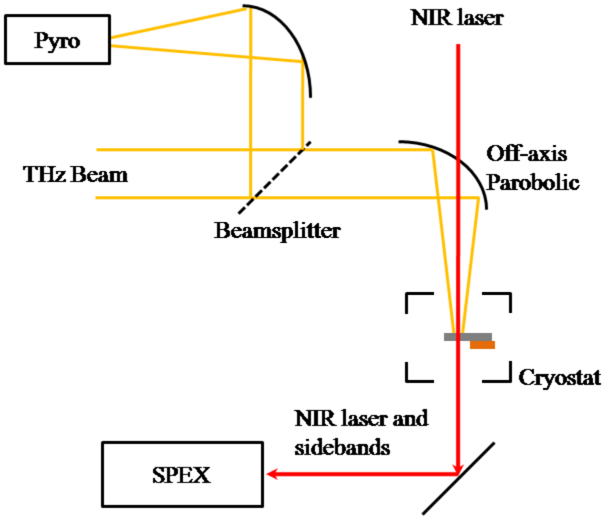

Figure 4.4: Experimental setup

electric field is polarized in the plane of the quantum well. The NIR laser focus is overlapped with the FEL focus so that the beams are collinear when travelling through the sample, which is held at a temperature of 10 K (Fig. 4.4). A diagram of the geometry at the sample is given in Fig. 4.5. The NIR laser and sidebands are then collected and analyzed.

The sidebands are dispersed in the 0.85m SPEX double monochromator and measured with a Hamamatsu R74000U-20 photomultiplier tube in most experiments but are occasionally mesured with the ICCD as well. The NIR beam is modulated with an acousto-optic modulator so that the NIR laser is only present at the sample, and more importantly at the detectors, when the FEL pulse is

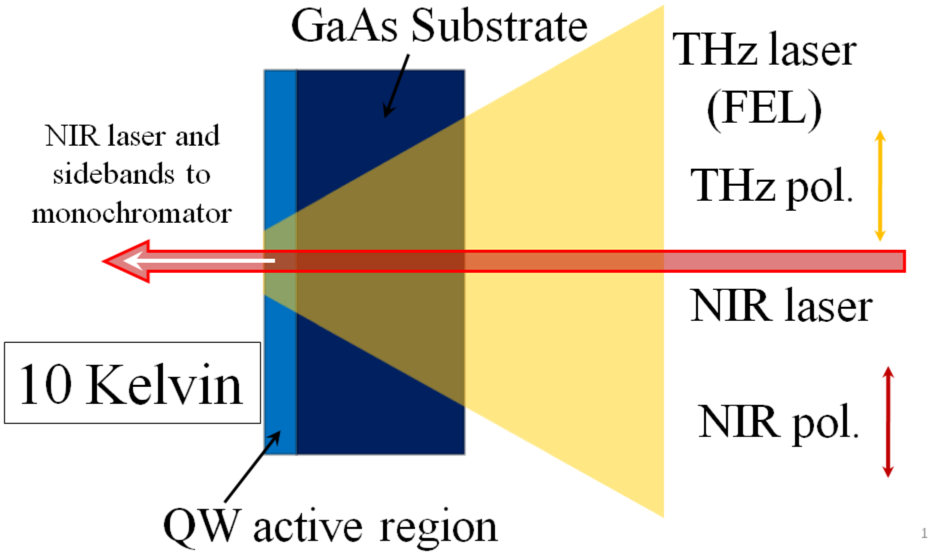

Figure 4.5: Illustration of the sample geometry

present as well. This prevents background noise, particularly for the ICCD which, as an integrating detector, is succeptible to pre pulse background. In particular the ICCD used will actually collect light, with an efficiency reduced by 1000, for 3 ms before the shutter opens. Additionally, the ICCD is succeptible to laser blooming and the sidebands get overpowered by the background signal in the fundamental laser line. Even when reduced in intensity by 100-1000, the fundamental laser line prevents measurement of higher order sidebands.

The slits on the monochromator are set so that the resolution is 0.2 meV (0.1 nm). The signal from the photomultiplier tube is sent through two stages of an SRS SR445 DC-300MHz amplifier to generate a gain of 25. The sidebands are then measured by either an oscilloscope or an SRS SR400 two channel gated photon counter depending on the strength of the sideband. Any background from the laser at the sideband frequencies will hinder measurement as we will be counting single photons. For this reason, an Edmund optics OD4 short pass filter is inserted into the laser path before the sample. To produce graphs of the full spectrum, a few sidebands are measured using both the oscilloscope and photon counter and the relative magnitudes of these signals are used to properly scale the amplitudes of the rest of the sidebands.

In the experiments performed, the FEL was split with a 90/10 beamsplitter so that it could be monitored on the scope using a pyroelectric detector and amplifier. In order to produce the most intense electric fields, pulses of 40 ns are created by cavity dumping the FEL (see section 1.3). For measurement as a function of polarization, the FEL was sent through a THz quarter wave plate. The quarter wave plate consists of a wiregrid polarizer at 45° to the FEL polarization with a mirror a variable distance behind it. By placing it in the FEL beam path at a 45° angle, the ellipticity of the polarization can be adjusted. This is because the linear FEL polarization is split into two orthoganlol components and one component is delayed with respect to the other. The FEL is focused onto the sample using an off axis parabolic mirror.

4.3.1.1 Note on Detection Methods

Signals measured with an oscilloscope have a background which is limited by electrical noise and the resolution of the scope. When the signal is measured using the photon counter, the background is limited by stray light which causes false counts. The average number of false counts per measurement is less than one, so the total number of counts measured when not measuring a sideband is often zero. However, to properly express the signal to noise ratio of our experiment, the amplitude of the signal used in the figures at these points is non-zero and is representative of the rate of false counts as compared to the actual measured signal. The errors quoted from data measured with an oscilloscope are given as a standard error of the mean. The errors quoted when measurements are taken with the photon counter are given by the square root of the number of counts, as typical for photon counting statistics.

4.3.1.2 Estimates of the Electric Field

In the experiments performed, the UCSB free electron lasers (FELs) are the source of the tunable, high intensity THz radiation. The electric field is estimated from the power during the FEL pulse and the spot size of the focused THz beam. The spot size is estimated from measurements using a Spiricon imaging system. The spot is taken to have a radius of 0.5 ± 0.05 mm at a frequency of 0.58 THz. In order to produce the most intense electric fields, pulses of 40 ns are created by cavity dumping[3] the FEL. The energy in each FEL pulse is measured by a Laser Precision Corp. RJ-7620 energy ratiometer and is used to estimate the power. The maximum energy available at the sample is greater than 100 μJ per pulse at 0.58 THz. The electric field can then be calculated, $F = \sqrt{\frac{2P}{A\epsilon_0 cn}}$, where F is the amplitude of the applied THz field, P is the THz power at the sample, A is the area of the THz spot and n is the refractive index in the material, taken to be 3.3 in the sample. The uncertainties quoted for the electric fields are due to fluctuations in the FEL power and uncertainty in the size of the THz spot. The field strength is given for each set of experimental data.

4.3.1.3 Estimates of the Exciton Density

We can estimate the density of excitons in each QW, $\rho_{exciton}$, from the NIR power incident on the sample, $P_{NIR} = 20$ mW, the absorption per quantum well, $\alpha = 0.05$, the exciton lifetime, $\tau < 5$ ns, the NIR spot size $r = 250\ \mu m$ and the NIR photon energy Ω_{NIR}. The density will then be given by

$$\rho_{exciton} < \frac{P_{NIR}\alpha\tau}{\Omega_{NIR}\pi r^2} \sim 10^{10}\, cm^{-2} \tag{4.14}$$

From this we estimate the inter-excitonic spacing to be greater than 100 nm at the highest powers. The Bohr radius of the exciton is estimated to be ~10 nm using a relative permittivity of $\epsilon \sim 13$ and an effective mass $m^*_{eff} \sim 0.067 m_e$. Thus, in these experiments we are not approaching the Mott density where excitons overlap. Given the low density of excitons, an electron from a particular exciton

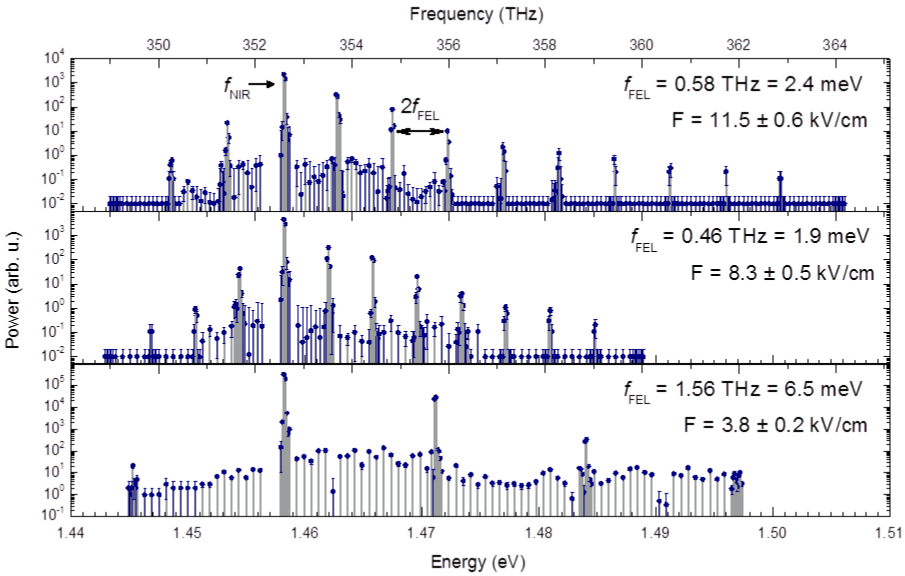

Figure 4.6: Sideband spectra from th 15 nm quantum well driven at frequencies of 0.46, 0.58, and 1.56 THz. The applied fields are quoted in the figure. At the highest THz frequency probed, the electric field was small and the ponderomotive energy was low, and fewer sidebands are observed.

can reasonably be expected to be ionized, accelerated away from the hole to which it was bound, and recollide with that same hole without scattering off of another one.

4.3.2 Observation of Sidebands

High-order sideband generation is observed at multiple THz driving frequencies. Spectra from a 15 nm quantum well are shown with the FEL at frequencies of 0.46, 0.58, and 1.56 THz are shown in Fig. 4.6. Sidebands from both a 15 and 18 nm quantum well are shown in Fig. 4.7, demonstrating the robustness of this effect. At a frequency of 0.58 THz, sidebands of up to eighteenth order ($n = 9$) are observed. We note that the energy associated with the highest-order sideband, $18hf_{THz} = 43.2\,meV$, is greater than the energy of the optical phonon in the material, $hf_{LO} \approx 36\,meV$. The intensity of the sidebands decays weakly with order above $n = 3$. This behavior is similar to the levelling off of intensity observed for high-order harmonics in high-order harmonic generation. The sideband plateau is also present when the FEL frequency is 0.45 THz, and sidebands of up to fourteenth order are observed. However, when the FEL frequency is increased to 1.56 THz, sidebands are generated only up to fourth order. This observation is consistent with the perturbative sideband generation seen in a quantum well exciton system at a similar frequency (Nat 16,17). Because the ponderomotive energy is lower at 1.56 THz and the 6.5-meV photon energy is comparable to the$\sim 10\,meV$ binding energy, the recollision model does not properly describe the sideband generation observed.

Sidebands at frequencies less than f_{NIR} are observed at all FEL frequencies that we investigated. Though the sidebands at frequencies above the NIR laser frequency are shown to have a non-perturbative origin, we believe the sidebands at frequencies below the NIR laser frequency are generated perturbatively. At frequencies below the laser frequency at most three sidebands are observed, there is no plateau region and the sidebands die off rapidly with increasing order. Unlike those of the sidebands at frequencies greater than f_{NIR}, the intensities of the

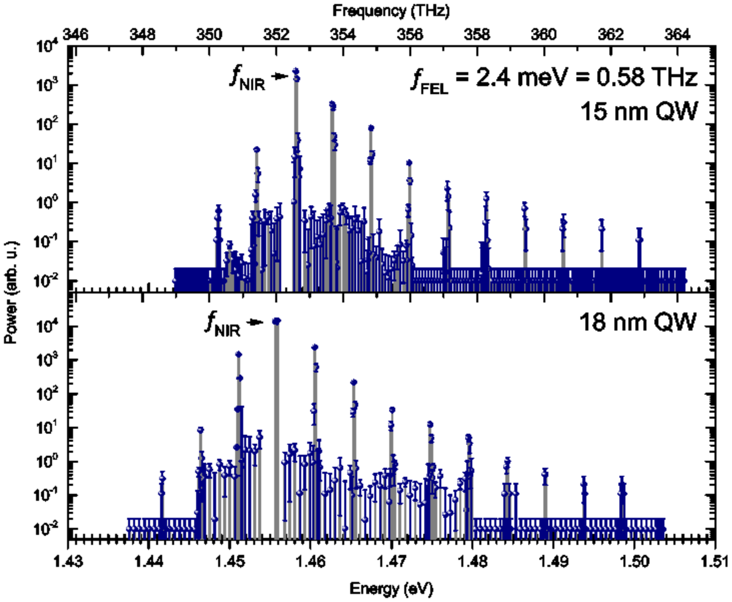

Figure 4.7: Sideband spectra in both a 15 nm and 18 nm quantum well with an applied field of$\sim 11^{kV}/_{cm}$ and a frequency of 0.58 THz.

sidebands below f_{NIR} decrease strongly with increasing order, implying that these sidebands are generated by means of a perturbative process. This is understandable because in this semiclassical model the electrons can only gain energy in the field and recollisions can only be responsible for sidebands at higher frequency than the laser.

4.3.3 THz Intensity Dependence

Intensity dependence of higher order perturbative processes have been discussed in section 2.1.2. For sidebands generated perturbatively, the intensity of the sideband of order $2n$ scales as the driving intensity to the power of $2n$, $I_{sideband,2n} \propto I_{THz}^{2n}$. The plateau observed in the intensity of the high-order sidebands indicates that high-order sideband generation is non-perturbative. This can be verified by investigating the dependence of individual sidebands on FEL intensity. Figure 4.8 shows the dependence of the $n = 1$ sideband ($f_{sideband} = f_{NIR} + 2f_{THz}$) on FEL intensity. At low power, we observe the expected perturbative behavior: the sideband intensity scales quadratically with FEL power. As the FEL intensity is increased, the intensity dependence deviates from quadratic and the perturbative description breaks down. For the most intense FEL fields, the sideband intensity is constant and the sideband is saturated.

Although it is often difficult to detect nonlinear optical processes above second order, we observe sidebands of fourteenth order or higher at two FEL frequencies

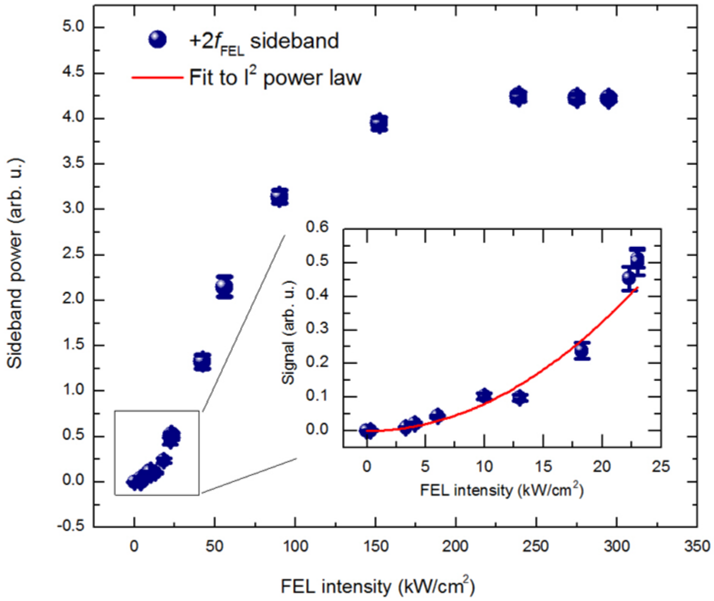

Figure 4.8: Dependence of the strength of the second order sideband ($n = 1$) as a function of the THz intensity. The inset is a zoomed in view of lower intensities. The red line shows the best I_{THz}^2 fit to the data. It fits well at low intensities but the sideband strength saturates at high THz intensities.

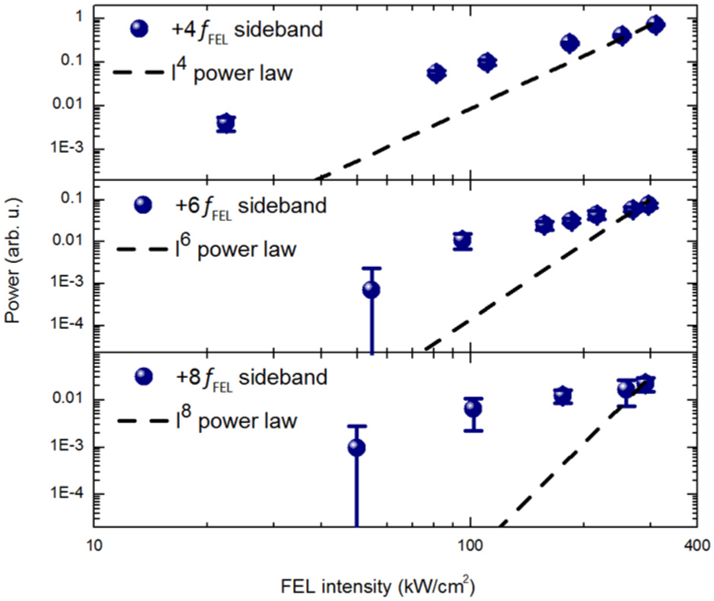

Figure 4.9: Dependence of the strength of the fourth, sixth and eighth order sidebands ($n = 2, 3, 4$) as a function of the THz intensity. The black dashed line line shows the best appropriate I_{THz}^{2n} fits to the data. None of the fits are good fits, and the fits deviate from the data strongly for higher order sidebands. This implies the sideband generation is non-perturbative.

in our experiment. The FEL intensity dependence of the higher-order sidebands further verifies the non-perturbative nature of the generation process. Figure 4.9 shows the FEL intensity dependence of the fourth-, sixth- and eighth-order sidebands (blue dots) as well as a fit to the appropriate power law (black dashed lines). The data systematically deviate from the power-law scaling, implying that the sidebands are not being generated perturbatively.

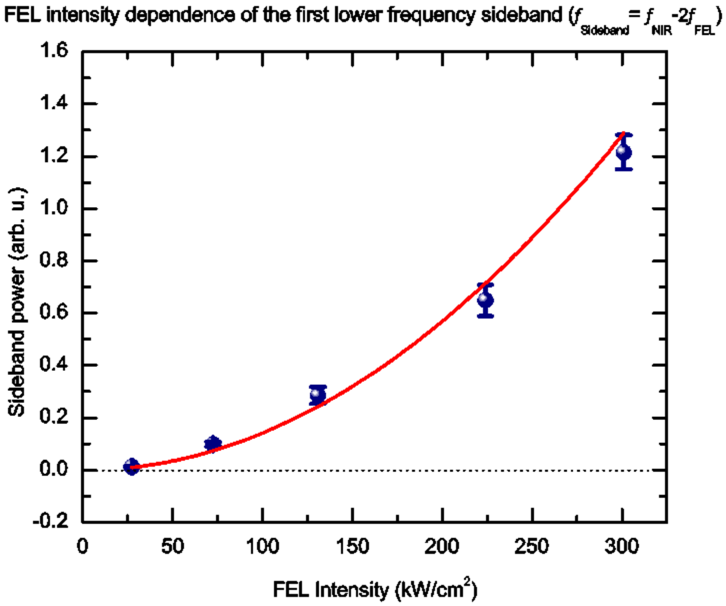

Figure 4.10: Dependence of the negative 2^{nd} order sideband ($n = -1$) on the THz intensity in a 15 nm quantum well. The data is well modeled by an I^2 fit, implying the perturbative nature of the sideband generation.

When observing the intensity dependence of the negative sidebands, we find that the experimental data fits the perturbaitve fits quite well. Data for the first negative sideband is shown in Fig. 4.10.

4.3.4 THz Polarization Dependence

The dependence of sideband intensity on the ellipticity of the FEL driving fields supports the identification of electron–hole recollisions as the mechanism for high-order sideband generation. Recollisions should be more likely to occur for the linear trajectories induced by linearly polarized driving fields than for the curved trajectories induced by elliptically polarized driving fields. Sideband generation is therefore expected to be least efficient for circularly polarized driving fields. We measured the sideband intensity as a function of the ellipticity of the FEL polarization. For a field

$$F(t) = F_x \cos(2\pi f t)\hat{x} + F_y \sin(2\pi f t)\hat{y} \tag{4.15}$$

with the ellipticity given by the phase φ, the amplitudes of the fields in the x and y directions are given by $F_x = \cos(\frac{\varphi}{2})$ and $F_y = \sin(\frac{\varphi}{2})$, respectively. The dependence of the second-, fourth- and sixth-order sidebands ($n =$1, 2 and 3) on the ellipticity of the FEL polarization is shown in Fig. 4.11 (blue dots). As predicted, the sideband intensity is at a maximum when the field is linearly polarized ($\varphi =$0, 180 and 360 degrees) and a minimum when the field is circularly polarized ($\varphi =$90 and 270 degrees). We also observed that the sideband intensity is slightly greater when the FEL polarization is parallel ($\varphi =$0 and 360 degrees) to that of the NIR laser, rather than perpendicular ($\varphi =$180 degrees). Further investigation is necessary to understand the origin of this asymmetry.

The electrons responsible for the highest-order sidebands have the highest energy, travel the farthest from the exciton core and are the least likely to recollide when on a non-linear path. Therefore, higher sidebands will have a stronger dependence on the ellipticity of the FEL polarization. A simple symmetry argument predicts that the intensity of the sideband of order $2n$ will scale as $\cos^{2n}(\varphi)$ (Supplementary Equations). These curves are plotted in Fig. 4.11 (black dash–dot

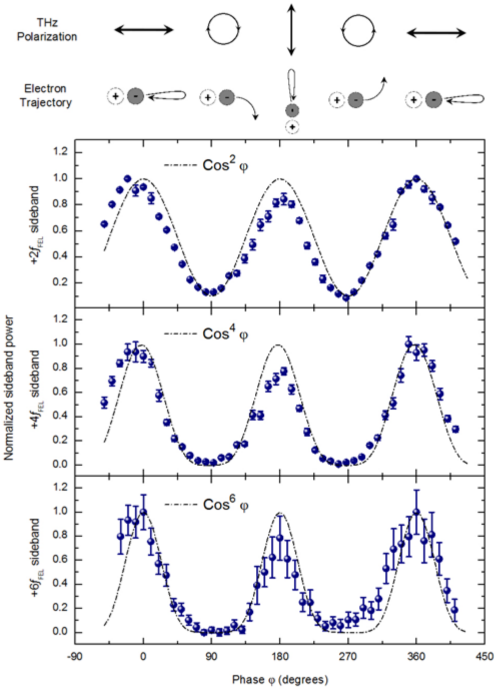

Figure 4.11: The data are taken in a 15 nm quantum well with $f_{THz} = 0.58$ THz. The electric field amplitudes in the x and y directions are given by $F_x = \cos(\frac{\varphi}{2})$ and $F_y = \sin(\frac{\varphi}{2})$, respectively. With a circularly polarized field applied, the nonlinear trajectory of the electron has the lowest probability of recollision and sideband generation is minimized. By conservation of angular momentum, we expect the intensity of the n^{th} sideband to scale as $\cos^{2n}(\varphi)$. The predicted curves (black dash–dot line) are plotted with the experimental data (blue dots) for the second-, fourth-, and sixth-order sidebands (n =1, 2 and 3). A sketch of the motion of the excited electron for a particular FEL polarization is shown at top.

lines), and comparison with our data indicates that the dependence of the sideband intensity on the ellipticity of the driving fields is in good agreement with the predictions.

4.3.4.1 Details of the Polarization Intensity Dependence

The dependence of the sideband generation on the ellipticity of the THz polarization can be written to lowest order by symmetry arguments. The electric field is given by where

$$
\begin{aligned}
F(t) &= [F_x \cos(\omega t),\, F_y \sin(\omega t)] \\
&= \frac{F_x + F_y}{2}[\cos(\omega t),\, \sin(\omega t)] + \frac{F_x - F_y}{2}[\cos(\omega t),\, -\sin(\omega t)] \\
&= F_+[\cos(\omega t),\, \sin(\omega t)] + F_-[\cos(\omega t),\, -\sin(\omega t)] \qquad (4.16)
\end{aligned}
$$

where $F_x = \cos(\frac{\varphi}{2})$ and $F_y = \sin(\frac{\varphi}{2})$, and F_+ and F_- are the amplitudes of circular and counter-circular polarized THz fields, respectively. Due to the symmetry of the system, the total angular momentum of the photons absorbed must be 0. Generation of the n^{th} sideband requires absorption of n pairs of circular and counter-circular polarized photons to conserve angular momentum, leading to a polarization in the sample

$$
\begin{aligned}
P^{2n} &\propto F_+^n F_-^n \propto (\frac{F_x + F_y}{2})^n (\frac{F_x - F_y}{2})^n \\
&\propto (F_x^2 - F_y^2)^n + O(F^{n+2}) \propto \cos^n(\varphi) + O(F^{n+2}) \qquad (4.17)
\end{aligned}
$$

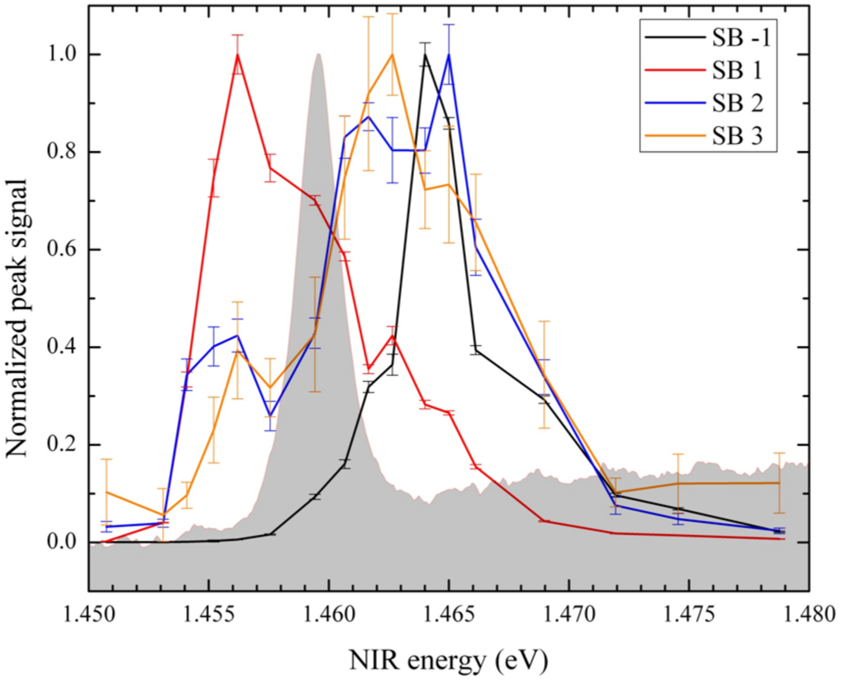

Figure 4.12: Near infrared frequency dependence of sideband generation in a 15 nm quantum well. The shaded area in the background shows the absorption from excitons in the quantum well.

To lowest order, we find the sideband intensity

$$I^{2n}_{sideband} \propto (P^{2n})^2 \propto \cos^{2n}(\varphi) \tag{4.18}$$

This leads to a dependence of the sideband intensity on the phase which describes the ellipticity of the THz polarization. For comparison, this dependence is plotted (chained line) with the experimental data in Fig. 4.11 and shows very good agreement with the sidebands measured.

4.3.5 NIR Frequency Dependence

As the NIR laser is detuned from the exciton resonance, the sideband intensity quickly decreases, demonstrating the excitonic nature of HSG. The sideband intensity as a function of NIR frequency does not exactly fit the absorption profile, but the overlap is quite strong. Both curves are shown in Fig. 4.12. As the NIR laser is detuned from the exciton resonance, the intensity of the lowest order sidebands quickly decreases. Theory predicts sideband generation and a sideband plateau even when the NIR laser is creating unbound electrons and holes[43]. However, the decrease of the sideband signal by orders of magnitude as the NIR laser is detuned from the exciton resonance indicates a strong excitonic influence on the experimental results.

We can see that the $n = 1$ sideband is strongest when it is slightly below the exciton resonance (Fig. 4.12). This sideband likely sees an enhancement when the laser photon energy plus twice the THz photon energy equals the exciton transition energy. This explains the peak of sideband intensity being lower than the exciton resonance by about twice the THz photon energy.

4.3.6 Temperature Dependence

Temperature dependent measurements of the $+6f_{THz}$, $+8f_{THz}$, and $+10f_{THz}$ sidebands are shown in Fig. 4.13. Though a systematic dependence of the sideband intensity on temperature is not established from these measurements, we do observe sideband generation up to 100K. We find that there is a maximum in the sideband intensity at 80K. We attribute this increase in the sideband signal to the temperature induced red-shift of the band gap which tunes the exciton transition slightly closer to resonance with the NIR laser and slightly enhances the sideband generation. We would like to point out that we have not adjusted the NIR laser to match the shift of the band gap and exciton resonance. It may be the case that our decrease in signal at higher temperatures is due to this detuning of the exciton resonance from the NIR laser and not solely from a temperature dependent change in the sideband generation efficiency, implying that sidebands may be present above 100K.

4.3.7 NIR Power Dependence

Sideband generation at a number of NIR powers is shown for multiple sidebands in Fig. 4.14. For fixed THz field amplitude (FEL intensity), the intensity of all sidebands increases linearly with NIR power at the lowest NIR powers used. The sideband intensities increase sub-linearly with NIR power at the highest NIR powers used. For the $+2f_{THz}$ sideband, the dependence of sideband intensity on NIR power is the same, up to a scale factor, for both relatively low THz field amplitudes and for the highest THz field amplitudes, at which the dependence of sideband intensity on THz field is saturated.

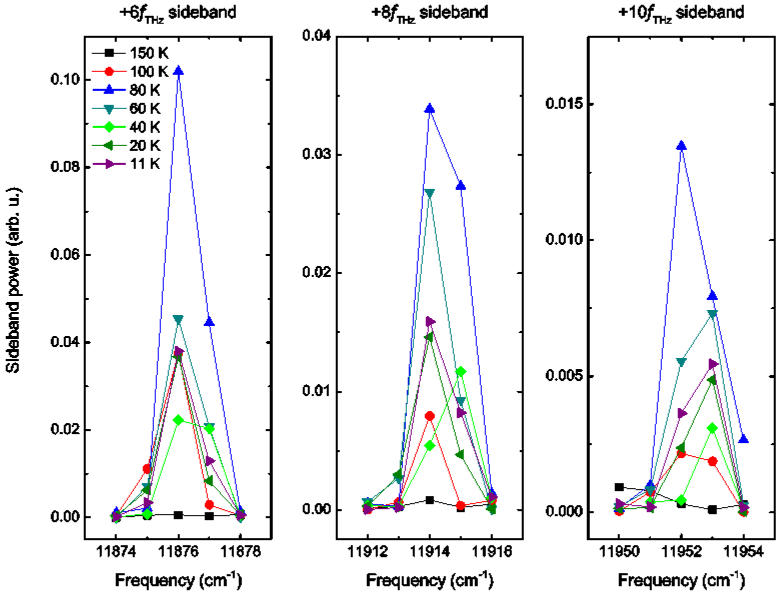

Figure 4.13: Temperature dependence of the third, fourth and fifth order sidebands. Our NIR laser was not adjusted to account for temperature dependent red shifts of the exciton resonance.

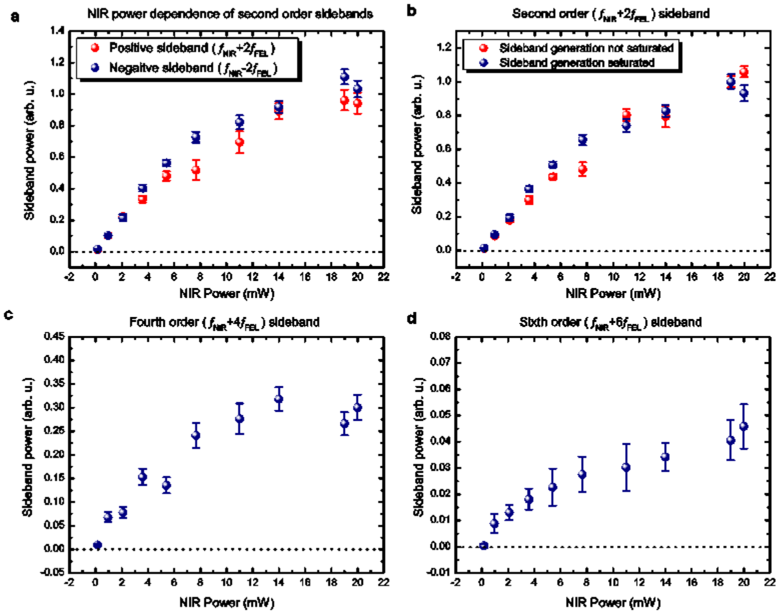

Figure 4.14: In a 22 nm QW driven by a 0.58 THz field, the dependence of the sideband strength on the NIR power is similar for all sidebands measured. The sideband strength increases linearly at lower NIR powers and increases sublinearly at the highest NIR powers. Graph a) shows NIR power dependence for both second order sidebands normalized to 1 at the maximum sideband power. Graph b) shows the NIR power dependence of the second-order positive sideband at and below THz saturation (normalized). Graphs c) and d) show the NIR power dependence of the 4^{th} and 6^{th} order sidebands, respectively.

4.3.8 Discussion

The nine sidebands observed at 0.58 THz are much fewer than the $\sim$ 44 sidebands predicted by calculating $\frac{E_{max}}{2hf_{THz}}$ assuming that $F = 11.5\,{}^{kV}\!/_{cm^2}$ and $m_{eff}^{*} = 0.067m_e$. However, a number of effects that are neglected by the existing theory could limit the number of observable sidebands. Although the distance between excitons in our experiment is $\sim$ 100nm (see section 4.3.1.3), the fields present suggest that the maximum excursion amplitude associated with the ponderomotive motion is greater than 400 nm. Scattering of the highest-energy electrons may prevent the observation of the highest-order sidebands. Additionally, we expect that the maximum kinetic energy that can be reached by a ballistic electron in the indium gallium arsenide quantum wells should be close to the 36-meV threshold for optical phonon emission, which is slightly less than the 43.2 meV of excess energy carried by the highest-order sideband observed. Finally, the highest-energy sidebands we have observed are near the limits of detection for this experiment, so the highest-order sidebands may have escaped detection.

Observation of high-order sideband generation in quantum wells demonstrates that the physics of recollisions extends beyond atoms and molecules. Though dielectric breakdown has made observation of high harmonic generation in solids difficult owing to the intense fields present during the short optical pulses, we have shown that recollisions in excitons can be studied at intensities well below the damage threshold of the semiconductor while using quasi-continuous wave sources.

4.4 Observation of High-Order Sideband Generation in Bulk GaAs

Recollisions have been predicted in any material which supports optical excitons[42,43] and direct observation of high-order sideband generation from a bulk semiconductor would solidify the effect as a universal phenomenon in semiconductors.

4.4.1 Sample

The GaAs sample used was purchased from the MBE growth lab as a 350 μm substrate wafer. A piece of the wafer was cleaved and then lapped to $\sim 100\,\mu m$ thick. After finally polishing the surface with a 0.5 μm grit polishing paper, a thick layer of photoresist was deposited and a ~1x1.5 cm rectangular hole was developed. A $BCl_3/Cl_2/Ar$ dry etch was performed in a Panasonic reactive ion etcher (ICP) and the final thickness of the hole was $\sim 10\,\mu m$. This was a long and time consuming process, and I believe an approach with a wet etch and no polishing would be a more effecient process.

The sample mounting and experimental setup is exactly identical to the sideband experiment discussed in section 4.3.1.

4.4.2 Observation of Sidebands

A large number of sidebands are observed in a bulk GaAs sample. Consistent with observations in quantum wells, the intensity of the sidebands decays only weakly as the order increases, particularly for the highest order sidebands.

The NIR spectrum when a strong THz field is applied to the GaAs quantum well excitons is shown in Fig. 4.15. With a THz field of 5 $^{kV}/_{cm}$ applied, sidebands of up to 14^{th} ($n = 7$) order are observed. The baseline value of 0.2 is representative of the noise level in the experiment. Any measured value with an error bar below the noise floor is considered too weak to confidently identify as a sideband, and the values below this confidence limit are represented by the gray crosshatch area in the figure.

Similar to what is observed for high sideband generation in quantum wells, there is a plateau in the intensity of the highest order sidebands. Though the ~10 μm thick bulk GaAs sample investigated here has orders of magnitude more active region than is present in the 15nm quantum well sample (150 nm active region from 10 quantum wells), the magnitude of the signal observed is similar in both the bulk and quantum well experiments. According to the manuscript by Yan[43], the increased coulomb energy of the exciton due to the confinement in the quantum

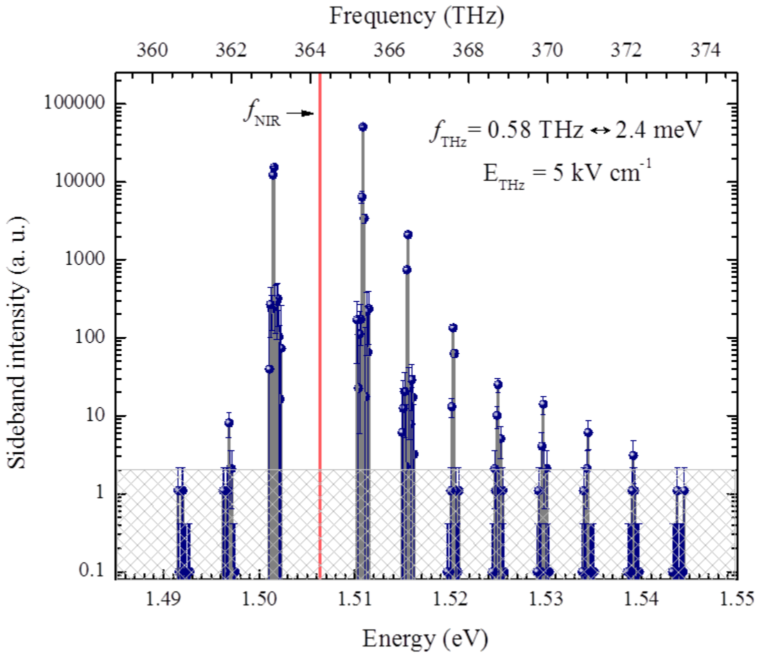

Figure 4.15: High-order sideband spectrum from a thin piece of GaAs. The frequency of the intense field was 0.58 THz and the peak electric field was 5 $^{kV}/_{cm}$. The gray crosshatch pattern represents the area that is below our confidence limit for identifying a sideband.

wells may increase the sideband generation efficiency. This increase in efficiency may be responsible for the comparatively strong signal from thin quantum well sample compared to the bulk GaAs sample. Alternatively, it may be that the sidebands we have observed are near saturation and it is not possible to produce sidebands of significantly higher intensity. It should be noted that the highest sidebands observed in this experiment are well above the band gap and higher sidebands that are not observed may have been reabsorbed while propagating through the material. More investigation is necessary to identify the optimal thickness sample to generate the strongest sidebands while minimizing sideband re-absorption above the band edge.

4.4.3 Temperature Dependence

Temperature dependent measurements of the sideband generation were performed between 10K and 170K and are shown in Fig. 4.16. At 170K, the tenth order sideband is still detected. In order to create excitons at higher temperatures, the frequency of the NIR laser must be adjusted to account for the temperature dependent shift of the GaAs band edge. A graph of the NIR frequency applied at different temperatures is shown in Fig. 4.16a. Figure 4.16b shows the peak sideband intensity for each sideband observed for temperatures between 10K and 170K. The NIR frequency scale is removed in order to better compare the data at different temperatures as the NIR frequency shifts with the temperature. The

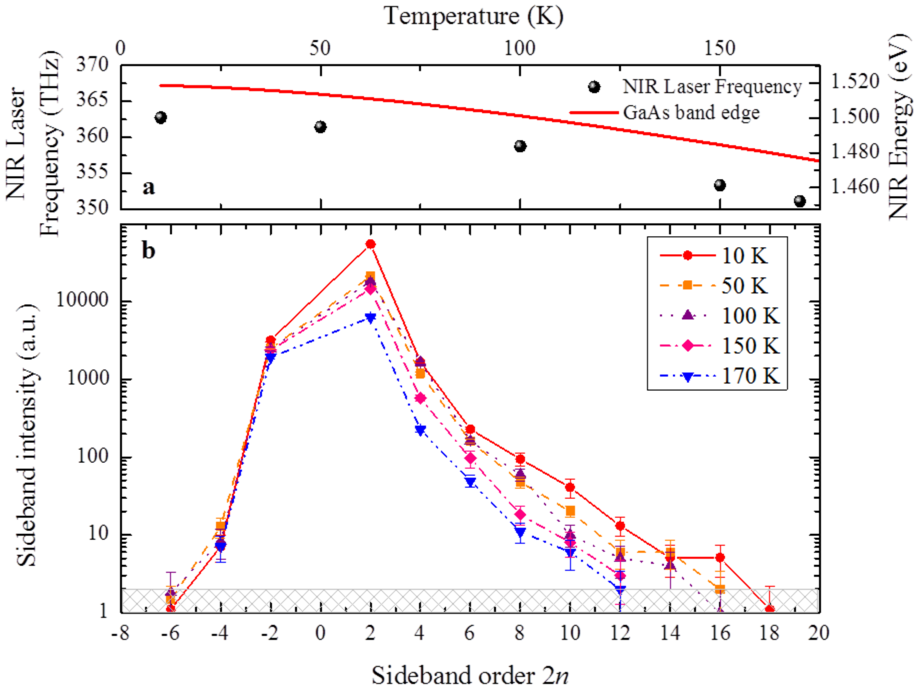

Figure 4.16: a) Plot of the NIR laser frequency applied for high-order sideband generation as a function of temperature (black dots). The NIR frequency is adjusted to account for the red shift of the GaAs band edge, which is given by the red line (from http://www.ioffe.ru). Our NIR laser cannot be tuned lower than ∼ 350 THz. b) Peak sideband intensity plotted as a function of temperature between 10K and 170K. Sidebands are identified by their order as opposed to their frequency for easier comparison. Sidebands of 10th order or greater are observed up to 170K.

sidebands plotted in Fig. 4.16 were taken with an applied THz field of $\sim 11^{kV}/_{cm}$. At 10K, sidebands of up to 16^{th} order are observed. The electric field applied in these measurements is greater than is what is presented in Fig. 4.15 and was achieved by use of the FEL cavity dump setup (see Section 1.3).

The most sensitive measurements made in this experiment are performed with a photon counter. Because the cavity dump pulse is only 40ns and the non-cavity dumped FEL pulse is 750ns, the measurement time for photon counting without the cavity dump is ~ 20 times greater than with the cavity dump. The increase in signal and signal to noise ratio associated with this increase of measurement time allows us to distinguish nearly as many sidebands with 5 $^{kV}/_{cm}$ applied as are observed with 11$^{kV}/_{cm}$ applied. The gray crosshatch pattern in Fig. 4.16b again represents the confidence limit for identifying sidebands.

4.4.4 NIR Frequency Dependence

The strength of a number of sidebands was measured as a function of the NIR frequency and is show in Fig. 4.17. Figure 4.17a shows the dependence on NIR intensity for the positive and negative second order sidebands ($n = \pm 1$). All sideband intensities have been normalized to their individual maximum values. There is a strong sideband signal for both of these sidebands when the NIR is resonant with the exciton frequency. However, the most intense sideband signal occurs slightly below the exciton resonance for the positive ($n = 1$, solid navy line) sideband and slightly above the exciton resonance for the negative ($n = -1$, dashed red line) sideband. The separation of the two peaks in the intensity profile for each of these sidebands is ~ 1.2 THz, approximately twice the THz frequency. This implies that the sideband signal for the second order sidebands ($n = \pm 1$) is strongest when the sideband, not the NIR laser, is resonant with the exciton frequency. Similar enhancements have been observed previously[37,38].

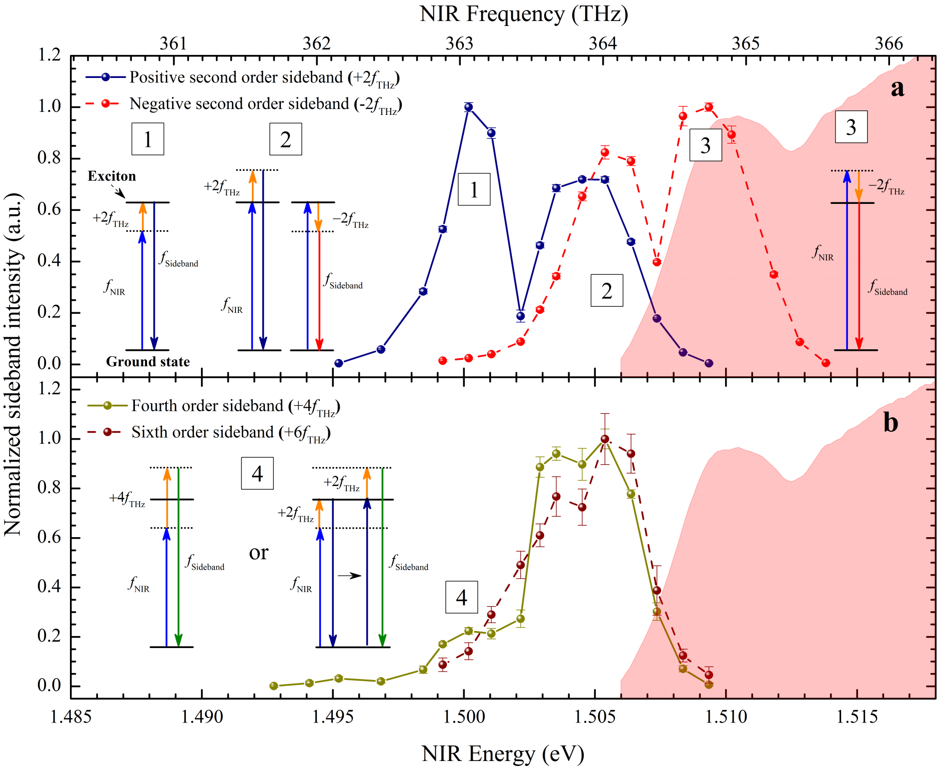

Figure 4.17: Sideband intensity dependence on the NIR laser frequency when a field of 0.58 THz is applied with a field of 5 $^{kV}\!/_{cm}$. The pink background is the absorption from the sample and the small peak is the exciton absorption. a) The sideband signal is shown for both the second order positive ($n = 1$, solid navy line) and negative ($n = -1$, dashed red line) sidebands. Peaks 1 and 3 show enhancement when the THz photon plus NIR photon frequencies sum to the exciton frequency. Peak 2 is when the NIR laser is resonant with the exciton line. b) The fourth and sixth order sidebands only show one peak in the NIR dependence, assumed to be resonance with the exciton transition. There is a small enhancement at 4 that may be due to a sideband generated on the first order sideband. We have assumed the peaks in sideband generation correspond to the exciton transition even though the exciton absorption is at a different frequency. This discrepancy is still not understood.

The NIR frequency dependence of the fourth and sixth order ($n = 2$ and 3, respectively) sidebands was also investigated (Fig. 4.17b). The sideband intensity for these higher order sidebands quickly decreased as the NIR frequency was detuned from the exciton resonance. There was no enhancement observed when the fourth order sideband was resonant with the exciton line. There is however a small enhancement in the intensity of the fourth order sideband when the NIR laser is detuned twice the THz frequency below the exciton resonance, where the second order sideband is most intense. This enhancement may be due to the strong second order sideband propagating through the sample producing its own second order ($n = 1$) sideband. This sideband of a sideband would be at the same frequency as the fourth order sideband.

We note that we have assumed the peaks in sideband generation correspond to the exciton transition even though the exciton absorption is at a different frequency, as can be seen in Fig. 4.17. This discrepancy is still not understood.

4.5 Conclusions

Our observation of high-order sidebands in bulk GaAs suggests that the recollision phenomenon is universal to excitons in semiconductors. In fact, it reveals the opportunity to study this phenomenon in different materials systems which should lead to an improved understanding of electron-hole recollisions. Additionally, the persistence of high sideband generation to temperatures greater than 170K may allow for experiments to be performed cryogen-free, which would be particularly beneficial for developing practical technology based on this phenomenon.

Bibliography

[1] C. Kittel. *Introduction to Solid State Physics.* John Wiley & Sons, Inc., 2005.

[2] J. H. Davies. *The Physics of Low-Dimensional Semiconductors.* Cambridge University Press, 1998.

[3] J. P. Kaminski, J. S. Spector, C. L. Felix, D. P. Enyeart, D. T. White, and G. Ramian. Far-infrared cavity dump coupling of the uc santa barbara free-electron laser. *Applied Physics Letters*, 57(26):2770–2772, 1990.

[4] R. W. Boyd. *Nonlinear Optics.* Academic Press, San Diego, 1992.

[5] V.G. Dmitriev, G.G. Gurzadyan, and D.N. Nikogosyan. *Handbook of Nonlinear Optical Crystals.* Springer-Verlag, 1991.

[6] I. Shoji, T. Kondo, A. Kitamoto, M. Shirane, and R. Ito. Absolute scale of second-order nonlinear-optical coefficients. *Journal of the Optical Society of America B-Optical Physics*, 14(9):2268–2294, 1997.

[7] I. I. Rabi. Space quantization in a gyrating magnetic field. *Physical Review*, 51(8):652, 1937.

[8] S. T. Cundiff, A. Knorr, J. Feldmann, S. W. Koch, E. O. Gobel, and H. Nickel. Rabi flopping in semiconductors. *Physical Review Letters*, 73(8):1178, 1994.

[9] J. P. Reithmaier, G. Sek, A. Loffler, C. Hofmann, S. Kuhn, S. Reitzenstein, L. V. Keldysh, V. D. Kulakovskii, T. L. Reinecke, and A. Forchel. Strong coupling in a single quantum dot-semiconductor microcavity system. *Nature*, 432(7014):197–200, 2004.

[10] T. Yoshie, A. Scherer, J. Hendrickson, G. Khitrova, H. M. Gibbs, G. Rupper, C. Ell, O. B. Shchekin, and D. G. Deppe. Vacuum rabi splitting with a single quantum dot in a photonic crystal nanocavity. *Nature*, 432(7014):200–203, 2004.

[11] R. J. Thompson, G. Rempe, and H. J. Kimble. Observation of normal-mode splitting for an atom in an optical cavity. *Physical Review Letters*, 68(8):1132–1135, 1992.

[12] S. H. Autler and C. H. Townes. Stark effect in rapidly varying fields. *Physical Review*, 100(2):703–722, 1955.

[13] D. R. Dion and J. O. Hirschfelder. Time-dependent perturbation of a two-state quantum system by a sinusoidal field. In I. Prigogine and Stuart A. Rice,

editors, *Advances in Chemical Physics*, volume 35, pages 265–350. Wiley Interscience, New York, 1976.

[14] H. Kamada, H. Gotoh, J. Temmyo, T. Takagahara, and H. Ando. Exciton rabi oscillation in a single quantum dot. *Physical Review Letters*, 87(24):246401, 2001.

[15] X. Xu, B. Sun, P. R. Berman, D. G. Steel, A. S. Bracker, D. Gammon, and L. J. Sham. Coherent optical spectroscopy of a strongly driven quantum dot. *Science*, 317(5840):929–932, August 17, 2007 2007.

[16] S. G. Carter, V. Birkedal, C. S. Wang, L. A. Coldren, A. V. Maslov, D. S. Citrin, and M. S. Sherwin. Quantum coherence in an optical modulator. *Science*, 310(5748):651–653, Oct 28 2005.

[17] J. F. Dynes, M. D. Frogley, M. Beck, J. Faist, and C. C. Phillips. Ac stark splitting and quantum interference with intersubband transitions in quantum wells. *Physical Review Letters*, 94(15), Apr 2005.

[18] M. Wagner, H. Schneider, D. Stehr, S. Winnerl, A. M. Andrews, S. Schartner, G. Strasser, and M. Helm. Observation of the intraexciton autler-townes effect in gaas/algaas semiconductor quantum wells. *Physical Review Letters*, 105(16):167401, 2010.

[19] M. Baur, S. Filipp, R. Bianchetti, J. M. Fink, M. Goppl, L. Steffen, P. J. Leek, A. Blais, and A. Wallraff. Measurement of autler-townes and mol-

low transitions in a strongly driven superconducting qubit. *Physical Review Letters*, 102(24):243602, Jun 19 2009.

[20] M. A. Sillanpää, J. Li, K. Cicak, F. Altomare, J. I. Park, R. W. Simmonds, G. S. Paraoanu, and P. J. Hakonen. Autler-townes effect in a superconducting three-level system. *Physical Review Letters*, 103(19):–, Nov 6 2009.

[21] H. Mabuchi and A. C. Doherty. Cavity quantum electrodynamics: Coherence in context. *Science*, 298(5597):1372–1377, November 15, 2002 2002.

[22] G. Gunter, A. A. Anappara, J. Hees, A. Sell, G. Biasiol, L. Sorba, S. De Liberato, C. Ciuti, A. Tredicucci, A. Leitenstorfer, and R. Huber. Sub-cycle switch-on of ultrastrong light-matter interaction. *Nature*, 458(7235):178–181, 2009.

[23] Y. Todorov, A. M. Andrews, R. Colombelli, S. De Liberato, C. Ciuti, P. Klang, G. Strasser, and C. Sirtori. Ultrastrong light-matter coupling regime with polariton dots. *Physical Review Letters*, 105(19):196402, 2010.

[24] T. Niemczyk, F. Deppe, H. Huebl, E. P. Menzel, F. Hocke, M. J. Schwarz, J. J. Garcia-Ripoll, D. Zueco, T. Hummer, E. Solano, A. Marx, and R. Gross. Circuit quantum electrodynamics in the ultrastrong-coupling regime. *Nat Phys*, 6(10):772–776, 2010.

[25] F. Bloch and A. Siegert. Magnetic resonance for nonrotating fields. *Physical Review*, 57(6):522, 1940.

[26] E. Arimondo and G. Moruzzi. Bloch-siegert shift in optically oriented 199 hg vapour. *Journal of Physics B: Atomic and Molecular Physics*, 6(11):2382, 1973.

[27] J. Tuorila, M. Silveri, M. Sillanpää, E. Thuneberg, Y. Makhlin, and P. Hakonen. Stark effect and generalized bloch-siegert shift in a strongly driven two-level system. *Physical Review Letters*, 105(25):257003, 2010.

[28] P. Forn-Diaz, J. Lisenfeld, D. Marcos, J. J. Garcia-Ripoll, E. Solano, C. J. P. M. Harmans, and J. E. Mooij. Observation of the bloch-siegert shift in a qubit-oscillator system in the ultrastrong coupling regime. *Physical Review Letters*, 105(23):237001, 2010.

[29] M. Cardona. Electron effective masses of inas and gaas as a function of temperature and doping. *Physical Review*, 121(3):752–758, 1961.

[30] S. G. Carter. *Terahertz electro-optic effects in (In)GaAs quantum wells*. PhD thesis, University of California at Santa Barbara, 2004.

[31] J. Cerne, A. G. Markelz, M. S. Sherwin, S. J. Allen, M. Sundaram, A. C. Gossard, P. C. van Son, and D. Bimberg. Quenching of excitonic quantum-well photoluminescence by intense far-infrared radiation: Free-carrier heating. *Physical Review B*, 51(8):5253–5262, 1995.

[32] W. Franz. *Z. Naturforsch. A*, 13A:484, 1958.

[33] L. V. Keldysh. *Sov. Phys. JETP*, 7:788, 1958.

[34] K. B. Nordstrom, K. Johnsen, S. J. Allen, A. P. Jauho, B. Birnir, J. Kono, T. Noda, H. Akiyama, and H. Sakaki. Excitonic dynamical franz-keldysh effect. *Physical Review Letters*, 81(2):457–460, 1998.

[35] B. Zaks, D. Stehr, T. A. Truong, P. M. Petroff, S. Hughes, and M. S. Sherwin. Thz-driven quantum wells: Coulomb interactions and stark shifts in the ultrastrong coupling regime. *New Journal of Physics*, 13(8):083009, 2011.

[36] J. Cerne, J. Kono, T. Inoshita, M. Sherwin, M. Sundaram, and A. C. Gossard. Near-infrared sideband generation induced by intense far-infrared radiation in gaas quantum wells. *Applied Physics Letters*, 70(26):3543–3545, Jun 1997.

[37] J. Kono, M. Y. Su, T. Inoshita, T. Noda, M. S. Sherwin, S. J. Allen, and H. Sakaki. Resonant terahertz optical sideband generation from confined magnetoexcitons. *Physical Review Letters*, 79(9):1758–1761, Sep 1997.

[38] M. Wagner, H. Schneider, S. Winnerl, M. Helm, T. Roch, A. M. Andrews, S. Schartner, and G. Strasser. Resonant enhancement of second order sideband generation for intraexcitonic transitions in gaas/algaas multiple quantum wells. *Appl. Phys. Lett.*, 94(24):241105, 2009.

[39] P. B. Corkum and F. Krausz. Attosecond science. *Nat Phys*, 3(6):381–387, 2007.

[40] L. V. Keldysh. Ionization in the field of a strong electromagnetic wave. *Soviet Physics JETP*, 20(5):1307–1314, 1965.

[41] M. Uiberacker, Th Uphues, M. Schultze, A. J. Verhoef, V. Yakovlev, M. F. Kling, J. Rauschenberger, N. M. Kabachnik, H. Schroder, M. Lezius, K. L. Kompa, H. G. Muller, M. J. J. Vrakking, S. Hendel, U. Kleineberg, U. Heinzmann, M. Drescher, and F. Krausz. Attosecond real-time observation of electron tunnelling in atoms. *Nature*, 446(7136):627–632, 2007.

[42] R. B. Liu and B. F. Zhu. High-order thz-sideband generation in semiconductors. In *AIP Conference Proceedings*, volume 893, pages 1455–1456. AIP, 2007.

[43] J. Y. Yan. Theory of excitonic high-order sideband generation in semiconductors under a strong terahertz field. *Physical Review B*, 78(7):075204, 2008.

Appendix A

Equipment Operating Procedures

Much of the information given in this section is either supplemented or provided in the thesis of Sam Carter.

A.1 Cryostat

The cryostat is a CTI Cryogenics Model 22 closed-cycle Helium refrigerator that can cool down to ∼10 K in about an hour. The cryostat is connected to a CTI Cryogenics Model 8200 Helium compressor through two high pressure Helium lines. It is also connected to the controller built into the compressor and to a Lakeshore 330 temperature controller. The sample is glued with rubber cement to a rectangular piece of copper that is screwed to a copper mount attached semi-permanently to the cryostat cold finger. A little bit of Apiezon vacuum grease applied between all of the copper pieces can improve thermal conduction and lower the base temperature. A Lakeshore temperature diode can be screwed to the sample mount, and insulated Nichrome heater wire is wrapper around the semi-permanent copper mount. A voltage can be applied to samples by connecting the pins glued to the sample mount to the 10 wires with pins soldered on the ends, each labeled by a letter. Teflon tape is used to secure the wires to the semi-permanent copper mount. The cryostat is mounted on two translation stages for lateral motion and on a labjack for vertical motion.

Cool down procedure

1. Evacuate cryostat to less than$\sim 2 \times 10^{-6}$ T. This may only take 2 to 3 hours, but pumping overnight will likely increase the time the cryostat can stay cold.

2. Turn on the building cooling water for the compressor.

3. Turn on compressor, wait until cold. Continue pumping on the cryostat during the cool down until just above 77 K, then close the valve to the cryostat.

The cryostat can stay cold for 2 to 3 days before it starts to warm up. Occasionally, the temperature starts creeping up really soon after cooling down. This problem can be fixed by pumping on the cryostat again for just a few minutes (make sure the pressure is low before opening the valve between the pump and cryostat). Also, if the base temperature does not drop below ∼11K, the o-ring which seals the cover of the cryostat may need to be re-greased. Apply a little bit of the silicon vacuum grease and then wipe with a Kimwipe so that there is only a thin layer of grease on the ring. This problem may be avoided if a new o-ring for the cryostat is purchased. The temperature stays pretty stable at 10 K without temperature regulation, but the heater can certainly be used with the temperature controller. If the temperature is raised above 77K, it will likely need to be pumped on to reach 10K. Do not open the cryostat at low temperatures as sample will still be cold and whatever is in the air will be able to freeze to the sample.

To warm up the cryostat, turn off the compressor and the cooling water. Warm up takes several hours. Warm up can be expedited by using the heater.

Maintenance

The Helium pressure in the compressor must be maintained at 250 psi. Occasionally there is a need to add additional Helium to the compressor. Make sure the helium used is ultra-high purity, the actual purity needed is stated in the manual. The procedure for this can also be found in the manual, but a high-pressure regulator and a special flared fitting needs to be used. There is a maintenance flange for this that is found in the lab. See the manual for other necessary maintenance.

A.2 Argon/Ti:Sapph laser

A.2.1 Argon laser (Coherent Innova 300)

The Argon laser puts out up to 12 W of power at multiple lines in the blue. It must be cooled with several gallons per minute of deionized water from the Coherent heat exchanger, which is cooled by the building water. For pumping the Ti:Sapphire, the Argon laser is run at ~6.5 W (light regulated) using 50 amps with aperture number 6. The Argon laser should be run for at least an hour every couple weeks at about this power. When it is turned on, it should usually be run for at least a half an hour at this kind of power.

A.2.2 Titanium Sapphire laser (Coherent 890)

The Ti:Sapphire is a cw laser that in principle can be tuned from 675 nm to 1100 nm, providing up to ~1 W of power. Typically, it puts out 200 to 300 mW when pumped by the Argon laser with ~6.5 W. It is tuned by rotating a birefringent filter using a computer controlled Newport motion controller/linear actuator. There are 4 to 8 cm^{-1} jumps in the tuning, which don't seem possible to eliminate. As the tuning crystal rotates, the wavelength continues making these steps until it moves out of the good tuning range. The wavelength will then jump from one end of the tuning range to the other. The output coupler can be changed to determine the wavelength range it operates at.

Turning on and off the Ti:Sapphire is controlled by turning on and off the Argon laser. Deionized cooling water from the heat exchanger is also sent to the Ti:Sapphire. (This must be turned off if the Argon laser is run without the Ti:Sapphire or water may condense on the Sapphire crystal.) After the laser has warmed up for at least 15 minutes, the laser power can be peaked up by adjusting the two knobs on the end of the laser (above the output). This doesn't change the beam alignment.

The linear actuator that controls the laser wavenumber should always be sent to a fixed position when turning off the laser just in case the power to the motion controller goes out (it loses the position). The Newport motion controller should always be left on. Values for the laser power and wavenumber should be recorded in the log book.

Operation procedures

First of all, be careful with this laser. It puts out a lot of power! Make sure the laser is being sent to the Ti:Sapph or blocked by a beam dump.

Turn on

1. Turn on building cooling water, heat exchanger

2. Turn on circuit breaker

3. Enable laser with key

4. Set to current regulation, 40 amps, turn on
5. If laser is going to Ti:Sapph, make sure the external water lines cooling the crystal are on
6. Wait $\sim$15 minutes for laser to stabilize
7. Set to light regulation and increase power to ˜6.5 W.

Turn off

1. Record info in log book
2. Set to current regulation, turn down to 40 amps
3. Turn off Argon laser
4. Make sure water to Ti:Sapph crystal is off
5. Disable laser with key
6. Turn off circuit breaker
7. Wait 10 minutes for laser to cool off
8. Turn off heat exchanger, building cooling water

Argon laser maintenance

A rebuilt laser tube was installed in the summer of 2002 by Laser Innovations, so it may need to be replaced in the near future. Sometimes the power needs to be peaked up by pressing the “Tune” button and adjusting the knobs on the back end of the laser. At one point the power became quite unstable and would not regulate the power well, please refer to Sam Carter’s thesis if this is the ever case. The laser was serviced by Coherent in 2007, however, Coherent no longer services this model laser, so service will not be available from them in the future.

Ti:Sapph laser maintenance

Sometimes the alignment needs to be tweaked to peak up the power. The cover must be taken off and laser goggles should be worn. Adjust the upper and lower cavity mirrors (see manual) to peak up the power. More detailed procedures are in the manual. Sometimes it is a good idea to clean some of the optics with methanol at this time (see manual).

Improving the tuning range and tuning jumps is tricky. The jumps can sometimes be improved by rotating the Sapphire crystal about the vertical axis. This is done by loosening a clamp on the crystal mount and rotating by hand (with the Argon laser aperture closed), so precise, reproducible changes are impossible. The power must be peaked up again after each adjustment. Sometimes a rotation about the horizontal axis can significantly improve the power and the tuning range as well. Be extremely careful when adjusting the laser, even small adjustments can make it very difficult to achieve lasing again! It may be a good idea to have a service call if the tuning poses too much of a problem, however, you would need to find a third party vendor to do this.

The output couplers can be changed pretty easily as outlined in the manual. Only the output coupler needs to be changed. The power will have to be peaked up after the change.

A.3 Acousto-Optic Modulator

An IntraAction AOM-602N acousto-optic modulator (AOM) is used to pulse the NIR beam. The AOM forms a pressure grating using an RF source (IntraAction Model ME signal processor) that diffracts the NIR beam. The RF source is turned on and off with a trigger–forming a pulse in the diffracted signal. (Make sure the RF cable doesn't get to close to any signal cables.) For alignment, the laser should first be sent straight through the AOM aperture. Then, look for the first-order diffracted beam while making slight adjustments to the incident angle. Isolate the first-order beam and send to a power meter, then use the tip/tilt of a mirror sending the beam into the AOM to maximize the power in the first-order beam.

A.4 SPEX Monochromator

The SPEX 0.85 m double monochromator is used for sideband experiments and when high resolution is needed. Inside, there are two 1800 lines/mm holographic gratings, 5 mirrors, and two apertures, so only about 10% of the light entering the SPEX reaches the exit slit. The light should be horizontally polarized or the efficiency is much worse. The slits are usually set to 400 μm, giving a resolution of 1 cm^{-1}. (Often, the entrance slit is set to 100 μm to ensure the NIR beam is coming to a good focus at the slit.)

Alignment is performed by first sending a laser into the monochromator with no focusing lens. Adjust the beam to get maximum power through the slit and so that it is centered on the first mirror. (There are white mirror covers under the SPEX that can be used for this purpose.) The laser should also be centered vertically on the slit. Then, put in the lens and adjust to get maximum power through the slit while keeping the beam centered on the first mirror. The laser should then be aligned. Check that the laser makes it all the way to the exit slit, and make sure that it is centered where the detector will be (don't let the beam actually hit the detector). If the beam is way off, either the alignment into the SPEX is bad or the SPEX itself is misaligned (bad news). After the laser is aligned into the SPEX, place two irises in the beam path to align with in the future. There are currently two irises in place, it should suffice to align to these and then maximize the signal at the PMT by translating the lens right before the entrance slit.

The output wavelength of the SPEX is controlled by a SPEX MSD Ministep-driver, which is interfaced through the SPEX 232/488RET GPIB Controller. These are left on all the time. There is a counter on the side of the SPEX that shows what wavenumber it is at. This wavenumber can only controlled by computer, using the Labview vi's in the next section. The SPEX should only be scanned from high to low wavenumbers.

Labview VI's

1. SPEX init.vi: Initializes SPEX communications and wavenumber. If the SPEX is not responding properly, use this program.
2. SPEX global: Global Labview variable that keeps track of the SPEX wavenumber. To change the SPEX wavenumber, change this file to the correct value and then run SPEX init.vi
3. Copy of SPEX goto wavenumber.vi: Moves SPEX to desired wavenumber. (The original version of this VI is linked to the Optilab VI)
4. Optilab-BEN.vi: A program that can read out and perform math operations on the Agilent scope. Is linked to a few of the SPEX VI's.

Optilab startup

1. Open the program Optilab-VNA-BEN.vi.
2. Press the arrow to run the program.
3. From the top menu, select System→UCSB FEL→SPEX monochromator
4. Click yes to the sub-VI "Initializing Kiethley 2400" (this will actually initialize the scope) (Set ID Query to Yes and Reset to No)
5. Set boxcars, math and wavelength region. Remember to always set your start to a higher wavenumber than your finish so that the SPEX only scans from high to low.
6. Press the Start button to run the VI.

A.5 Photomultiplier Tube

A Hamamatsu R7400U-20 photomultiplier tube (PMT) detector was mounted on the SPEX for most of the experiments. A PMT was used due to its high noise-free gain (10^6) needed for these measurements. The photocathode for this PMT is multialkali, which gives a quantum efficiency of 10% at 800nm. The efficiency dies off rapidly past 830 nm. Cooled GaAs PMTs could probably give a somewhat better signal to noise, but GaAs PMTs cannot tolerate much power and are more expensive.

A voltage of -900 V was applied to the PMT anode from an SRS high voltage source. The output current was sent to an SRS 445 preamp set to 50Ω. It was sent through two channels with a gain of 5 each for a total gain of 25.

A.6 SRS Photon Counter

There is a SRS SR400 photon counter which can be used to measure extremely small signals measured with the PMT and SPEX. The photon counter will look for rising or falling edges of a set magnitude within a specific time window. Inside this time window it can identify pulses separated by as little as ~5 ns.

Operation procedure

1. Send trigger pulse into both External Start (TTL in) and Trig In (10 kΩ).
2. Send your signal from the PMT amplifier to Input A or B (50 Ω).
3. The window for detecting photons can be observed by connecting Gate A or B (50 Ω out) to a scope.
4. Set gate width and delay to proper values by adjusting controls on the front panel menu of the SR400 (see manual for more information)
5. After set, open: Bens SR400 with SPEX new.vi.
6. Read values from the LCD front panel of the SR400 and enter into the VI. Set values for number of measurements, 'trig' level (for triggering photon

counting window), and photon trigger level (for detecting a single photon). Leave dwell time at 0 and TSET at 0.001.

7. Set the measurement step size and wavelength region for the scan. Remember to always set your start to a higher wavenumber than your finish so that the SPEX only scans from high to low.

8. Run VI. Often a long or short pass filter is necessary at the output of the Ti:Sapph to minimize the background counts from Ti:Sapph luminescence.

A.7 Intensified CCD

An Acton 0.275 meter triple grating monochromator with a Princeton Instruments intensified CCD (ICCD) was used for experiments as well. The monochromator has two switchable gratings, 1200 lines/mm and 300 lines/mm. An ICCD is attached to the monochromator. This detector is similar to a PMT in that it amplifies electrons ejected from a photocathode, but it provides an entire spectrum at once using the CCD. The signal is intensified when a high-voltage pulse is applied to the detector. This pulse is also used to gate the detection on time scales as short as a few ns. The ICCD is cooled with a TE-cooler, reducing dark counts. The chiller need DI water to function, make sure it is always topped off to the line before use.

Operation procedure

1. Open Nitrogen valve to purge ICCD
2. Turn on small chiller, building cooling water
3. Turn on PI Detector controller along with the cooler switch, wait for status LED to turn green.
4. Block monochromator, turn on PI Pulse Generator Model PG-10.
5. Connect external trigger to PI pulse generator or use internal trigger
6. Set pulse gate width and gate delay.
7. Set center wavelength and grating of monochromator using Acton Spectradrive Stepping Motor Scan Controller.
8. Run Labview vi: ICCD Front Panel-Jing.vi (or similar). Select init CCD the first run.
9. Unblock monochromator. If saturated (counts $>$ 16000), immediately block monochromator and reduce gate width.

There is an output on the back of the PI pulse generator (monitor gate 1) which provides a reference for the gate pulse. This can be used to ensure the pulse timing is correct.

Troubleshooting

Sometimes the program will freeze up. The solution is usually to stop the program, push the reset button on the PI Detector controller, and run the program again, making sure to select the init CCD button. Occasionally, Labview needs to be restarted altogether. Also, there seems to be more communication problems when the ICCD is run at a repetition rate of 2 Hz or faster.

Appendix B

Experimental Procedures

B.1 NIR/THz Alignment

If changes are made to either the NIR or THz alignment, the system must be re-aligned to ensure that the NIR and THz focal spots are overlapped at the sample. For realignment of the AT experiment, see Sam Carter's thesis. Here realignment of the collinear sideband setup will be described.

1. Remove the sample mount and lower the cryostat so that you can insert a pinhole or possibly the Spiricon.
2. Turn on the FEL alignment laser. At the focal spot make sure the focus looks good (circular, not elliptical). Make adjustments to the off-axis parabolic if the spot is elliptical in order to correct and achieve a circular spot.

3. Put a pinhole with a power meter behind (or Spiricon) on a 3-axis stage and maximize the alignment laser signal through the pinhole.

4. If the FEL can be used for alignment, a pyroelectric detector can be mounted behind the pinhole. The Spiricon can be used to image the focal spot of the FEL.

5. Once the position of the FEL is known, the NIR laser can be aligned. Send the laser through a lightly focusing lens and through the back of the off-axis parabolic. Check to make sure the power making it through the OAP is maximized.

6. Now adjustments can be made to the lens and mirrors right before the OAP to maximize the signal through the pinhole (or overlap on the Spiricon).

The alignment should be very close to optimized by this procedure, however, small adjustments to the NIR beam can be made while observing the signal to maximize the observed signal. Irises can be inserted into the both the NIR and THz beam path in order to mark the well aligned laser path.

B.2 Spiricon

The focused spot of the FEL can be observed using the Spiricon imaging system. Place the head (Pyrocam) of the Spiricon so that the FEL alignment laser is on the pyroelectric active region. A computer monitor is necessary to run the Spiricon. The following connections must be made:

Pyrocam

1. Power cable
2. VGA (to LBA Sync in on rear panel)
3. RS170/CCIR (to LBA Video in on front panel)
4. Trigger in (at least 8.5 ms before FEL event-FEL advanced trigger)

LBA controller

1. Power cable
2. Sync in (to Pyrocam VGA)
3. VGA (to monitor)
4. Video in (to Pyrocam RS170/CCIR)

Procedure

1. First, set the FEL advanced trigger to 8.5 to 11 ms ahead of the FEL event.
2. Attempt to focus the alignment laser on the front of the pyrocam.
3. Make sure you hit the run button on the Pyro cam.

4. Choose the gain on the pyrocam (1, 3 or 10) and set the output to LBA

LBA setup

On the LBA, go to menu, then go to setup.

1. Trigger mode: Vid Trig Run/Stop
2. Trigger level: 128 (can be less if you have less signal)
3. Capture Method: Continuous

Under menus, go to Cameras.

1. Camera type: 14-Pyrocam 1
2. Sync Source: External

Under menus, go to Macro

1. CW Mode B

B.3 SPEX Alignment

After sidebands are generated at the sample, they need to be sent to the SPEX monochromator to be analyzed. The sidebands will come out propagating collinear with the NIR beam. By sending the NIR laser into the SPEX, we are also aligning the sidebands to be analyzed. Often it is only necessary to align to the two irises at the entrance of the SPEX.

1. Open the entrance slits of the SPEX to $\sim 400\mu$m.
2. Make sure the exit and center slits are closed, the SPEX wavelength is far from the laser wavelength and the PMT is off. (The PMT can be removed but is not necessary)
3. Send the laser (modulated by the AOM) into the entrance slits and make sure the the laser is centered on the first grating in the SPEX.
4. Attenuate the NIR laser by ~1000 and turn down the AOM to 0.
5. Close the entrance slit and open all other slits to $\sim 400\mu$m and turn on PMT to 700V.
6. Send the SPEX to the NIR laser wavelength.
7. Open the entrance slit to $\sim 50\mu$m.
8. Slowly increase the AOM signal until a signal can be seen from the PMT (on the oscilloscope). It should be easy to see the modulation from the AOM.
9. Adjust the laser as it enters the entrance slit to maximize the signal.
10. After this signal is maximized, insert a lens near the entrance slit.
11. Adjust the position of the lens to maximize the PMT signal.
12. Put in two irises right before the entrance of the SPEX.

Aligning the NIR laser to these two irises is often all that is necessary to have good alignment into the SPEX. Only if you cannot see any signal when aligned to these irises should the previous procedure be performed.

B.4 Sample Polishing

The samples used in the AT experiment have the facets polished in order to slightly improve the coupling to the sample. The samples were polished using the microscopy preparation lab in CNSI, the polishing machines are maintained by Mark Cornish.

1. Find the polishing mount with the proper angle.
2. Set hot plate to 100 C and put polishing mount on hot plate
3. With metal tweezers, place a very small amount of wax where the sample will be mounted.
4. Adjust the polishing mount such that the sample facet slightly hangs over the edge of the polishing mount.
5. Take off hot plate and let cool.
6. Mount onto the polisher.
7. Put 3μm grit paper down on polisher.

8. Turn on water.

9. Polish sample until the whole facet is at an angle.

10. Switch to 1μm polishing paper. Check in microscope when facet looks smoother.

11. Switch to 0.5μm polishing paper. Check in microscope when facet looks smoother.

12. Heat up on hot plate and remove sample. Clean in acetone before use to remove any leftover wax.

B.5 Cavity Dump

To achieve the highest intensities using the FEL, the cavity dump system must be used.

1. Make sure the FEL beam line is set to the cavity dump line.

2. Turn on Big Sky laser in FEL vault, usually before turning on the FEL. Allow at least 15 minutes to warm up.

3. Tune up FEL.

4. Set the FEL advanced trigger to 1.6 ms. The AT should already be triggering the YAG laser.

5. Use the AT to trigger a delay generator.
6. Send a pulse 926 μs after the AT to trigger the flashlamp (Cable 1 in 1380D).
7. Send a pulse 666 μs after the flashlamp pulse to trigger the Q-switch (Cable 2 in 1380D). This will actually dump the cavity so the timing may have to be adjusted slightly to dump the cavity at the correct time during an FEL pulse.

The cavity dump should be observable on a pyroelectric detector as a fast rise in the FEL power.